MOHAMMED FIRST UNIVERSITY
FACULTY OF SCIENCES IN OUJDA

DOCTORAL THESIS IN ASTROPHYSICS

Search for magnetic monopoles with the ANTARES neutrino telescope

---

Author:
Imad EL BOJADDAINI

Supervisor:
Prof. Yahya TAYALATI

Defended in front of the jury members:

Prof. Antoine Kouchner (President) .... *Paris-7 University, Denis Diderot, France*

Prof. Yassine Hassouni (Referee) .... *Mohammed V University, Rabat*

Prof. El Hassan Tahri (Referee) .... *Mohammed I University, Oujda*

Prof. Maurizio Spurio (Referee) .... *University of Bologna, Italy*

Prof. Morad El Baz (Examiner) .... *Mohammed V University, Rabat*

Prof. Abdelilah Moussa (Examiner) .... *Mohammed I University, Oujda*

Prof. Taoufik Ouali (Examiner) .... *Mohammed I University, Oujda*

Prof. Yahya Tayalati (Thesis supervisor) .... *Mohammed V University, Rabat*

Laboratory of Physics of Matter and Radiation
Department of Physics

December 08, 2018

UNIVERSITÉ MOHAMMED PREMIER
FACULTÉ DES SCIENCES D'OUJDA

THÈSE DE DOCTORAT EN ASTROPHYSIQUE

Recherche de monopôles magnétiques avec le télescope à neutrinos ANTARES

Auteur:
Imad EL BOJADDAINI

Encadrant:
Prof. Yahya TAYALATI

Soutenue le 08 Décembre 2018 devant le jury composé de:

Pr. Antoine Kouchner (Président) .... *Université Paris-7, Denis Diderot, France*

Pr. Yassine Hassouni (Rapporteur) .... *Université Mohammed V, Rabat*

Pr. El Hassan Tahri (Rapporteur) .... *Université Mohammed I, Oujda*

Pr. Maurizio Spurio (Rapporteur) .... *Université de Bologne, Italie*

Pr. Morad El Baz (Examinateur) .... *Université Mohammed V, Rabat*

Pr. Abdelilah Moussa (Examinateur) .... *Université Mohammed I, Oujda*

Pr. Taoufik Ouali (Examinateur) .... *Université Mohammed I, Oujda*

Pr. Yahya Tayalati (Directeur de thèse) .... *Université Mohammed V, Rabat*

Laboratoire de Physique de la Matière et du Rayonnement
Département de Physique

Le 08 Décembre 2018

"It always seems impossible until it is done."

Nelson Mandela

MOHAMMED FIRST UNIVERSITY

Abstract

Faculty of Sciences in Oujda
Department of Physics

Doctor of Philosophy

Search for magnetic monopoles with the ANTARES neutrino telescope

by Imad EL BOJADDAINI

A search for magnetic monopoles using 5 years of data recorded with the ANTARES neutrino telescope from January 2008 to December 2012 with a total lifetime of 1121 days is presented. The analysis is carried out in the range $\beta > 0.6$ of magnetic monopole velocities using a new simulation strategy based on run-by-run Monte Carlo simulations. No excess above the background expectation from atmospheric muons and atmospheric neutrinos is observed, and upper limits are set on the magnetic monopole flux ranging from 5.7×10^{-16} to 1.5×10^{-18} $\mathrm{cm}^{-2} \cdot \mathrm{s}^{-1} \cdot \mathrm{sr}^{-1}$.

Key words : Magnetic Monopole, ANTARES, Neutrino telescope.

Résumé de la thèse

L'astronomie des neutrinos est une discipline qui vise à explorer l'univers avec une toute nouvelle sonde (le neutrino) ayant une interaction différente en comparaison avec les photons. ANTARES est l'un des plus grands télescopes à neutrinos au monde, avec un champ de vision complémentaire au télescope à neutrinos IceCube. La présente thèse de doctorat a pour but de définir une méthode de recherche des monopôles magnétiques (MM) à l'aide des données collectées par le télescope ANTARES de 2008 à 2012. Cependant, aucune détection n'a eu lieu et des limites supérieures sur le flux ont été déduites. Ces limites sont en concurrence (dans la gamme dans laquelle les MMs sont visibles dans les détecteurs Cherenkov) avec celles d'autres expériences, et les résultats obtenus ont été publiés sur JHEP.

Cette thèse a porté sur deux thèmes principaux: la simulation du signal produit par un candidat MM lors de son passage dans l'eau et la recherche en données réelles du signal indiquant le passage d'un MM. En ce qui concerne la première partie, une méthode standard qui suppose une interaction MM-matière à travers la section efficace de Mott a été utilisée. De plus, comme suite très importante à cette thèse, une nouvelle simulation a été développée pour décrire ce processus d'interaction à travers la section efficace de KYG. Cette partie (décrite en annexe A) sera utilisée par la collaboration ANTARES pour des recherches ultérieures dans leurs données.

En ce qui concerne la recherche de candidats MMs, une méthode originale (décrite au chapitre 5) basée sur la division en 9 intervalles différents de la gamme de vitesse possible de MMs, à été mis au point. Pour chaque intervalle, les paramètres de recherche ont été optimisés. L'optimisation repose sur le rejet du bruit de fond atmosphérique. La méthode de recherche a été approuvée par la collaboration ANTARES et a été appliqué sur le lot de données.

Aucun MM n'a été détecté et des limites sur le flux ont été établies en fonction de $\beta = v/c$, où v est la vitesses des MMs dans l'eau et c la vitesse de la lumière dans le vide.

Cette thèse est composée de 5 chapitres et 3 annexes. Le premier chapitre porte sur le télescope ANTARES, décrivant sa structure et son principe de détection, tandis que le chapitre 2 décrit la physique des MMs. Le chapitre 3 décrit les aspects pertinents de l'interaction des monopôles magnétiques avec la matière et la détection avec un télescope à neutrinos, alors que le chapitre 4 décrit le traitement et la simulation de données. Enfin, l'analyse des données et les résultats figurent au chapitre 5.

Mots clés : **Monopôle Magnétique, ANTARES, Télescope à neutrinos.**

Acknowledgements

I would like to present my sincere thanks to my professor and supervisor Yahya Tayalati for his support and encouragements throughout this thesis and who allowed me to join a valuable collaboration and do a high quality work. He has the ability to push me forward in order to work harder and make better results. I always take his successes as a physicist as a source of inspiration. Together, we have performed a great job that I will always be proud of.

Thanks to the training and the work I've done in the framework of ANTARES and KM3NeT collaborations, I could improve my knowledge in the fields of neutrino physics and astrophysics.

I'm grateful to Jürgen Brunner who invited me twice to the Center of Particle Physics of Marseille (CPPM) and helped me to accomplish my analysis. He contributed to a large part of this work and thanks to him, I overcame several obstacles in this analysis. Thank you very much Jürgen Brunner, Vincent Bertin, Liam Quinn, Damien Dornic, Alexander Enzenhöfer and all the colleagues in CPPM !

I had the honor to have Antoine Kouchner as a president of jury in my thesis defense. In fact, Antoine always supports me and presents help whenever needed. He had invited me to the laboratory of AstroParticles and Cosmology (APC) and helped me with his team to finish my work. In APC, I was delighted to begin my first mission in KM3NeT thanks to João Coelho who gave me the opportunity to evaluate some Monte Carlo data. So, thank you very much Antoine Kouchner, João Coelho, Bruny Baret, Véronique Van Elewyck and all the colleagues in APC !

I present my special thanks to Maurizio Spurio who provided a very honorable report about my thesis. I have the honor to consider him as a member of the jury, alghough he couldn't be present because of his duties. I appreciate the permanent support and encouragements of Maurizio during my thesis and the knowledge he always shares with me about magnetic monopoles and other topics in astrophysics.

I would like to thank Juande Zornoza who followed this analysis from the beginning, for his remarks and help. I also thank Vladimir Kulikovskiy, Robert Lahmann, Thierry Pradier and all our collaborators in different European laboratories for their significant remarks, help and support. I wish to continue collaborating with all these people in some other works in astrophysics and neutrino physics.

I'm proud to belong to a great laboratory in Oujda, which is the laboratory of Physics of Matter and Radiation. This team is composed of high level professors who never stop supporting young researchers and push them forward. I particularly thank my professors Fouad Fethi, Taoufik Ouali, El Hassan Tahri, Abdelilah Moussa, Hassan Chatei and anyone who tried to help me during my Master and PhD theses. It's been an honor to have El Hassan Tahri, Taoufik Ouali and Abdelilah Moussa in the jury of this thesis. The laboratory allowed me to meet good colleagues who ended up to be among my best friends.

I was very happy to have two great professors from Mohammed V university in Rabat in my thesis jury. Thank you very much Yassine Hassouni and Morad El Baz for being in the jury and for the good reactions and remarks about my dissertation

!. I also want to thank our group in Rabat for their encouragements and for having me several times there.

I present my special thanks to my colleague Anna Pollmann for the helpful interactions and remarks about my analysis and also for explaining the IceCube search for monopoles that she performed. Her reactions toward my analysis were significant and very important. Vielen Dank Anna !

My friends are special, in the sense that they believe in my ambitions and support me to get rid of several obstacles. Those who are in the same field as mine get involved with me in different discussions and sometimes we share the same purposes. Thanks to them, I've never needed to be at the University in order to discuss physics.

Finally, I would like to thank my family which is always supporting me, especially my mother and my brothers. They believe in what I do and they try hard to offer anything I need. Thank you very much Mohammed for providing anything I need and for taking care of me during this thesis. Thank you Jamal, Abderrahman and all family members for your permanent support. Unfortunately, my father died last year, and one of his dreams was to see me graduated. He was so proud of me and I'm grateful to his encouragement and his prayers. This thesis is dedicated to him.

Contents

List of Figures

List of Tables

List of Abbreviations

ANTARES	**A**stronomy with a **N**eutrino **T**elescope and **A**byss environmental **RES**earch
WIMP	**W**eakly **I**nteracting **M**assive **P**article
KM3NeT	**K**ilo**M**eter **3** (cubic) **Ne**utrino **T**elescope
ARCA	**A**stroparticle **R**esearch with **C**osmics in the **A**byss
ORCA	**O**scillation **R**esearch with **C**osmics in the **A**byss
MSW	**M**ikheyev–**S**mirnov–**W**olfenstein
PMT	**P**hoto**M**ulti**P**lier
OM	**O**ptical **M**odule
LCM	**L**ocal **C**ontrol **M**odule
ARS	**A**nalog **R**ing **S**ampler
TVC	**T**ime to **V**oltage **C**onverter
FPGA	**F**ield **P**rogrammable **G**ate **A**rray
DWDM	**D**ense **W**avelength **D**ivision **M**ultiplexing
HV	**H**igh **V**oltage
pe	**p**hoto**e**lectron
MM	**M**agnetic **M**onopole
GUT	**G**rand **U**nified **T**heory
TOE	**T**heory **O**f **E**verything
HPSS	**H**igh **P**erformance **S**torage **S**ystem
MC	**M**onte**C**arlo
DAQ	**D**ata **A**c**Q**uisition

Physical Constants

Speed of Light	$c = 2.997\,924\,58 \times 10^{8}\,\mathrm{m\,s^{-1}}$ (exact)
Fine structure constant	$\alpha = 7.297 \times 10^{-3}$

Dedicated to my dear father.

Introduction

Astrophysics and particle physics provide a good description of the evolution of the Universe. Based on the cosmological model of Big-Bang on the one hand and the standard model of particle physics on the other hand, researchers succeeded in demystifying the evolution of matter surrounding us. These models have been very successful with their predictions that have been verified experimentally. However, the precise description of the very first instants of the Universe always eludes researchers. Physicists are led to introduce hypotheses for scenarios that may have taken place at the beginning of the Universe (inflation [1], CP violation [2], topological defects [3], etc.). These models use energy scales that are beyond those that can be replicated by terrestrial accelerators. Direct astrophysical and cosmological observations are the only way to test these models.

In the context of high energy astronomy, the understanding of the processes involved in powerful cosmic accelerators requires more information than the only observation of photons from the source, for which different mechanisms of production are conceivable. High energy neutrino telescopes are privileged instruments in the current context of astroparticle physics. In addition to having access to the heart of astrophysical objects, thanks to the weak interaction of neutrinos with matter, which allows them to cross very dense regions without interacting, these telescopes can bring very interesting results on the oscillations of neutrinos and on indirect detection of non-baryonic dark matter.

In addition to the detection of high energy neutrinos, neutrino telescopes have a large detection surface that will offer new opportunities, especially for the search for exotic particles, presenting big constraints on the flux. Among all the cosmological observations carried out at present, the investigation of magnetic monopoles is the subject of intensive studies. These topological defects appear in several models of particle physics [4, 5], in which they are inevitably formed during phase transition in the primordial Universe. In addition, topological defects would have played a very important role in the scenarios of the primordial universe and could contribute to the formation of large structures.

Magnetic monopoles are hypothetical particles that carry a magnetic charge, unlike the usual magnets which have two opposite magnetic poles, their existence can give rise to a variety of unusual physical phenomena. In Maxwell's electromagnetism, the electric field is generated by the usual charges which give it a non-zero divergence, but the magnetic field is always of zero divergence because of the absence of the corresponding point charges, the only source of the magnetic field comes from the electric current, that is to say, a movement of electric charges. The existence of magnetic monopoles would thus imply the existence of magnetic currents which would also supply a source to the electric field of a nature different from the usual sources (localized charge or magnetic induction). The properties of magnetic monopoles are the most easily computable among all other topological defects and although they can give a characteristic signal in a particle detector, no experiment has detected them so far. Only limits on their flux with very low values are established [6–9].

High-energy neutrino telescopes such as ANTARES considered in this thesis, offer a new way to search for magnetic monopoles. In this analysis, the aim is to use a collection of five years of ANTARES data recorded between 2008 and 2012 to draw a better limit on the magnetic monopole flux, unless a significant signal above the atmospheric background expectation is observed.

Chapter 1 of this manuscript is intended for the ANTARES telescope installed in the depth of the Mediterranean Sea. We will first present the scientific framework of the experiment and the different issues and objectives. Then we will describe the geometry of the telescope, its detection principle, its performance and the data acquisition system.

Chapter 2 introduces the theoretical framework of magnetic monopoles and their effect, especially the symmetry of Maxwell equations and the quantization of electric charge. Then, the theoretical and experimental constraints on their flux will be presented, as well as the various experimental researches carried out. Afterwards, the interaction of magnetic monopoles in matter, their energy loss in water and their signal in a neutrino telescope will be discussed in chapter 3.

In chapter 4, we will discuss the simulation performed, our strategy of reconstruction and data processing, as well as the trigger efficiency of the detector to these particles.

Two different analyses were carried out, according to the speed range of the magnetic monopoles divided into two regions. The first analysis is intended for magnetic monopoles below the Cherenkov threshold, while the second one studies relativistic monopoles whose speed exceeds the Cherenkov threshold. These analyses, as well as the results obtained after using five years of ANTARES data, will be presented in Chapter 5. Finally, we give a summary of the analyses performed and the prospective studies.

Chapter 1

The ANTARES telescope

1.1 Introduction

Many scientific experiments are concerned with the detection of messengers of cosmic phenomena, such as the HESS gamma ray telescope [10], AUGER [11] for charged nuclear particles, IceCube [12] and ANTARES [13] for cosmic neutrinos, or LIGO [14] and VIRGO [15] that made a first detection of gravitational waves recently [16]. The study of cosmic radiation represents an important step in understanding the Universe.

Neutrinos, unlike cosmic rays that are sensitive to the magnetic fields of the Universe, and unlike photons that are easily absorbed by the interstellar medium, are able to escape from the core of the most compact astrophysical objects and travel without being deflected by magnetic fields, or even absorbed by clouds of interstellar matter. However, due to their low interaction with matter, the detection of neutrinos requires huge detectors, often installed in a hostile environment, and whose construction represents a real technological challenge. The primary aim of the ANTARES (Astronomy with a Neutrino Telescope and Abyss environmental RESearch) experiment is to use neutrinos as a tool to study particle acceleration mechanisms in energetic astrophysical objects such as active galactic nuclei and gamma-ray bursts, which may also shed light on the origin of ultra-high-energy cosmic rays. At lower energies, non-baryonic dark matter (WIMPs) may be detected through the neutrinos produced when gravitationally captured WIMPs annihilate in the cores of the Earth and the Sun. Neutrino oscillations can be measured as well, by studying distortions in the energy spectrum of upward-going atmospheric neutrinos.

1.2 The collaboration

The ANTARES collaboration is composed of around 150 engineers, technicians and physicists from 29 institutes. The map of the countries involved in this project is shown in Fig. 1.1.

Morocco has joined the collaboration in 2011, represented by Mohammed I University in Oujda. Afterwards, Mohammed V University in Rabat has also taken part in the collaboration, then Cadi ayyad University of Marrakesh and the National Center of Energy, Sciences and Nuclear Techniques CNESTEN.

Meanwhile, the group is participating in the development of the future kilometer-sized telescope being deployed in the Mediterranean in the framework of KM3NeT collaboration [17]. This new collaboration aims to develop two neutrino telescopes;

FIGURE 1.1: The ANTARES collaboration map.

ARCA (Astroparticle Research with Cosmics in the Abyss) that is dedicated to the search for very high-energy cosmic neutrinos and ORCA (Oscillation Research with Cosmics in the Abyss) that will be devoted to the study of the fundamental properties of neutrinos, exploiting the abundant flux of neutrinos produced in the interactions of the cosmic rays with the atmosphere. Further information about the new experiment KM3NeT is presented in Appendix. C. In addition to Oujda and Rabat, Cadi Ayyad University in Marrakech has also joined the KM3NeT collaboration, making a larger representation of Morocco.

1.3 Scientific framework of the experiment

The aim of the ANTARES experiment revolves three topics: particle physics presenting one of the biggest challenges currently which is neutrino oscillation, particle astrophysics trying mainly to solve the mystery of dark matter, and astronomy.

1.3.1 Neutrino oscillations

The neutrino has been reported for the first time in nuclear physics, particularly in beta decay where a nucleus of atomic number Z transforms into a nucleus of atomic number Z + 1 with emission of an electron. For example, carbon 14 is converted to nitrogen 14 according to the reaction:

$$C_6^{14} \rightarrow N_7^{14} + e^- \tag{1.1}$$

In Beta decay the daughter nucleus has less mass than the parent. According to Einstein's $E = mc^2$, it is expected that the electron would carry off the difference in masses in the form of kinetic energy. However, instead of all electrons having the same energy, there was a continuous distribution, as shown in Fig. 1.2.

This result was unexpected and with no explanation, there were even suggestions that energy conservation did not hold at the atomic level. However, in 1930,

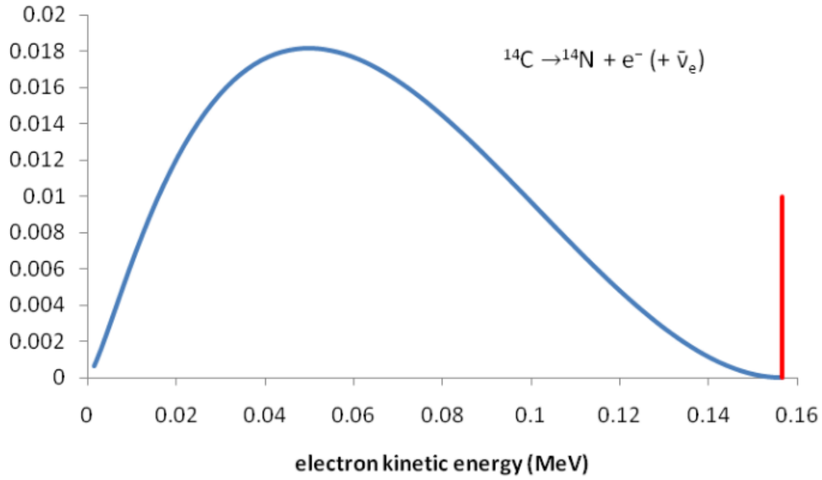

FIGURE 1.2: Electron energy spectrum for beta decay of carbon-14. The red line marks the expected electron energy if only an electron was emitted. The blue line shows the observed electron energies.

Wolfgang Pauli wrote a famous letter to a conference in Tübingen[1], in which he proposed the existence of a light neutral particle (neutrino) of spin 1/2 emitted alongside the electron in beta decay. Thus, the available energy is split between the electron and the undetected neutral particle, this explains the continuous spectrum and also solves a couple of more technical non-conservation problems.

The neutrino was then introduced by Fermi in his theory of Beta decay [18], establishing its existence in nuclear and particle physics. The issue with this particle was that it could never be detected, which made physicists worried about the failure of the new theory. Fortunately, with the advancement of nuclear fission in the 1930s and 1940s, the experimental detection of these elusive particles was established. Nuclear fissions offered an intense source of neutrinos.

According to the minimal standard model, neutrinos are strictly massless, but physicists realized that this idea should be reviewed with the appearance of the so-called the Solar Neutrino Problem. Indeed, neutrino astronomy experiments showed that the flux of electron neutrinos from the Sun was lower than expected. Later on, this problem has been explained by neutrino oscillations either in vacuum or more probably within the Sun itself, enhanced by the high electron density in the solar core (the MSW effect [19]).

Neutrino oscillation solutions to the solar neutrino problem involve the conversion of electron neutrinos into some other flavour. Recent measurements of the Super-Kamiokande neutrino detector [20] seem to indicate the existence of atmospheric muonic neutrino oscillations. This result is based on the observation of an asymmetry between the ascending and descending muonic events. Other experiments support this result [21, 22].

The phenomenon of quantum oscillation occurs between particles whose mass eigenstates are different from the eigenstates of flavors. If the oscillations are confirmed, this inevitably implies that the neutrinos have a mass.

---

[1] It's a German university town.

In the simple case of a mixture of two flavors of ν_α and ν_β neutrinos, the eigenstates of flavors can be decomposed into a linear combination of the mass eigenstates ν_1 and ν_2 (of mass m_1 and m_2 respectively), via an unitary mixture matrix:

$$\begin{pmatrix} \nu_\alpha \\ \nu_\beta \end{pmatrix} = \begin{pmatrix} \cos\theta & \sin\theta \\ -\sin\theta & \cos\theta \end{pmatrix} \begin{pmatrix} \nu_1 \\ \nu_2 \end{pmatrix} \tag{1.2}$$

where θ is the mixing angle. The time evolution equation of the mass states makes it possible to calculate the transition amplitude from ν_α to ν_β:

$$\langle \nu_\beta | \nu_\alpha \rangle = -\cos\theta \sin\theta \exp(\frac{-iE_1 t}{\hbar}) + \sin\theta \cos\theta \exp(\frac{-iE_2 t}{\hbar}) \tag{1.3}$$

and to deduce the transition probability:

$$P(\nu_\alpha \to \nu_\beta) = \sin^2(2\theta) \sin^2[1.27 \frac{\Delta m^2 (eV^2) L(km)}{E_\nu (GeV)}] \tag{1.4}$$

where $\Delta m^2 = \mid m_1^2 - m_2^2 \mid$ is the squared mass difference.

For neutrinos produced in the atmosphere, the distance L extends between 15 km (downward vertical trajectory) and almost 13000 km (upward vertical trajectory). Super-Kamiokande data show asymmetry for the muon events, but not for the corresponding electronic events. Current data imply the disappearance of muon neutrinos, most probably due to oscillations $\nu_\mu \leftrightarrow \nu_\tau$, with $\sin^2 2\theta > 0.88$ and $1.6 \times 10^{-3} < \Delta m^2 < 4 \times 10^{-3} eV^2$ at 90% confidence level; the most likely parameters being a total mixture ($\sin^2 2\theta = 1$) and a squared mass difference $\Delta m^2 \approx 2.5 \times 10^{-3} eV^2$ [20].

Fig. 1.3 shows that at low energy the averaged effect of atmospheric neutrino oscillations is observed as a decrease in flux. High energy neutrino telescopes that are sensitive to values of $x = E/\cos\theta > 20 GeV$, can record both a maximum and a minimum of this survival probability.

1.3.2 Astronomy and astrophysics

High energy neutrinos are generated through the interaction of protons accelerated from astrophysical objects with matter or radiation. These proton interactions produce essentially pions, whose leptonic decay modes yield neutrinos. Thus, several astrophysical neutrino sources are involved.

Compact objects, such as neutron stars or black holes, accrete matter from their normal companion stars leading to plasma waves in the a strong magnetic field, which bring protons to high energies by stochastic acceleration. Interactions of the accelerated particles with the accreting matter or with the companion star would then produce a neutrino flux comparable to that in high-energy particles with a spectral index close to 2.

The Explosions of massive stars known as supernovae lead to an acceleration of high energy particles. The supernovae could leave a neutron star which is detectable as a pulsar in some cases. Different mechanisms could take place to accelerate protons in the supernovae shells, which interact with the matter of the shell giving rise

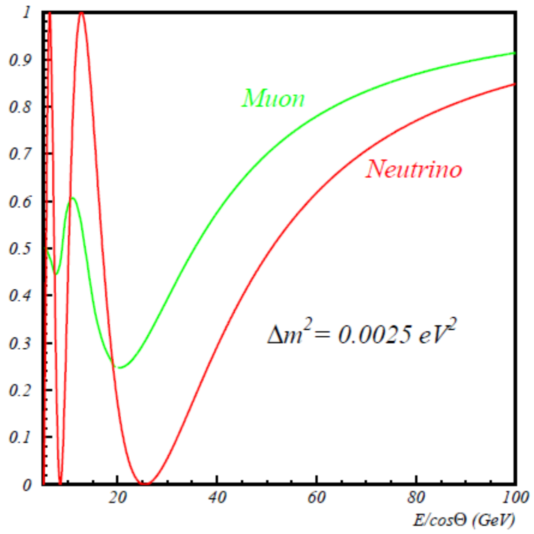

FIGURE 1.3: Probability of survival of ascending neutrinos as a function of $x = E/\cos\theta$, when x is given by the true values of the neutrinos or for the corresponding values of the muons they generate.

to charged and neutral pion decays producing neutrinos and photons respectively. The observation of these neutrinos would provide a clear indication of proton acceleration with the direction identifying the source.

1.3.3 Cosmology and dark matter

In recent years it has become generally accepted by astrophysicists that most of the matter in the universe is non-luminous "dark matter”. The clearest evidence for this is the observed flatness of the rotation curves of disk galaxies, which imply a dynamical mass far in excess of that accounted for by the constituent stars and gas. Constraints from the observed abundances of light elements indicate that much of the dark matter in the cosmos must be non-baryonic. No presently known particle has the required properties, but a good theoretical candidate is the stable neutral particle expected in most versions of supersymmetry theory.

Supersymmetric WIMPs accumulate in the cores of the Sun and the Earth or in the centre of the Galaxy through gravitational capture. The resulting high space density leads to annihilation reactions, which will yield high-energy neutrinos through the decays of the gauge bosons and heavy particles produced. These neutrinos could be detected by the ANTARES telescope over a useful range of WIMP masses. The detection and identification of a relic cosmological population of supersymmetric particles would be of immense importance to both cosmology and particle theory.

1.4 Detection principle

The principle of neutrino telescopes is based on the use of a three-dimensional network of photomultipliers installed within a very large volume of a natural transparent medium, such as a lake, the sea, or the ice, this is to detect Cherenkov radiation from leptons, products of neutrino interactions by charged current. The Earth is used both as a target for neutrinos and as a shield against all particles other than neutrinos (Fig. 1.4).

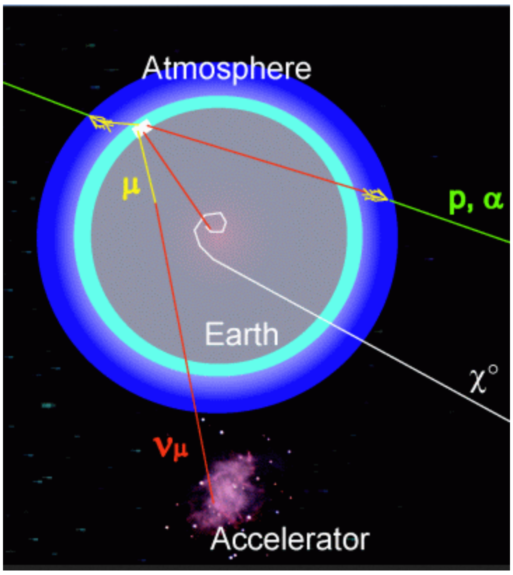

FIGURE 1.4: A neutrino telescope uses the detection of upward-going muons as a signature of muon neutrino interactions in the matter below the detector.

A large target dense volume is needed because of the very weak interaction of neutrinos with the material. This detection technique requires discriminating upward going muons against the much higher flux of downward atmospheric muons (see Fig. 1.5).

In order to correlate the measured muon spectrum with the original neutrino spectrum, it is necessary to understand the dynamics of neutrino interactions, the opacity of the Earth, the energy loss of muons and the resolution of the detector over a wide range of angles and energies.

1.4.1 Neutrino interactions in ANTARES

A neutrino of $10^{12}eV$ has a mean free path of about $3 \cdot 10^{11} g.cm^{-2}$, whereas the Earth's diameter is equivalent to $5 \cdot 10^{9} g.cm^{-2}$. Consider a neutrino (anti-neutrino) emitted by a source, it will propagate with few interactions to the Earth, where it will weakly interact with it by charged current: $\nu_l(\bar{\nu}_l) + N \rightarrow l(\bar{l}) + X$, or by neutral current: $\nu_l(\bar{\nu}_l) + N \rightarrow \nu_l(\bar{\nu}_l) + X$, where l is a charged lepton, ν a neutrino, N is a nucleon and X is a hadronic sheaf.

Charged-current ν_e interactions give rise to electromagnetic and hadronic showers with longitudinal dimensions of no more than a few metres, because the radiation length and the nuclear interaction length of water are below 1 m. On the scale of ANTARES, these are nearly point-like events. At energies above 100 GeV, the energy resolution of these events is expected to be better than for muon events because they leave all of their energy inside the detector volume. On the other hand, their angular resolution will be poor compared to muon events, due to the point-like character of the showers. Charged-current ν_e interactions will be contaminated

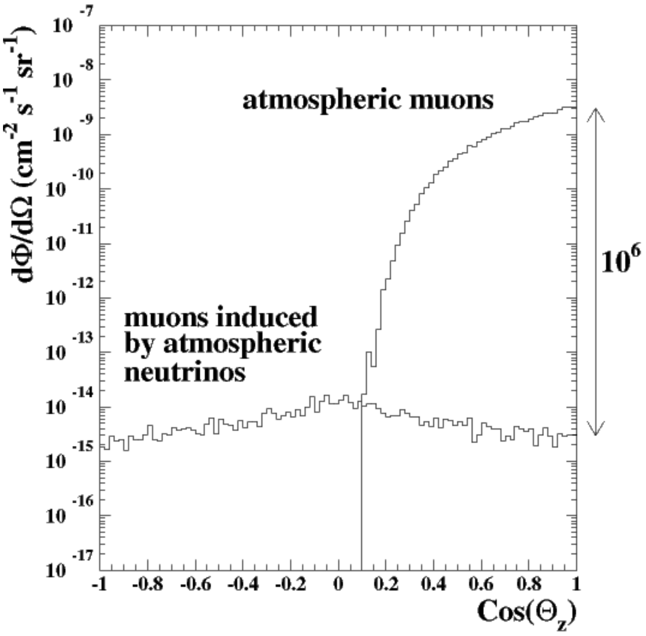

FIGURE 1.5: The flux of atmospheric muons and neutrinos as a function of the cosinus of their zenithal angle.

by neutral-current interactions of both ν_e and ν_μ(and ν_τ, if present). The number of neutral-current interactions is about 1/3 of the number of charged-current interactions. The neutrino type is not identified in the neutral-current interactions, the energy resolution is poor due to the missing final-state neutrino, and the angular resolution is poor due to the point-like character.

Charged-current ν_μ interactions produce $\mu^\pm$ leptons as well as a point-like hadronic shower. The ν_μ energy can be estimated from the measured $\mu^\pm$ energy. In $\nu_\mu d \rightarrow \mu^- u$ interactions, the average μ^- energy is 1/2 of the ν_μ energy; in $\bar{\nu}_\mu u \rightarrow \mu^+ d$ interactions, the average μ^+ energy is 3/4 of the $\bar{\nu}_\mu$ energy. The $\mu^\pm$ energy can be determined from the range for $E < 100$ GeV, or from dE/dx for $E > 1 TeV$. For ν_μ interactions inside the detector, additional information on the ν_μ energy is available from the hadronic shower. The ANTARES detector is designed for the detection of these charged-current ν_μ interactions.

Charged-current ν_τ interactions produce $\tau^\pm$ leptons with electronic, muonic and hadronic decay modes. The ν_τ interaction vertex and the $\tau^\pm$ decay vertex cannot be separated for energies below around 100 TeV. The electronic and hadronic modes will look like ν_e charged-current or neutral-current interactions. The muonic decays $\tau^- \rightarrow \mu^- \bar{\nu}_\mu \nu_\tau$, with branching ratio 17%, will be visible in ANTARES, but they cannot be distinguished from ν_μ interactions.

Among all neutrino flavors, muon neutrino interactions far away from the detector can be observed due to the long range of the muon. The other leptons have shorter ranges due to the low energy (electron) or the short lifetime (tau), making the detection of other neutrino flavors weak in terms of efficiency and angular precision. Hence, only the muon channel will be considered in the following.

1.4.2 Cherenkov light emission

A charged particle crossing a medium of index n, with a speed $v = \beta \cdot c$, greater than the speed of light ($\frac{c}{n}$) in the medium, induces the propagation of an electromagnetic wave (see Fig. 1.6).

The first observational study of this phenomenon was undertaken by Mallet between 1926 and 1929. But it was only between 1934 and 1944 that Cherenkov conducted the study of this radiation [23]. He analyzed, among other things, the angular distribution, the dependence with n and β of the radiation, and showed that the intensity of the wave is proportional to the distance traveled. The relation bearing his name is written as:

$$\cos\theta = \frac{1}{n \cdot \beta} \tag{1.5}$$

where θ is the angle between the particle and the direction of the light emitted.

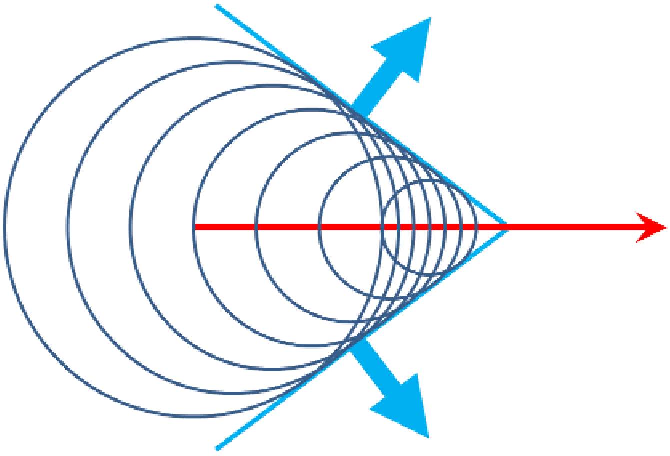

FIGURE 1.6: Representation of the Cherenkov light.

In the energy range interesting for ANTARES ($E > 10$ GeV), particles will generally be ultra-relativistic with $\beta = 1$. The refractive index of sea water is n = 1.35 for a wavelength of 450 nm, therefore, the Cherenkov light is emitted under 42° for this wavelength. This easy geometrical pattern of light emission allows a precise reconstruction of tracks from the measurement of only few hits at different space points.

Considering a homogeneous medium of index n, the Cherenkov emission of the particle is done symmetrically with respect to its direction of propagation. A cone of light is thus formed, also called a Cherenkov cone of angle θ_c constant with respect to the propagation of the particle, as illustrated in Fig. 1.6.

Fig. 1.7 illustrates the neutrino detection with an undersea neutrino telescope.

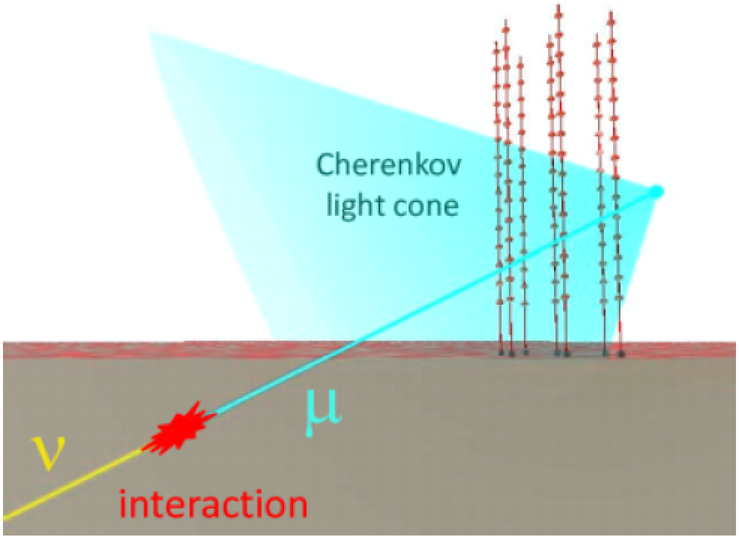

FIGURE 1.7: Representation of the detection principle of a neutrino by a telescope. The incoming neutrino interacts with matter below the detector giving rise to a muon which propagates in water emit a Cherenkov light cone.

The number of photons produced along a flight path dx in a wave length bin $d\lambda$ for a particle carrying unit charge is :

$$\frac{d^2N}{d\lambda dx} = 2\pi\alpha \sin^2\theta/\lambda^2.$$

Cherenkov photons emitted during the crossing of a muon, will spread differently depending on the optical properties of the medium through. Several measurement campaigns were carried out on the ANTARES site between 1997 and 2000, in order to characterize the optical properties of the water, and in particular the attenuation length of the light. The effective attenuation length L_{att} corresponds to the distance for which the luminous intensity has decreased by a factor $1/e$. It is a function of the absorption length L_{abs} as well as the scattering length [2] L_{scatt}, such that:

$$\frac{1}{L_{att}} = \frac{1}{L_{abs}} + \frac{1}{L_{scatt}}. \tag{1.6}$$

The attenuation length enters into the definition of the luminous intensity I function of the distance R at the source of emission, of intensity I_0, and is expressed for an isotropic source such that:

$$I(R) \propto \frac{I_0}{R^2} \exp^{-\frac{R}{L_{att}}}. \tag{1.7}$$

---

[2] The scattering length is the average length between two scatterings.

By measuring the number of photons as a function of the distance to the source, the measurements made on the ANTARES site give an attenuation length of the order of 50 m for a wavelength of 473 nm (blue).

One can, moreover, note the phenomenon of chromatic dispersion, related to the group velocity v_g of light in water [24], characterized by the group refractive index $n_g = c/v_g$. The index n_g varies with the wavelength, and is about 1.38 for 460 nm [25]. This dependence causes a dispersion phenomenon, which causes, for a distance of 150 m, a longer arrival time of photons up to 2 ns [25].

1.5 Detector description

The construction of the detector was completed on May 30, 2008, after several phases of construction. The ANTARES detector is located at 42° 50′ N and 6° 10′ E, in France, 40 km off Toulon (see Fig. 1.8). This area was chosen for its relatively flat ground (inclination of a few meters per 100 m^2 of surface), and its depth of about 2500 m, which allows to get rid of sunlight and a large part of muons created in the atmosphere. In addition, its proximity to the coast allows for deployment and maintenance operations, much more simply.

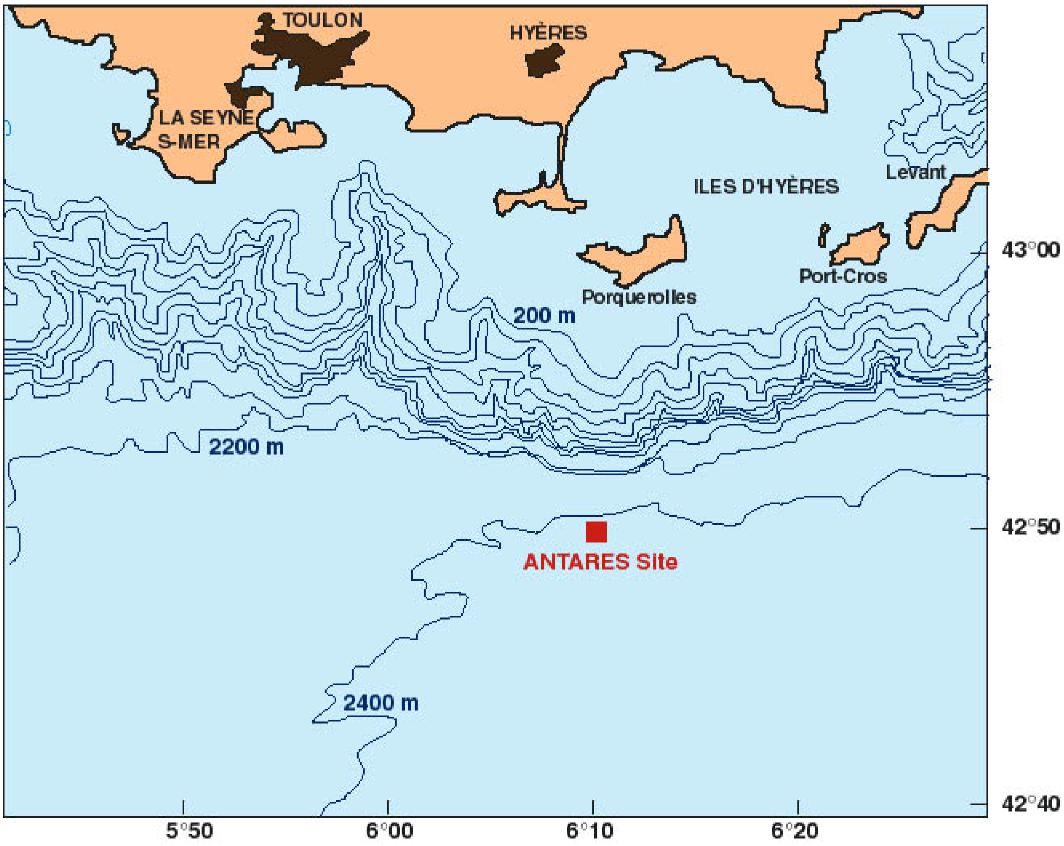

FIGURE 1.8: The ANTARES site.

1.5.1 Detector layout

The telescope is composed of a network of 885 photomultipliers distributed over a large area. These 10" photomultipliers (PMT) (Hamamatsu R7081-20), sensitive in the wavelength region of *[300, 600] nm* are surrounded by a 17" diameter glass sphere, to which they are glued using a transparent gel, whose refractive index of 1.404 is between that of the sphere of 1.47 and the water of about 1.35, to reduce the reflection of light on its surface. PMTs are further protected by a mu-metal grid to limit the effects of the Earth's magnetic field, and are connected to the electronics needed to provide them with high voltage. One can also note the presence of an internal LED used to control the evolution of the transit time in the phototube of the PMTs. This set is called Optical Module (OM) [27], and is shown in Fig. 1.9. The OMs are oriented at about 43° from the vertical towards the ground and their upper hemisphere is painted in black, in order to decrease the sensitivity to the photons arriving in the opposite direction.

FIGURE 1.9: A picture of an Optical Module showing also its components.

Three OMs form a group, called storey (or floor). The latter, shown in Fig. 1.10, also consists of a titanium cylinder, called LCM (Local Control Module), responsible for the distribution of current to OMs, digitization and signal processing, and the sending of data to the shore station. Each LCM contains an inclinometer and a compass, which measure the three-dimensional orientation of a floor, and electronic boards that check that it is working properly (temperature, voltage, current and humidity measurements).

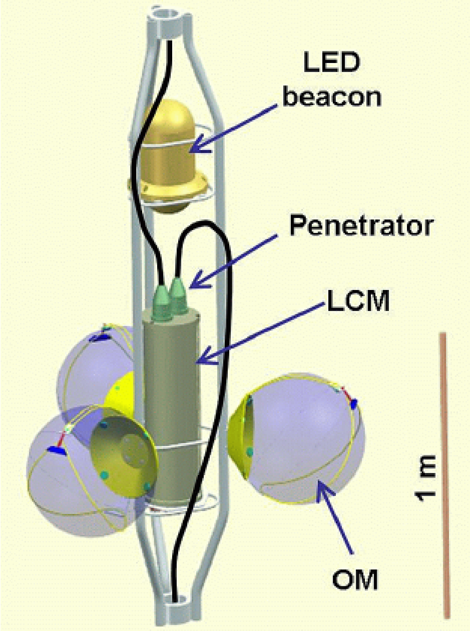

FIGURE 1.10: A storey equipped with the 3 OMs, the LCM and an LED beacon.

The floors are 14.5 m apart, and are interconnected by electromechanical cables. They constitute a set of 25 levels, named "lines". These lines are held on the ground by a lead base, and remain almost vertical with the help of a buoy (see Fig. 1.11). The latter are not rigid, and move slightly with the sea currents. On each of them are distributed five hydrophones, as well as four LED systems, called LED Beacons [28], in order, respectively, to know the shape of the line, and to carry out an in situ calibration of the OMs of the detector.

On each foot of line is fixed a transceiver hydrophone, which allows to position the location of the lines, and to send signals to the five receivers distributed on the lines. Finally, the lines are connected to a junction box, which is connected by a 42 km long electro-optical cable to the control center, located at La Seyne sur Mer. Fig. 1.12 shows the ANTARES detector as a whole.

The lines have been designed so that a recovery, repair, redeployment of each one of them is possible.

1.5.2 Acquisition system

Each photomultiplier is "read" by two ARS (Analog Ring Samplers) [30, 31], electronic cards that are used for digitizing the signal at the output of the PMT. As soon as the voltage coming from the PMT exceeds a threshold of 0.3 photoelectron (pe), a "hit", containing the integrated charge on the anode during a time interval of $\approx$ 33 ns, with $\approx$ 8 ns before the passage of the threshold and $\approx$ 25 ns after, and time given by the internal clock of the LCM, is created by the ARS. Time labeling is made possible by a TVC (Time to Voltage Converter), available for each ARS, that interpolates the time between two local clock pulses of 50 ns, with a precision less than one nanosecond. The local clock of each LCM is, in turn, regularly synchronized with

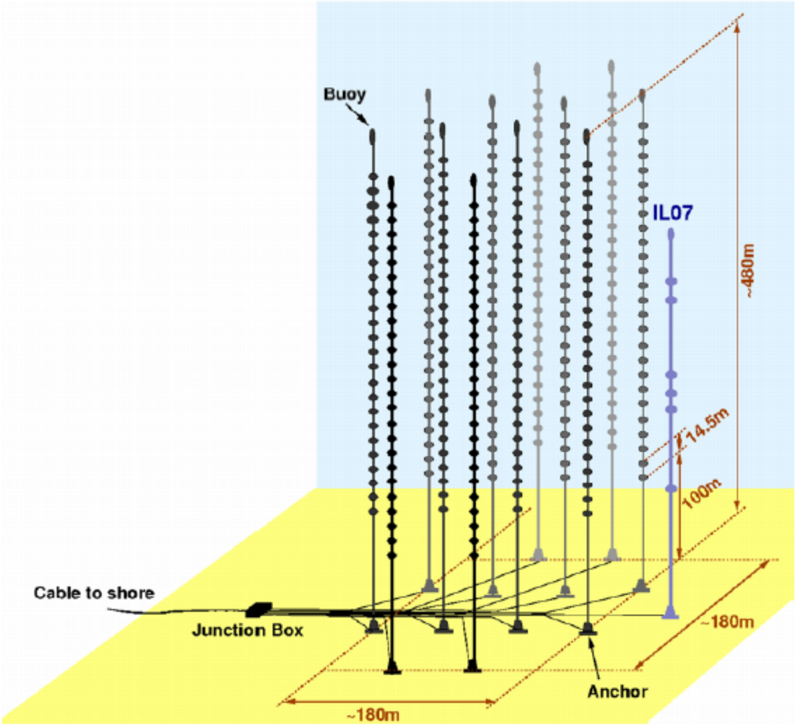

FIGURE 1.11: Illustration of the ANTARES detector.

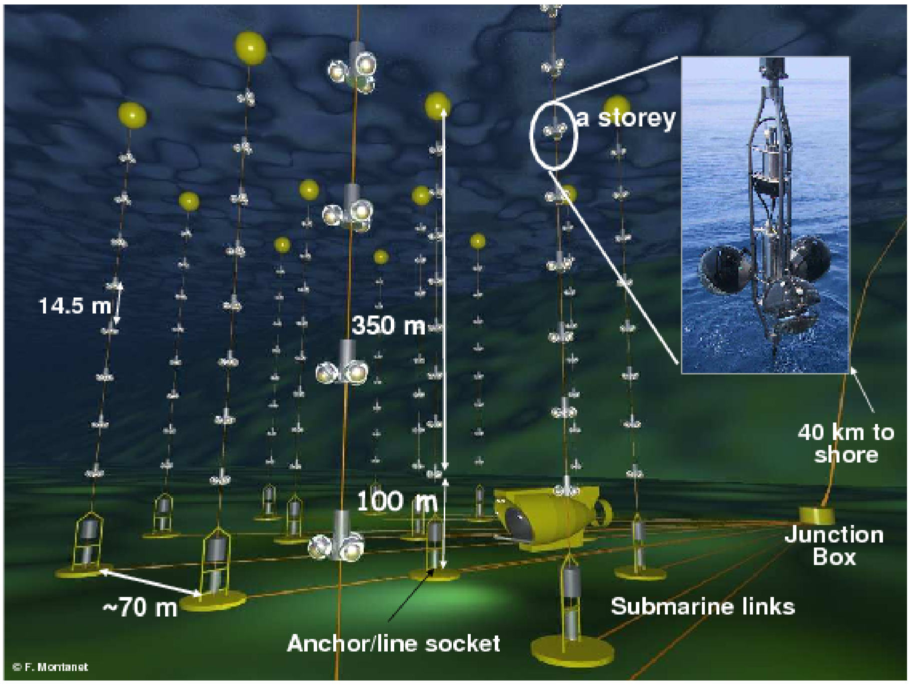

FIGURE 1.12: Illustration of the ANTARES telescope.

the master clock of the control station.

After integration and signal conversion, a dead time of about 250 ns results for an ARS. In order to compensate for this dead time, two ARSs are connected in parallel by a logic "token ring", which carries out the permutation from one ARS to the other. The dead time between the first and the second signal is then about 40 ns[3], and about 250 ns between the first and the third signal.

The reading of the ARS pair is performed by a Field Programmable Gate Array (FPGA), which groups the digitized data in packets of 104 ms, and which are then sent to one of the LCMs, called MLCM (Master Local Control Module).). The MLCMs, which are one in each sector (grouping 5 consecutive floors), include the same components as the LCMs, but also an ethernet switch, and a demultiplexing system, a DWDM (Dense Wavelength Division Multiplexing), which allows to collect the data of the five floors in a single package and send it in the same bandwidth to the shore station. Fig. 1.13 shows a schematic view of the components present in an LCM.

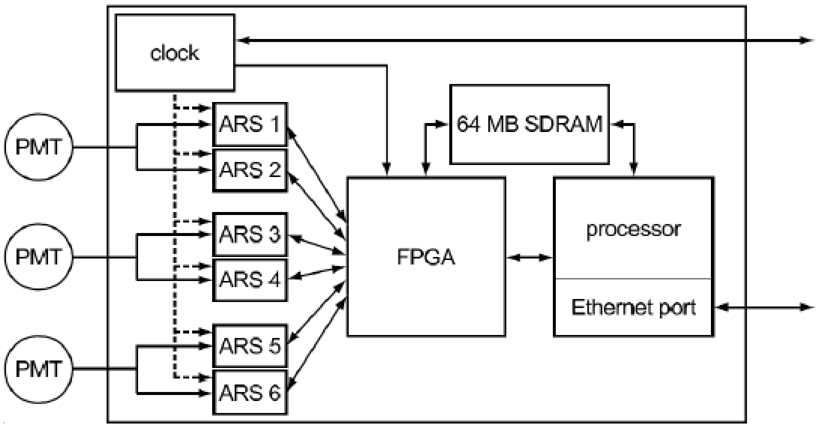

FIGURE 1.13: Schematic view of the components present in an LCM.

Finally, a computer farm located at the shore station, combines the simultaneous packets from each PMT in a time window of 104 ms. Thus, each of these packets may contain several muon events, the latter having a detector traversal time of the order of 2 μs.

The majority of data sent is due to the surrounding background noise. The computer farm therefore applies in real time various triggers[4], selecting events that may correspond to the passage of a muon in the detector. The trigger system will be further discussed in 1.7. The algorithms seek for time and position-related hits, which will usually be the result of the passage of a muon into the detector, due to the properties of the Cherenkov light emission. In ANTARES, the notion of event corresponds to the time window in which the hits were selected by a trigger, to which are added a time window of 2.2 μs before the first triggered hit, and a time window

---

[3] The $\approx$ 40 ns of dead time come from the signal integration time of about 33 ns and the ARS permutation time of about 10 ns.

[4] Criteria of selecting events.

of 2.2 μs after the last trigged hit. This large time window is commonly called the snapshot.

1.5.3 Acoustic positioning

Unlike a rigid telescope, the lines in ANTARES move according to the direction of the currents and their forces[5]. However, the reconstruction of the trajectories of the incident particles, from the light detected by the optical modules, requires a good knowledge of the relative position of the latter in space. To obtain a precision of the order of one nanosecond on the photon arrival time on the PMTs, required by the reconstruction, it is necessary to have a precision of 22 cm on the position of the optical modules. For this, on each line foot, was installed an acoustic transceiver hydrophone, broadcasting high frequency signals from 40 to 60 kHz per cycle of one to two minutes. The five receiver hydrophones arranged on each sector[6] of a line, thus detect the acoustic signal, and, by triangulation, knowing the speed of sound in the medium, the shape of the line is reconstructed. Fig. 1.14 illustrates the horizontal displacements of the hydrophones of line 4 during two months of data taking.

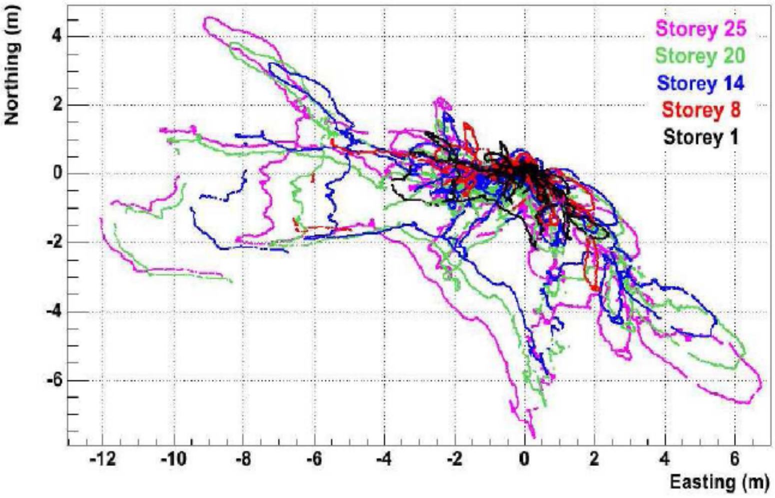

FIGURE 1.14: the horizontal displacements of the hydrophones of line 4 during two months of data taking.

The estimated accuracy on the measurement is of the order of 6 *cm* for the most distant storeys from the line foot, and is mainly due to the uncertainties of measurement of the apparatus, and to the uncertainty on sound speed [29].

1.5.4 Timing calibration

In the timing calibration [32], the master clock provides a common synchronization signal to the whole apparatus. It can be used to measure the time path from shore to each electronics module. Such information is useful to check the overall stability of the system and to measure the in situ time delays after the connection of a detector line. Fig. 1.15 shows the round trip time measured for one electronics module.

---

[5] This unstable configuration of the telescope has been taken into account in the simulation part by introducing a "smart" strategy named run-by-run, which will be explained in chapter 4.

[6] a line is composed of 5 sectors, which contain 5 consecutive floors.

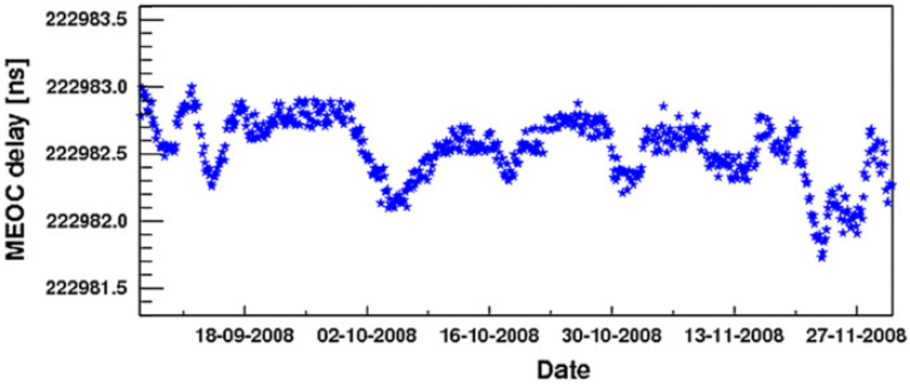

FIGURE 1.15: Round trip time for clock signals between shore and one of the electronics module of the apparatus.

Using the optical beacons installed on the lines and the LED pulsers mounted inside each Optical Module, the time offsets for each specific channel are then calibrated in situ. This includes LED beacons, distributed at different levels along each line, and two laser beacons located at the bottom of two central lines. The laser beacons are mainly used for cross-check of the timing calibration of the OMs of different lines, while the LED beacons remain the main tool for in situ timing calibration. These beacons are flashed in turn for short time periods in order to illuminate the surrounding optical modules. From the comparison between the measured and the expected time of the hits, taking into account the propagation time of the light, one can infer the time offset for each OM.

Fig. 1.16 shows the time residual distribution for one particular OM obtained from one calibration run. The tail on the right part of the distribution is attributed to light scattering.

The position of the leading edge is determined with a Gaussian fit to the left part of the distribution, which is less affected by scattering. The distribution of the leading edge as a function of the distance (or, equivalently, the storey number) shows a linear trend, which is ascribed to the "early-photon effect". This effect is due to the duration of the light pulse ($\approx 4\ ns$) and to the intensity of the detected light. The closer the OM, the more light it receives and therefore the sooner the PMT signal passes the preset threshold of the ARS, an effect which is further emphasized by time walk. A straight line fit is then applied to the data and deviations from this fit are understood as the corrections to be made on the time offsets obtained by the calibration onshore. An example is given in Fig. 1.17.

In most cases these corrections are small, and only for $\approx$ 15% of cases they are larger than 1 ns. This method provides an average improvement of $\approx 0.5ns$ over the timing calibration performed onshore.

The time offset variations of each optical module, due to variations in the transit time of the photomultiplier for instance, can be monitored by operating the LED

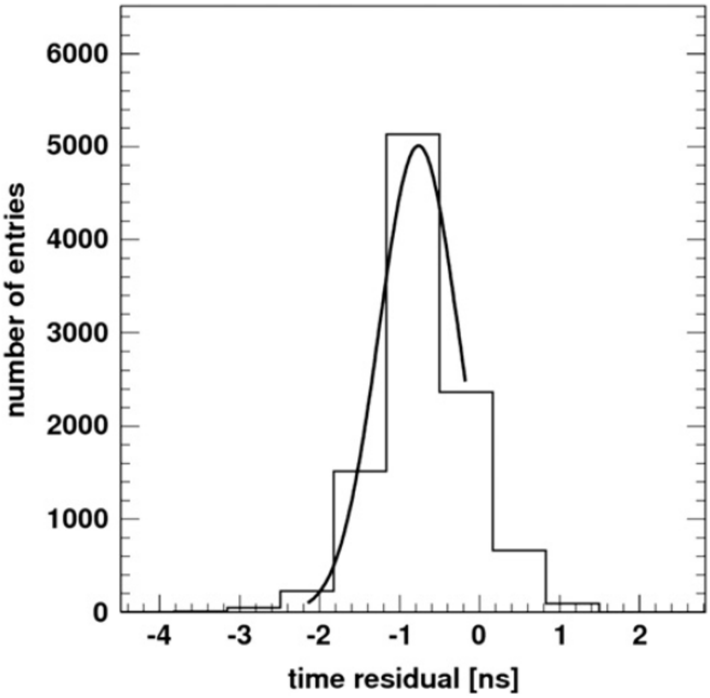

FIGURE 1.16: Time residual distribution of the signals in an OM located two storeys above a flashing LED Beacon. The curve is a Gaussian fit with a sigma of 0.5 ns.

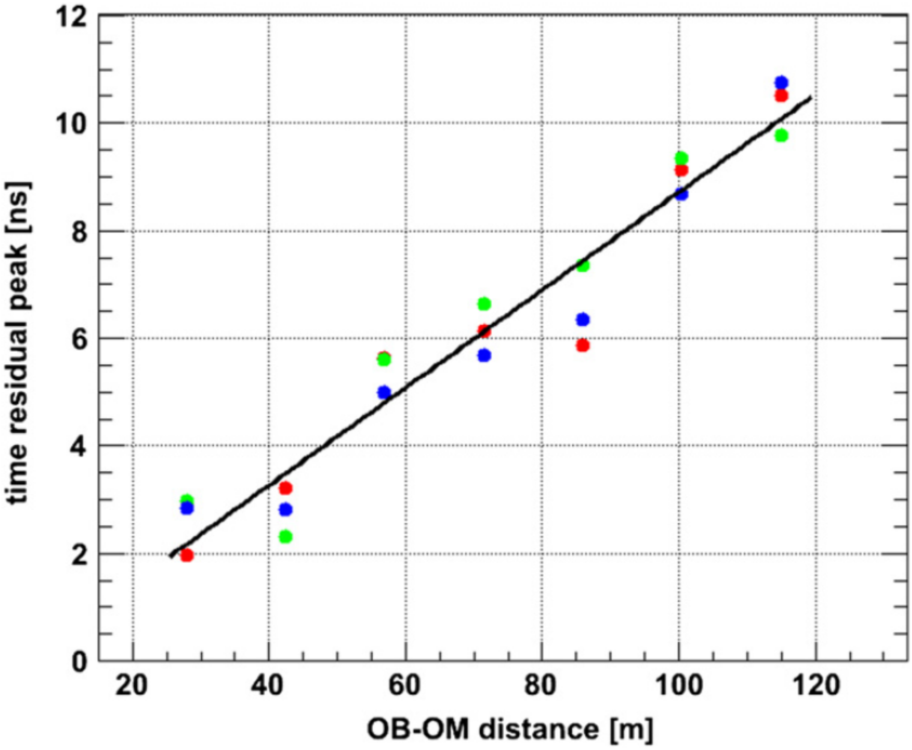

FIGURE 1.17: Time residual peak position as a function of the distance between a flashing LED beacon and the OMs along seven storeys above. The three points at each distance correspond to the three OMs in each storey. The additional delay with distance is due to the early photon effect.

pulser placed in each optical module. These data show a good stability of the time delays when the HV of the PMT and the settings of the ARS are not changed.

1.6 Detector performance

The ANTARES detector is particularly sensitive to up-coming particles, in particular because of the inclination of the OMs of the detector, to ≈ 43° with respect to the axis of the line, towards the ground.

Muons are mostly produced in the atmosphere by the decay of charged and neutral mesons, resulting from the interaction of cosmic rays with the present nuclei, giving rise to hadronic sheaves. Muons are the only particles produced in the atmosphere, with the neutrinos, to be able to reach the ANTARES detector, and to emit a characteristic signal. An exponential decay of their flux with the depth of water crossed is observed, as shown in Fig. 1.18 [33], as a result of significant energy losses due to Bremsstrahlung, the production of e^- e^+ pairs and photo-nuclear interactions.

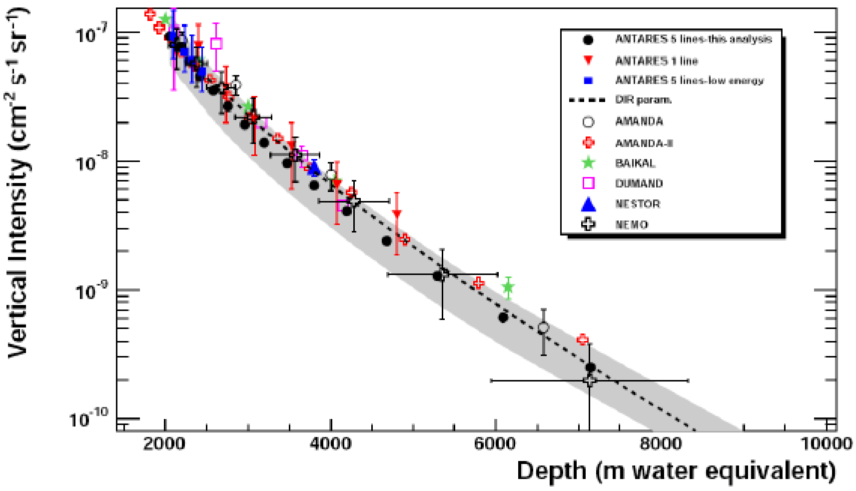

FIGURE 1.18: Flux of atmospheric muons from measurements made with the detector's 5-line configuration in 2007 (black dots) as a function of traversed water depth. The red triangles pointing down show the results from the one-line configuration data taken in 2006 [34]. The blue squares show the results obtained with a method that selects low energy muons [35]. The expected stream from the Bugaev parameterization (dashed line) is superimposed [36]. A compilation of the results obtained with other underwater detectors is shown: AMANDA [37], AMANDA-II [38], Baikal [39], DUMAND [40], NESTOR [41], NEMO [42].

1.6.1 Optical background

The light produced by the passage of muons in seawater is not the only one detected by photomultipliers. Most of the photons come from the beta decay of potassium 40 (K^{40}), and from bioluminescent organisms. Seawater contains about 400 ppm of potassium [43], including the radioactive isotope K^{40} with a proportion of ≈ 0.0117%. This isotope decays mainly in Ca^{40} (89.3%) [44], emitting an electron, whose maximum energy is 1.311 MeV, greater than the energy required to cross the Cherenkov threshold of ≈ 1.13 MeV for an electron.

$$K^{40}_{19} \rightarrow Ca^{39}_{20} + e^{-} + \bar{\nu}_e. \tag{1.8}$$

Each decay of K^{40} will emit Cherenkov photons that are visible to PMTs [45]. The background noise level visible by the PMTs, and coming from K^{40} is about 30 +/- 7 kHz.

Another source of background comes from bioluminescent organisms, such as bacteria and shrimp. The presence of bioluminescent microorganisms produces a variable background noise, generally of the order of 30 kHz on PMTs. This level of background noise varies, in particular as a function of the sea currents and the temperature of the water. The higher the current, the greater the background noise (the opposite is not true). Fig. 1.19 (a) shows the background noise rate, or baseline, measured by different storeys of a line in a period of a few days, at around 60 kHz most of the time, while Fig. 1.19 (b) shows the background noise rate for a time interval of one hundred seconds. On this window, one can see, in addition to the baseline, peaks of a few seconds, which generally correspond to the passage of bioluminescent macroscopic organisms, and which are visible only on neighboring optical modules.

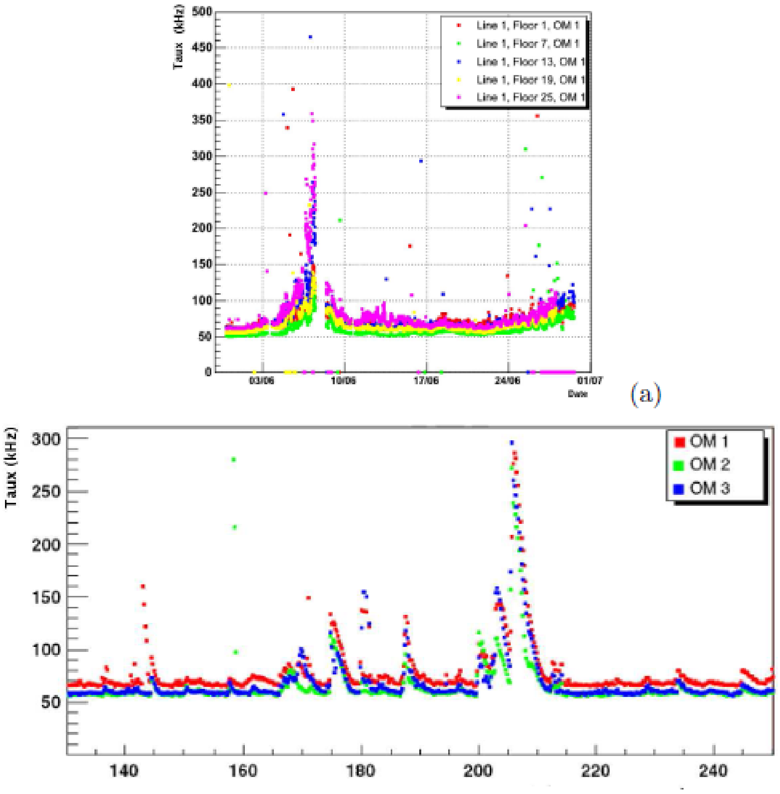

(a)

(b)

FIGURE 1.19: (a) Count rate of 5 optical modules of line 1 placed on 5 different stages for a period of about one month. (b) Count rate of three optical modules of the same floor (as a function of time (s)) for a period of one hundred seconds.

Finally, we can note the electronic background of photomultipliers which is of the order of 2-3 kHz [29].

1.6.2 Pointing accuracy

The expected performance of the detector is generally derived from simulated data. Angular resolution is a crucial characteristic of a telescope seeking to detect point sources. It is a function of reconstruction methods, which constantly evolve over time. For the ANTARES detector, this parameter is illustrated on Fig. 1.20. This figure shows the median value of the distribution between the angle of simulated neutrinos and reconstructed muons, as well as the median value of the distribution between the angle of simulated and reconstructed muons.

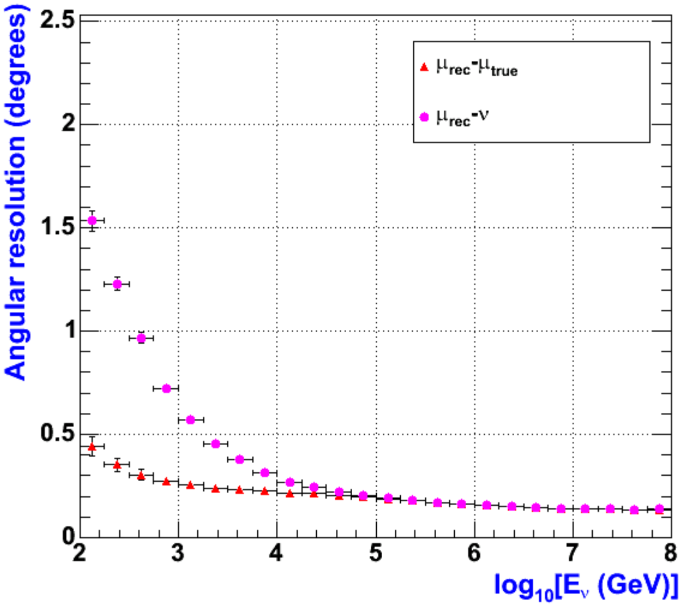

FIGURE 1.20: Distribution of the angular difference between the direction of the reconstructed muon and the direction of the incident muon (in red), or the direction of the incident neutrino (in pink).

One can see that at high energy, above 100 TeV, the muon resulting from the interaction of the neutrino, follows the same direction ($\leq 0.2°$), and the resolution of the detector is then limited only by the reconstruction quality. Whereas at low energy, the ANTARES resolution is mainly limited by the angle between the muon resulting from the interaction of the neutrino with the Earth, and the parent neutrino. The energy resolution of the detector and its effective surface are important parameters that also characterize a telescope.

1.6.3 Effective area

The effective area is the surface the detector would have perpendicular to the incident particle beam if its detection efficiency was 100%. It is obtained from the ratio of the rate of detected events (s^{-1}), muons in the following, over the incident flux ($cm^{-2} \cdot s^{-1}$). For an incident muon flux at the detector, this gives the muon effective area. For an incident flux of neutrinos at the Earth surface, this gives the neutrino effective area.

Muon effective area

The muon effective area gives the response function (detection rate) of the detector to an incident muon flux, whatever the process that gave rise to this flux. It is shown on Fig. 1.21 (obtained from simulated charged current neutrino interactions).

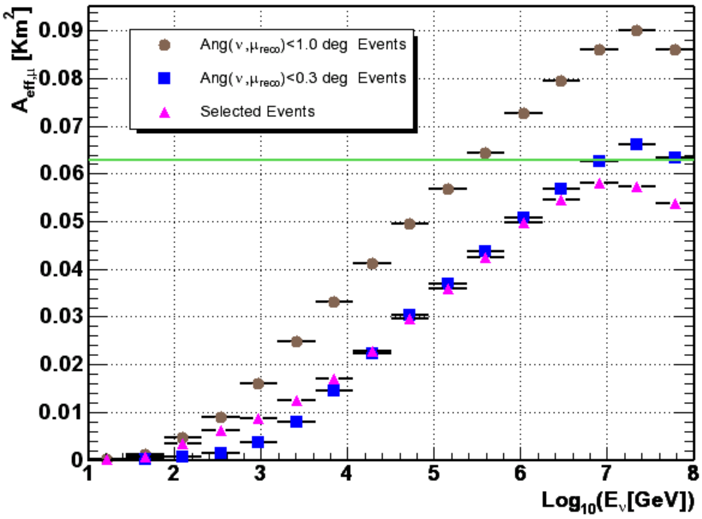

FIGURE 1.21: Muon effective area.

The two first curves are respectively for reconstructed muons matching the neutrino angle at less than 1 degree and less than 3 degrees. They were obtained requiring explicitly these angular resolutions. The last curve is the result of the selection criteria that lead to the angular resolution curve above, namely better than 0.3 degree above 10 TeV (thus explaining why the purple curve crosses the blue one at 10 TeV). Below 100 GeV muons do not cross the instrumented volume anymore. This explains the drop below this energy. The green line represents the geometrical surface, namely the ground surface covered by the instrumented volume. At high energies the effective area reaches or even exceeds the geometrical surface.

Neutrino effective area

The muon-neutrino effective area is much smaller than the muon effective area since it takes into account the probability for a muon neutrino to interact and give a muon that can be seen by the detector. It never exceeds a few tens of square metres. It is shown for several angle ranges on Fig. 1.22.

Around the vertical (0-30°, blue curve) and above 100 TeV, the Earth starts to become opaque to neutrinos : because of their larger cross section they interact early and the muon cannot reach the detector. At larger angles the rock thickness is smaller and this effect occurs later in energy. As a consequence the detector remains very efficient at very high energy for nearly horizontal neutrinos.

1.6.4 Detector response to various spectral indices

Fig. 1.23 shows the differential event rates as a function of the simulated neutrino energy for three incoming neutrino spectra. Each spectrum is a power law, normalised to the same value, with the spectral indices, $g = 2$, $g = 2.2$ and $g = 3.7$. The first two

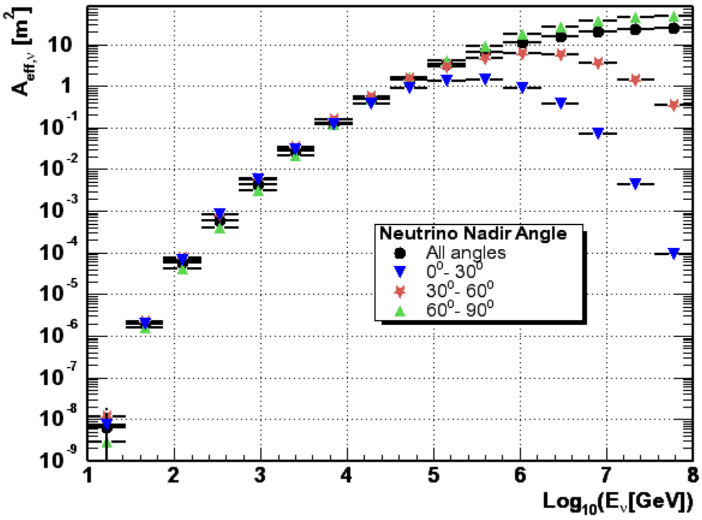

FIGURE 1.22: Neutrino effective area.

values are what is expected from cosmic accelerators, while the last one is a good approximation of an atmospheric neutrino spectrum.

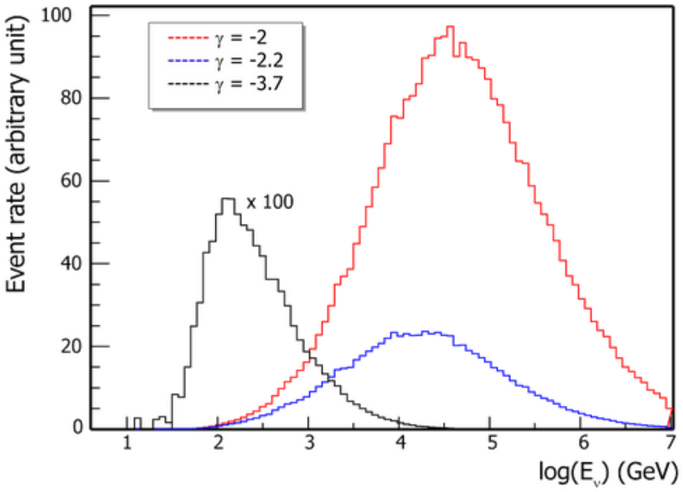

FIGURE 1.23: Event rates as a function of the simulated neutrino energy for three incoming neutrino spectra.

This figure was obtained from simulated charged current neutrino interactions. Muon were reconstructed and selected according to point-like source search criteria (purple curve in the angular resolution plot). It shows where the event rate peak is expected for each hypothesis and how the cosmic accelerator spectrum can be separated from the atmospheric neutrino events.

1.6.5 Energy response

The energy response is determined by the energy fraction transferred to the muon in the neutrino interaction, the energy lost by the muon outside the detector and the energy resolution of the detector. The muon energy determination requires different techniques in different energy ranges. Below 100 GeV, the muons are close to minimum-ionizing, and the energy of contained events, with start and end points measured inside the detector, can be determined accurately from the range. The threshold for this method is about 5-10 GeV for vertical tracks, depending on the vertical distance between groups of optical modules, and about 15 GeV for more isotropic events, depending on the horizontal distance between lines. Above 100 GeV, the range cannot be measured because of the limited size of the detector, but the visible range determines a minimum energy that can be used for the analysis of partially-contained events: starting events in which the vertex point is measured inside the detector, and stopping events in which the endpoint is measured. Above 1 TeV, stochastic processes (bremsstrahlung, pair production, δ-rays) are dominant, and the muon energy loss becomes proportional to the energy. The muon range above 1 TeV increases only logarithmically with the muon energy. On the other hand, the detection efficiency increases with energy because of the additional energy loss. Monte Carlo studies have shown that the neutrino energy can be determined within a factor 3 above 1 TeV from the average energy loss. Above 1 PeV, the Earth becomes opaque to upward-going vertical neutrinos. Higher energies are accessible closer to the horizon, however. Very high-energy tau neutrinos can be observed because the $\tau^{\pm}$ produced in ν_τ interactions decay before they are absorbed, producing ν_τ of lower energy which continue along the original ν_τ flight path, but with decreasing interaction probability, resulting in an accumulation of events at the highest detectable energies.

1.7 Triggers

The data filter algorithm applied onshore is based on different trigger criteria, including a general purpose muon trigger, a directional trigger, muon triggers based on local coincidences, a minimum bias trigger for monitoring the data quality, and dedicated triggers for multi-messenger investigations.

The general purpose (“standard”) muon trigger makes use of the general causality relation:

$$\mid t_i - t_j \mid \leq r_{ij} \times \frac{n}{c} \tag{1.9}$$

where t_i (t_j) refers to the time of hit i (j), r_{ij} to the distance between PMTs i and j, c is the speed of light and n the index of refraction of the sea water(Fig. 1.24, left). The direction of the muon, and hence of the neutrino, being not used, this trigger is sensitive to muons covering the full sky. To limit the rate of accidental correlations (i.e.to increase the purity of the event samples), the hits have to be preselected. This preselection provides the L1 signals, i.e.either coincidences in a time window of 20 ns between two neighbouring PMTs in the same storey or the occurrence of large pulses (number of photoelectrons typically greater than 3 in a single PMT). Then, the trigger criteria consist either in a set of at least 5 L1 hits that are causally related or in a local cluster of neighbouring L1 hits. The efficiency and the purity of this trigger have been determined with a simulation of the detector response to muons and accounting for the observed background [26]. The efficiency grows fast above 10 detected photons and reaches ≈ 1 at 40 detected photons. The typical threshold for the neutrino energy is a few hundred GeV.The purity is of the order of 90%, the remaining impurity being mainly due to (low energy) muons which in combination with the random background produce a trigger. The observed trigger rate is thus dominated by the background of atmospheric muons and amounts to 5–10

Hz(depending on the trigger conditions). The standard trigger can operate with hit rates in each PMT up to about 250kHz.

In addition to the standard trigger, a directional trigger has been implemented to maximize the detection efficiency of tracks coming from predefined directions. Currently, this trigger is used to look for events coming from the Galactic centre. This trigger makes use of the following direction specific causality relation:

$$(z_i - z_j) - R_{ij} \tan\theta_c \leq c(t_i - t_j) \leq (z_i - z_j) + R_{ij} \tan\theta_c \tag{1.10}$$

where z_i refers to the position of hit i along the neutrino direction, R_{ij} refers to distance between the positions of hits i and j in the plane perpendicular to the neutrino direction and θ_c is the Cherenkov angle in water(Fig. 1.24, right).

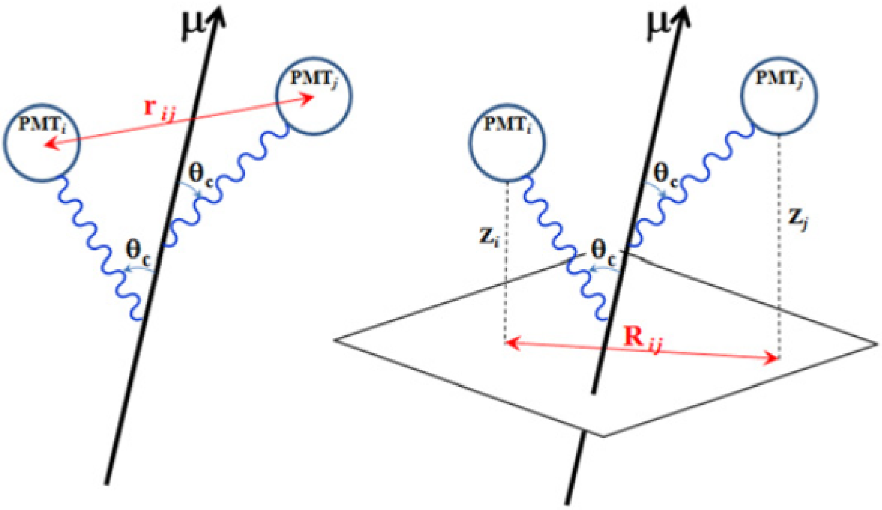

FIGURE 1.24: Definitions of the symbols used in Eq.(1.9) (left) and in Eq.(1.10) (right).

Compared to Eq.(1.9), this condition is more stringent because the 2-dimensional distance R_{ij} is always smaller than the corresponding 3-dimensional distance. Furthermore, this distance corresponds to the distance travelled by the photon (and not by the muon). Hence, it can be limited to several absorption lengths without loss of detection efficiency. This restriction reduces the combinatorics significantly. As a consequence, all hits can be considered for the directional trigger and not only the preselected hits used for the standard trigger, without compromising the purity of the physics events. In a field of view of about 101 around the selected direction and for neutrino energy below 1 TeV, the detection efficiency with the directional trigger is 2 times higher than that obtained with the standard trigger.

1.8 Conclusion

ANTARES has demonstrated that undersea neutrino telescopes are feasible and manageable from the onshore infrastructure. A neutrino telescope is potentially sensitive to any particle emitting light in its path and could detect the passage of still unknown particles, such as magnetic monopoles.

The prediction of such particles in physics and their theoretical framework will be discussed in the next chapter.

Chapter 2

Magnetic monopoles

2.1 Introduction

The concept of electric monopole is very familiar in physics although it is known with its more common name "electric charge", because it exists in the form of particles that have positive or negative charges like electrons and protons. Opposite electric charges attract and like charges repel through the interaction of electric fields, which are defined as running from positive to negative. Magnetism seems analogous to electricity, as there exist a magnetic field with a direction defined as running from north to south. However, this analogy breaks down when trying to find the magnetic counterpart of the electric charge, the magnetic monopole (MM). This particle with only one magnetic pole has never been observed, instead, magnets exist only in the form of dipoles with a north and a south end.

Therefore, from a theoretical point of view, magnetic monopoles would be expected to exist. Finding one would be an incredible breakthrough for high energy physics. They derive their properties from laws of physics at very high energies, which are far out of reach of any particle accelerator experiments. They are absolutely stable, so they would not decay to other particles, unlike most other particles physicists are hoping to find, and they interact relatively strongly through the electromagnetic field, which means that they would be easy to study experimentally. Their discovery would therefore allow physicists to design experiments to test GUTs (Grand Unified Theories) and TOEs (Theories Of Everything) directly. Unfortunately, all attempts to find them have failed so far, but they have still played a key role in the development of particle physics and cosmology in the recent decades.

2.2 Monopoles in Classical Electrodynamics

In classical electrodynamics, the fundamental quantities are the electric and magnetic fields, **E** and **B**. Electric charges both create and respond to electric fields, so that two charges interact because one charge responds to the field created by the other, and vice versa. Basically, all electromagnetic problems can be reduced to finding the electric and magnetic fields for given sources and boundary conditions. Even more fundamentally, all electromagnetic effects can be derived from a set of Maxwell equations. The following Maxwell equations for a vacuum without sources possess an interesting symmetry:

$$\nabla \cdot \mathbf{E} = 0, \tag{2.1}$$
$$\nabla \cdot \mathbf{B} = 0, \tag{2.2}$$
$$\nabla \times \mathbf{E} + \frac{1}{c}\frac{\partial \mathbf{B}}{\partial t} = 0, \tag{2.3}$$
$$\nabla \times \mathbf{B} - \frac{1}{c}\frac{\partial \mathbf{E}}{\partial t} = 0. \tag{2.4}$$

Anyone staring at the above equations can see that they are symmetric under the exchange of **E** and **B**. More precisely, they are invariant under

$$\mathbf{E} \to \mathbf{B} \qquad \text{and} \qquad \mathbf{B} \to -\mathbf{E} \tag{2.5}$$

Unfortunately, the above symmetry seems to be spoiled in nature since no magnetic charges have been observed so far. To understand the statement, assume that there are electric charge density ρ_e and electric current J_e but no corresponding magnetic conterparts. The Maxwell equations then become :

$$\nabla \cdot \mathbf{E} = 4\pi\rho_e, \tag{2.6}$$
$$\nabla \cdot \mathbf{B} = 0, \tag{2.7}$$
$$\nabla \times \mathbf{E} + \frac{1}{c}\frac{\partial \mathbf{B}}{\partial t} = 0, \tag{2.8}$$
$$\nabla \times \mathbf{B} - \frac{1}{c}\frac{\partial \mathbf{E}}{\partial t} = \frac{4\pi}{c}J_e. \tag{2.9}$$

The equations are no longer symmetric under the duality transformation. Equations (2.7) and (2.8) seem to be missing something on their right hand sides. To see exactly what they are missing, it is needed to explain the meaning of $\nabla \cdot B$, also called the divergence of B. Let V be a volume enclosed by a surface S in space. $\nabla \cdot B$ integrated over the volume V gives 4π times the total amount of magnetic charge g contained in V. Similarly, $\nabla \cdot B$ evaluated at point x gives 4π times the magnetic charge density at x. Hence, Equation (2.7) says that there is no magnetic charge at any point in space. Roughly speaking, moving charges are equivalent to currents. But because the above Maxwell equations assume that there is no magnetic charge, there is no magnetic current J_m on the right hand side of Equation (2.8). Hence, the absence of magnetic charge ruins the duality. In other words, the absence of magnetic charge breaks the symmetry.

This raises the question why nature has this asymmetry. From the point of view of classical electrodynamics, there is no reason why there could not be magnetic charges, and if they did, the duality symmetry would be intact. In other words, classical electrodynamics is perfectly compatible with the notion of magnetic monopoles, and from the aesthetic point of view it is strange that magnetic monopoles do not seem to exist, because their existence would make the theory more symmetric [46].

2.3 The Dirac monopole

The concept of a particle with a magnetic charge (the magnetic monopole) was first introduced by P. A. M. Dirac in 1931 [47] to explain the quantization of the elementary electric charge, e. Measured electric charges are always found to be integer multiples of the electron charge. This quantization of electric charge is a deep property of Nature without an explanation. Dirac showed that assuming the existence of a particle with a single magnetic pole, and that it can interact with charged particles, then the laws of quantum mechanics impose that electrical charges must be quantized.

Consider a magnetic field produced by a magnetic monopole of charge g, like the Coulomb electric field produced by an electric charge:

$$\vec{B} = \frac{g\vec{r}}{r^3}. \tag{2.10}$$

A particle with an electric charge e interacting with a magnetic monopole satisfies the classical equations of motion:

$$m\ddot{\vec{r}} = e\dot{\vec{r}} \wedge \vec{B}. \tag{2.11}$$

The classical dynamic defined by this equation is perfectly known. However, to characterize the quantum mechanics of a charged particle interacting with a magnetic monopoles, it is needed to introduce the potential vector $\vec{A}$ such as $\vec{B} = \vec{\nabla} \wedge \vec{A}$.

To define the quantum mechanisms, the action S_{int} is introduced, the interaction term of a charged particle with an external electromagnetic field

$$S_{int} = \frac{e}{\hbar c}\int_1^2 dt\frac{d\vec{r}}{dt}\cdot\vec{A} = \frac{e}{\hbar c}\int_1^2 d\vec{r}\cdot\vec{A}, \tag{2.12}$$

which depends only on the path traversed by the particle. The wave function of the particle can be then represented by

$$\psi(\vec{r}) = \psi_0(\vec{r})e^{i\frac{e}{\hbar c}\int_0^{\vec{r}} d\vec{r'}\cdot\vec{A}}, \tag{2.13}$$

where $\psi_0(\vec{r})$ is a wave function satisfying the free Schrödinger equation. The potential vector $\vec{A}$ can not be defined continuously on a sphere surrounding a magnetic monopole. However, this definition does not matter, in fact only the relative phase between two paths will interest us.

Consider Γ and Γ' two different paths with the same starting and ending points.

$$(S_{int})_\Gamma - (S_{int})_{\Gamma'} = \frac{e}{\hbar c}\oint_{\Gamma-\Gamma'} d\vec{r}\cdot\vec{A} = \frac{e}{\hbar c}\int_{S_{\Gamma-\Gamma'}} d^2\vec{S}\cdot\vec{B} = \frac{e}{\hbar c}\Phi_{\Gamma-\Gamma'}. \tag{2.14}$$

By applying the Stokes theorem, the relative phase $\Phi_{\Gamma-\Gamma'}$ has been expressed as the magnetic flow through a surface bounded by the closed path $\Gamma - \Gamma'$. The relative phase is thus a function of the magnetic field which is better defined. There is, however, always a problem because the phase is multivalued. If the path Γ' can scan once the surface closed around the monopole and return to its original position, then the action changes of

$$\Delta S_{int} = \frac{e}{\hbar c}\Phi_{sphere} = \frac{e}{\hbar c}\frac{g}{r^2}\int_0^{\pi} \sin\theta d\theta \int_0^{2\pi} d\phi = \frac{4\pi e g}{\hbar c}, \tag{2.15}$$

where θ and ϕ are the zenithal and azimuthal angle in spherical coordinates respectively.

Finally, the relative phase between two paths is defined unambiguously, only if $exp(i\Delta S_{int}) = 1$, and so if

$$\frac{eg}{c} = \frac{n\hbar}{2} \quad \longrightarrow \quad g = k \cdot g_D = k \cdot \frac{e}{2\alpha}\,, \tag{2.16}$$

with $n \in Z$. This simple relation is the quantization condition of Dirac. If a monopole is somewhere in the Universe, it would explain the quantization of electrical charges.

2.4 Monopoles and unification

In contrast to Dirac's demonstration of the consistency of magnetic monopoles with quantum mechanics, G. 't Hooft [4] and A. M. Polyakov [5] demonstrated independently in 1974 the necessity of magnetic monopoles in unified gauge theories. Any unified gauge theory in which the group $U(1)$ describing electromagnetism is embedded in a spontaneously broken semisimple gauge group, and electric charge is thus automatically quantized, necessarily contains magnetic monopoles. MMs appear at the phase transition corresponding to the spontaneous breaking of the unified group into subgroups, one of which is $U(1)$, describing electromagnetism [54].

Grand unified theories (GUTs) are based on the hypothesis that at sufficiently high energies, strong, weak and electromagnetic interactions come from a single gauge group, within which they were unified, which was broken into $SU(3) \times SU(2) \times U(1)$. This group represents the standard model of particle physics: the group $SU(3)$ describes the strong interaction, and the group $SU(2) \times U(1)$ describes the electroweak interaction. Therefore, the existence of magnetic monopoles is a generic prediction of grand unification.

2.5 Monopoles in the Universe

At the beginning of the Universe where the temperature was very high, forces were unified. With the expansion of the universe and the decrease of its temperature, and at a certain temperature of order Λ, these gauge symmetries have been spontaneously broken in the framework of the so-called phase transitions of the universe. At this stage, topological defects including magnetic monopoles have been created according to the Kibble mechanism [49]. One magnetic monopole is created per causal domain at this time, with a typical mass of 10^{17}GeV. Regarding the magnetic monopole relic, there is an inconsistency referred to as the "magnetic monopole problem". Their mass density exceeds the mass density of the observable Universe by many orders of magnitude [50], which means that the density of magnetic monopoles should be higher than observed. This problem can be solved assuming an inflation phase that occurred at the early universe, which dilutes the magnetic monopole density to a very small number [1] (see Fig. 2.1).

Inflation models can solve this problem by reducing the abundance of monopoles in the observable universe at negligible values [52].

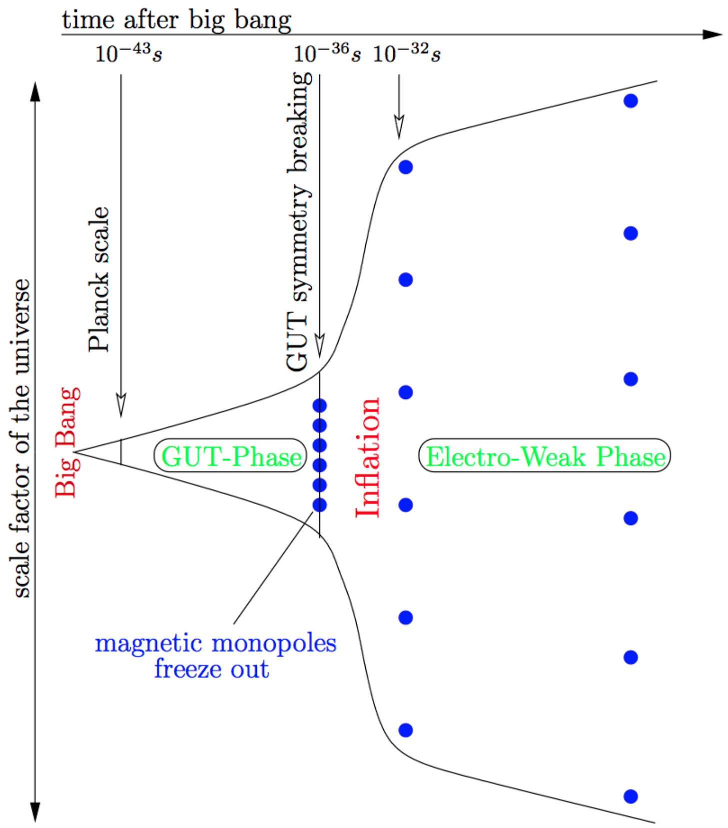

FIGURE 2.1: Illustration of the time evolution in the early Universe. If monopoles are created before the symmetry breaking, their density is diluted by inflation. Taken from [51].

Another solution is based on grand unification models in which magnetic monopoles appear at temperatures below 10^{11} GeV, well below the initial high unification scale [53]. This leads to intermediate monopole masses, and to a more reasonable density compared to cosmology.

The mass (and charge) of magnetic monopoles is highly dependent on the scale of unification of the gauge theories that predict them.

$$M \geq \frac{\Lambda}{\alpha_G}, \tag{2.17}$$

where α_G is the unified gauge coupling constant. As determined from the running of the low-energy coupling constants, Λ and α_G are expected to be of the order of 10^{15} GeV and 10^{-2} respectively [54].

In a minimal $SU(5)$ unification model, the magnetic monopoles produced are of mass of the order of 10^{17} GeV, carrying a single Dirac charge [55, 56]. However, an extension of the $SU(5)$ model predicts a magnetic monopole mass of the order of 10^{11} GeV [57], and the phenomenologically interesting model $SU(15)$ gives relatively light particles of $\approx 10^{8}$ GeV [58, 59]. In some supersymmetric models, magnetic monopole masses as low as 10^{7} GeV appear in [60, 61]. One can also distinguish Kaluza-Klein models [62, 63], which reduce the mass of large unification if the extra-dimensions are not too compactive. For example, with the introduction of two extra-dimensions of millimeter size, the unification scale becomes of the order of 100 TeV, implying a mass of the order of 10^4 TeV for the magnetic monopoles.

There are many theoretical possibilities to produce magnetic monopoles, with masses ranging from about 10^4 GeV to about 10^{20} GeV, and multiple charges. The Kibble mechanism predicts a significant flux of magnetic monopoles on Earth if their formation has not been followed by a period of inflation.

2.6 Acceleration of cosmic monopoles

A broad motivation for the search for magnetic monopoles in high-energy cosmic rays is the ease with which kinetic energy is transmitted to magnetic monopoles by cosmic magnetic fields. A magnetic field B acting over a length l increases the monopole kinetic energy T by

$$T = gBl. \tag{2.18}$$

For a fine structure constant of $1/137$, one can calculate the energy gBl that a magnetic monopole of minimal charge would acquire across various regions of magnetic fields in the Universe. These energies can be computed from the properties shown in Table 2.1, taken from [64], from various estimated characteristics of cosmic magnetic fields that can be traversed by magnetic monopoles.

cosmic environment	$B(\mu G)$	$L(pc)$	$T(GeV)$
Milky Way	3	300	6×10^{10}
galaxy clusters	$2-30$	$10^2 - 10^6$	$10^{10} - 10^{15}$
extragalactic sheets	$0.1-1$	$10^6 - 3 \times 10^7$	$10^{12} - 10^{15}$
AGN jets	10^2	$10^2 - 10^4$	$10^{11} - 10^{13}$
radio galaxy lobes	$10 - 10^2$	10^5	$10^{13} - 10^{14}$

TABLE 2.1: Magnetic field strength B and coherence length L of several cosmic magnetic fields, taken from [52, 65, 66]. The typical kinetic energy T of a magnetic monopole that traverses such a field is given in the last column.

The extragalactic medium is expected to be the dominant spectrum of the medium that can be crossed by magnetic monopoles. Based on the values in the table, a minimum energy gain of 1.7×10^{13} GeV is expected for a minimum magnetic monopole charge and $\alpha \approx 1/137$, after it has passed through a coherent extragalactic magnetic field region. Thus, in order for a magnetic charge to reach a speed of $\beta \geq 0.5$ and thus to emit a sufficiently characteristic signal in water, it is necessary that $M \leq 1.5 \times 10^{13}$ GeV. However this calculation only takes into account the passage of a magnetic monopole in a single region of coherent field. In the paper [64], the number of crossed fields is estimated to be of the order of $n \approx H_0^{-1}/50Mpc \approx 100$, inducing an acquired energy of a higher order of magnitude, and thus a limit mass for relativistic monopoles of the order of $M \leq 10^{14}$ GeV.

Parker was one of the first to emphasize that the existence of observable galactic magnetic fields could provide an upper limit on the magnetic monopole flux [69].

Magnetic monopoles propagating in the Universe will be accelerated by the magnetic field, and will therefore gain kinetic energy to the detriment of the latter. In order for the magnetic field to survive, the rate at which the field energy is drained must be small compared of the time scale of its regeneration. With reasonable choices for the astrophysical parameters [70], the Parker bound corresponds to

$$\Phi_M \lesssim \begin{cases} 10^{-15} & [\mathrm{cm}^{-2}\mathrm{s}^{-1}\mathrm{sr}^{-1}], \quad M \lesssim 10^{17}\ \mathrm{GeV/c}^2 \\ 10^{-15}\left(\frac{10^{17}\ \mathrm{GeV}}{M}\right) & [\mathrm{cm}^{-2}\mathrm{s}^{-1}\mathrm{sr}^{-1}], \quad M \gtrsim 10^{17}\ \mathrm{GeV/c}^2 \end{cases} \tag{2.19}$$

The Parker bound is also shown in Fig. 2.2. For larger monopole masses and velocities, the limit is less stringent.

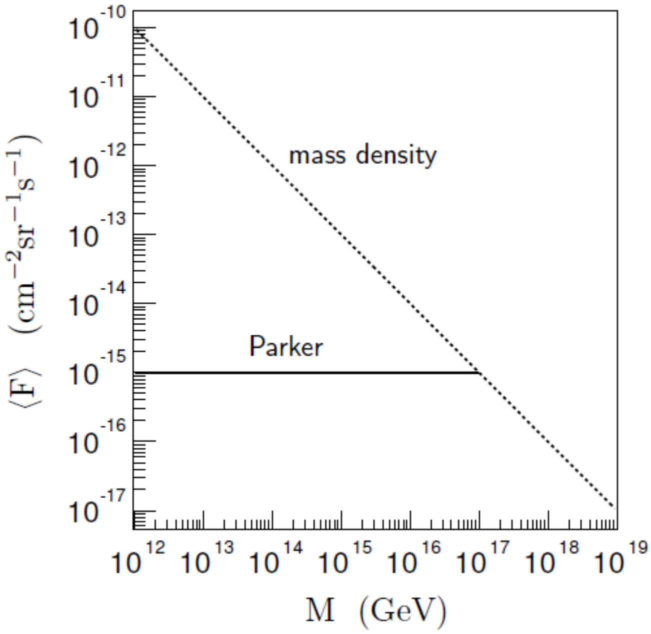

FIGURE 2.2: Upper limits on the average monopole flux as a function of the monopole mass for a typical monopole velocity of $10^{-3}c$. The limits are based on the mass density of the Universe (dashed line) and the survival of the galactic magnetic field (i.e. the Parker bound, solid line).

2.7 Experimental searches

Search strategies are determined by the expected interactions of MMs as they pass through matter. These would give rise to a number of peculiar signatures. A complete description of the techniques used for the search of these particles is in [71], and a complete list of the results in [70].

Many searches for cosmic monopoles have been performed since the theoretical prediction of their existence, using different techniques. The MACRO experiment applied different types of excitation and ionisation detectors (liquid scintillators, streamer chambers and nuclear track-etch material) to search for monopoles in a large velocity range, $\beta \geq 4 \times 10^{-5}$, with a detection area of several 100 m^2 [72], and obtained the limit on the magnetic monopole flux, carrying a Dirac charge, the most extended according to their speed. This 90% confidence limit is about one order of magnitude greater than Parker's limit. Another experiment based on the ionisation properties of monopoles is the Ohya experiment, which has used a 2000 m^2 array of track-etch detector to search for supermassive relic particles in the same velocity range as MACRO [73]. The bright Cherenkov signal of a monopole in water and ice is used by the Baikal and AMANDA neutrino telescopes to search for fast monopoles with $\beta \geq 0.8$ [6, 74]. Other experiments have been searching for the catalysis of proton decay, see e.g. [75, 76].

Analogs of monopoles may be observable in quantum fluids. M. W. Ray et al. [77] performed an experiment in which they manipulated a gas of rubidium atoms prepared in a non-magnetic state close to absolute zero temperature. Under these extreme conditions, they were able to create a monopole in the quantum-mechanical field that describes the gas. This experiment established important characteristics of magnetic monopoles, supporting the possibility of their existence.

Guided mainly by Dirac's argument and their predicted existence from spontaneous symmetry breaking mechanisms, searches have been routinely made for MMs produced at accelerators, in cosmic rays, and bound in matter [70, 71]. Eq.(2.16) defines most of the MM properties, as they are assumed as point-like particles, of magnetic charge equal g, with unknown mass and with unknown relic cosmic abundance. To date, there are no confirmed observations of exotic particles possessing magnetic charge.

MMs at the electroweak scale with $M < 10$ TeV are very good candidates for searches at the CERN's Large Hadron Collider (LHC). The ATLAS collaboration [7] searched for MMs as highly ionizing particles produced in proton-proton collisions, leading to new cross section upper limits for spin 1/2 and spin 0 particles. MoEDAL is a dedicated experiment searching for MMs produced in high-energy collisions at the LHC using stacks of nuclear-track detectors and a trapping detector. Recently, limits on MM production cross sections have been reported both for 8 TeV and 13 TeV LHC runs [78, 79].

Several searches were carried out also using neutrino telescopes. The ANTARES neutrino telescope [13] was completed in 2008 and the collected data can be used to search for MMs with energies high enough to yield light emission. The results of the analysis published in [8] using a data set of 116 days livetime, lead to upper limits on the flux in the range between 1.3×10^{-17} and 5.7×10^{-16} $\mathrm{cm^{-2} \cdot s^{-1} \cdot sr^{-1}}$ for MMs with $\beta > 0.6$. The IceCube collaboration has set upper limits on the flux for relativistic MMs ranging from 1.55×10^{-18} to 10.39×10^{-18} $\mathrm{cm^{-2} \cdot s^{-1} \cdot sr^{-1}}$ [9] (see Fig. 2.3).

2.8 Conclusion

Despite intense research, magnetic monopoles have not been observed so far, and are not part of the standard model theory. But several theories of grand unification foresee the existence of monopoles or at least the possibility of their existence at high energy. Their discovery would have important consequences, as it would naturally complete the theory of electromagnetism by making Maxwell's equations

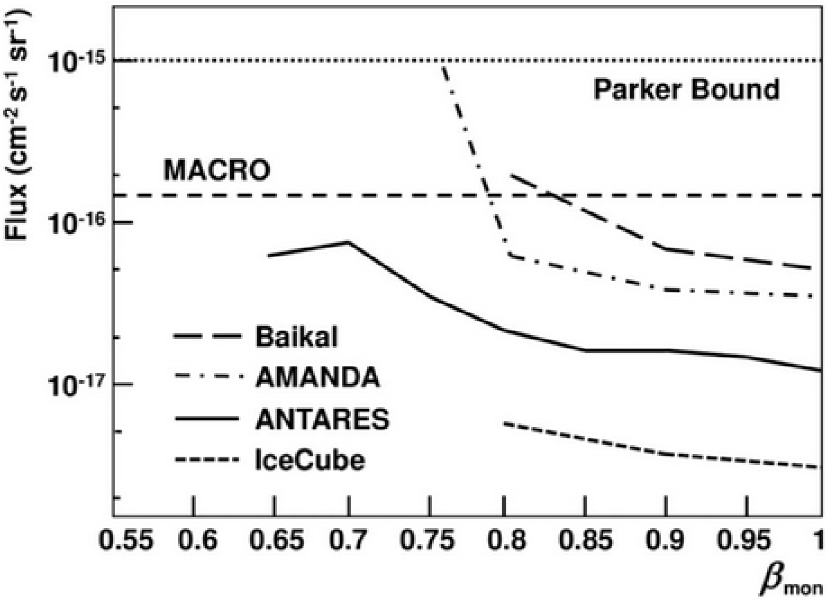

FIGURE 2.3: Upper limits on the monopole flux as a function of $\beta = v/c$, obtained by different experiments (taken from [80]).

completely symmetrical under the electrical-magnetic duality and secondly it would give a natural explanation to the quantization of the electric charge.

Chapter 3

Magnetic monopole interaction with matter and detection with a neutrino telescope

3.1 Introduction

At high speeds, a magnetic monopole carrying Dirac charge, should behave like a heavy ion $Ze \approx 68.5e$ (considering a fine structure constant of $\approx 1/137$). Due to this relatively large charge, large electromagnetic energy losses are expected when crossing the material. In its motion, the magnetic monopole produces an electric field that is perpendicular to its direction of propagation, which interacts with the electrons of the atoms, and the nuclei of the medium traversed. This electric field will thus lead to the ionization and excitation of the surrounding atoms.

The ANTARES telescope is essentially sensitive to upward going particles. Therefore, it is necessary to estimate the energy that a magnetic monopole would lose when crossing the Earth, to know if it is possible to look for them as up-going events.

3.2 Energy loss and interactions of monopoles

The energy loss of monopoles in matter due to electronic interactions refers to ionization and atomic excitation of the medium. As mentioned before, at high velocities, the electromagnetic interaction of magnetic monopoles is comparable to the interactions of heavy ions of charge $Z \approx 68$.

3.2.1 Collisional losses

S. P. Ahlen [81] has established for magnetic monopoles the equivalent of the Bethe-Bloch formula that describes the energy loss in the passage of a heavy electric charge by ionization and excitation in a non-conductive medium, based on the Mott cross sections by Bauer and Cole [82, 83]. Then, he calculated the energy loss [84] after the publication of the new KYG cross section [85]

$$\frac{dE}{dx} = \frac{4\pi N_e g^2 e^2}{m_e c^2}[ln(\frac{2m_e c^2 \beta^2 \gamma^2}{I}) - \frac{1}{2} + \frac{k}{2} - \frac{\delta}{2} - B_m], \tag{3.1}$$

where N_e is the electron density, m_e is the electron mass, g is the magnetic charge of the monopole, I is the mean ionization potential, δ is the density effect correction [86], k is the QED correction of cross section [85], and B_m is the Bloch correction [87]. The formula is valid in the velocity range $\beta \geq 0.1$ and $\gamma \leq 100$ and it is plotted in Fig. 3.1. The monopole energy loss is constantly increasing with velocity whereas the energy loss of leptons is decreasing up to $\beta\gamma = 3.5$ before increasing again.

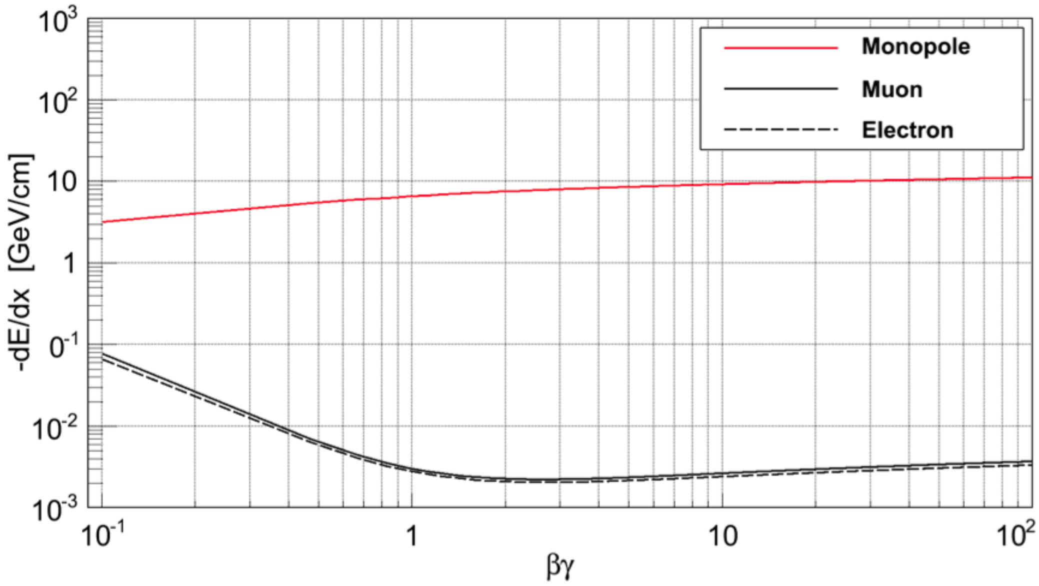

FIGURE 3.1: Mean energy loss rate due to collisional losses for monopoles, muons and electrons. Taken from [88].

The ionization energy loss of a monopole with magnetic charge g and velocity βc is about $(g\beta/Ze)^2$ times larger than that of a particle with electric charge Ze and the same velocity.

3.2.2 Radiative losses

At velocities $\gamma > 10^3 (\beta \approx 0.999)$ radiative processes have to be considered. These are pair production, bremsstrahlung, and photo-nuclear interactions.

Electromagnetic energy loss by a magnetic monopole of a mass $M \sim 10^5$ GeV in air is shown in Fig. 3.2 taken from [89]. The losses by collisions are dominant until $\gamma \sim 10^4$. At higher velocities, electromagnetic energy losses are dominated by pair production e^+e^- for $10^4 < \gamma < 10^6$, and by photonuclear interactions for $\gamma > 10^6$. In [89], the energy loss of muons by pair production [90, 91] is adapted to monopoles and photonuclear interactions are described by the exchange of a virtual photon between the monopole and the nucleus, such as the energy losses of leptons issued from these interactions [92] are adapted for monopoles. Fig. 3.2 also shows the contribution of energy losses by Bremsstrahlung radiation from magnetic monopoles, which become negligible for massive particles, because it's inversely proportional to their mass [89], whereas losses by collision, by pair production, and by photonuclear interactions are almost independent of the mass of the monopoles.

Furthermore, the stopping-power of a MM crossing the Earth could be estimated using the simplified density profile established by Derkaoui et al. [93] (see Fig. 3.3).

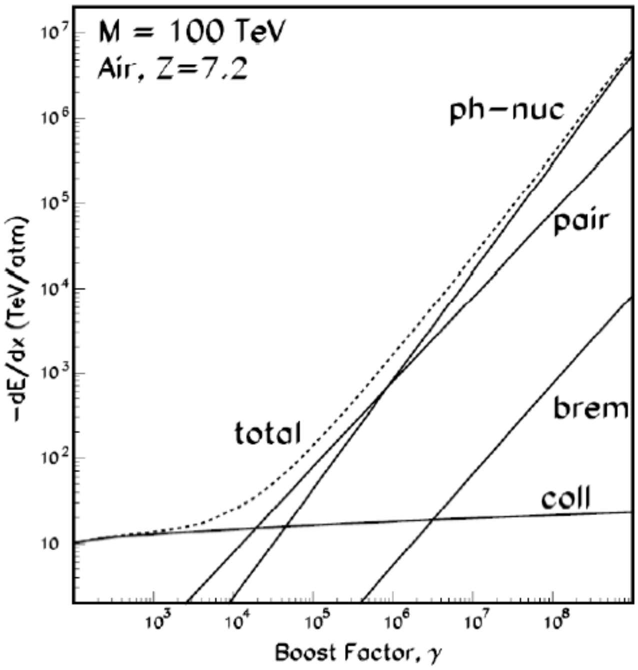

FIGURE 3.2: Electromagnetic energy loss by collision (coll), Bremsstrahlung (brem), pair production (pair), and by photonuclear interactions in air for a monopole of mass $M = 100$ TeV, as a function of the boost factor γ.

The solid lines of regions A and B are issued from Eq.(3.1) and another equation valid at mean velocities $10^{-3} < \beta < 10^{-2}$. Part C is the result of numerical calculations [93]. The dashed lines indicate that the formulas have been extrapolated beyond their area of validity ($\beta < 10^{-5}$ and $\beta \sim 8 \cdot 10^{-4}$), or that two valid regions have been connected with a polynomial ensuring continuity of functions and derivatives ($0.01 < \beta < 0.1$). On one hand, magnetic monopoles with $M \gtrsim 10^{10}$ GeV$/c^2$ would remain relativistic and detectable as up-going events (see for instance Fig. 3 of [71]) in spite of the energy loss in their path. On the other hand, magnetic monopoles with a mass $M \lesssim 10^{14}$ GeV$/c^2$ can be expected in neutrino telescopes as an up-going event with a speed exceeding the Cherenkov threshold, given reasonable astrophysical considerations.

3.2.3 Mechanism of Callan-Rubakov

Magnetic monopoles of some GUT models would catalyze nuclear decay [94–97]. This requires a low velocity of monopoles of about $\beta \leq 10^{-3}$. The cross section of catalysis takes the from:

$$\sigma_{cat} = \frac{\sigma_0}{\beta}, \tag{3.2}$$

where σ_0 has the value of strong interaction cross sections ($\sim 10^{-28} cm^2$). During a catalysis, the released energy is distributed between the different products of the proton decay, which will emit Cherenkov light. If the rate of nuclear decay is fairly high along the monopole path, the Cherenkov photon rate may exceed that of background. However, in the rest of the thesis we will focus only on the detection of magnetic monopoles by their direct and indirect Cherenkov emission.

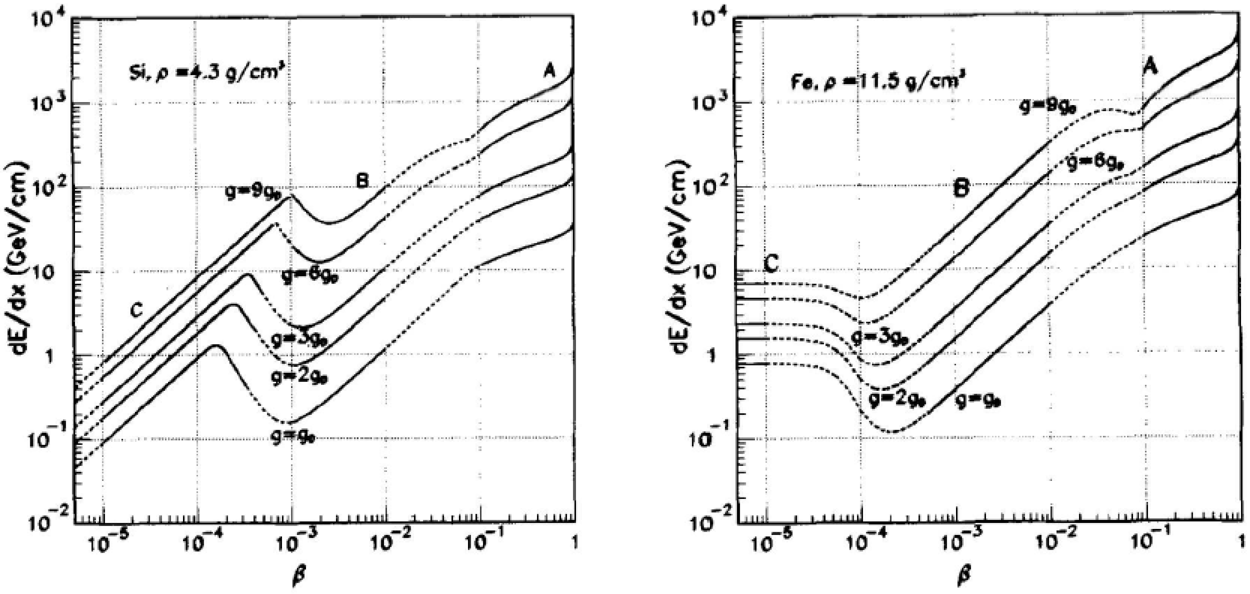

FIGURE 3.3: Energy loss of a monopole by ionization in the mantle (left) and the core (right) of the Earth, taken from [93].

3.3 Monopole signature in water

Despite high energy losses during a material traverse, a sufficiently energetic magnetic monopole (with a high mass and a large Lorentz factor) can cross the Earth and reach the detector with a significant upward speed. The speed of magnetic monopoles is the parameter which determines the mechanism of its detection. Given the extreme energies that can be achieved by monopoles by acceleration in a cosmological magnetic field and predicted masses according to the different models, it appears that the relatively light magnetic monopoles ($M \leq 10^{12}$ GeV) can easily reach relativistic speeds.

Based on this, the search for magnetic monopoles in ANTARES relies on two mechanisms:

- Direct Cherenkov emission ($\beta \geq 0.74$)
- Indirect Cherenkov emission ($0.52 \leq \beta < 0.74$).

3.3.1 Direct Cherenkov radiation

As for electrical charges, Tompkins [98] showed that for magnetic charges, the Cherenkov emission does not occur for a velocity $\beta < 1/n$, with n the refractive index of the medium. The number of photons emitted per unit length and wavelength, for $\beta > 1/n$ is written as:

$$\frac{d^2 n_\gamma}{d\lambda dx} = \frac{2\pi\alpha}{\lambda^2}\left(\frac{ng}{e}\right)^2\left(1 - \frac{1}{n^2\beta^2}\right), \tag{3.3}$$

where n_γ is the number of photons emitted and λ is their wavelength; the remaining quantities are already defined in Eq. (2.16). For a given speed, the Cherenkov radiation emitted by the magnetic monopole is a factor $\left(\frac{ng}{Ze}\right)^2$ more important than for an electrically charged particle. In addition to a different intensity of Cherenkov radiation, the radiation is polarized differently for a magnetic monopole than for an electric charge. Thus, for a refractive index $n \approx 1.35$ for seawater, and a fine structure constant $\alpha \approx 1/137$, about 8550 times more Cherenkov photons are expected to be emitted by a Dirac charge monopole $g = g_D$ than by an electric charge of the same speed.

3.3.2 Indirect Cherenkov radiation: δ-rays

During its passage through matter, a magnetic monopole will ionize the surrounding environment. This ionization will lead to the production of δ-electrons (or δ-rays), which will potentially emit Cherenkov light if their kinetic energy is sufficient. The electromagnetic interactions of a magnetic monopole in matter can be approximated to those produced by an electric charge by the $Z \to g\beta/e$ substitution [99]. Thus the distribution of δ-rays produced by a magnetic monopole can be deduced from those produced by an electric charge [100]. The contributions to the light yield from all mechanisms are shown in Fig. 3.4. The production of δ-electrons is described by the differential cross-section of Kasama, Yang and Goldhaber (KYG) [85] or by the more conservative (in terms of photon yield) Mott cross section [81].

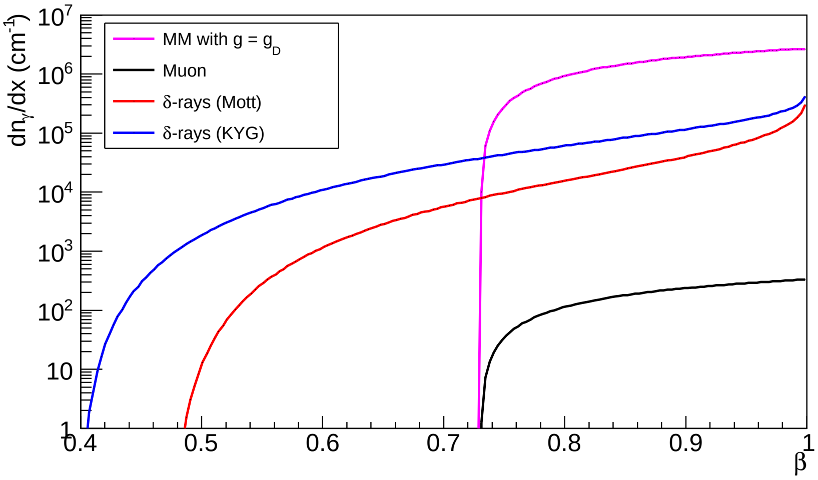

FIGURE 3.4: The total number of Cherenkov photons with wavelengths between 300 and 600 nm that are directly produced per centimeter path length by a MM with $g = g_D$, as a function of its velocity (β). The number of photons produced by δ-rays with Mott cross section model [81] and KYG cross section model [85] and by a minimum ionizing muon are also shown.

Contributions from radio-luminescence of water, pair production, Bremsstrahlung and photo-nuclear reactions induced by relativistic MMs are negligible compared to the direct and indirect Cherenkov light presented in Fig. 3.4, and are not taken into account in this analysis.

Production of δ-rays

The distribution of δ-rays produced by a magnetic monopole per unit of length dx and energy dT_e is given by [101]

$$\frac{d^2N_e}{dT_e dx} = \frac{2\pi N g^2 e^2}{m_e c^2} \frac{F(T_e)}{T_e^2}, \tag{3.4}$$

where T_e is the kinetic energy of the electrons. In order to emit Cherenkov light in a medium of index 1.35, an electron must have an energy of at least T_0 = 0.25 MeV. As $I = 74$ eV for water [102], Eq.(3.4) can be used to determine the number of δ-electrons producing Cherenkov light.

The factor $F(T_e)$ is dependent on the spin of the monopole. However, as long as T_e is small compared to the kinetic energy and mass of the monopole, the production of δ-ray is independent of its spin, and $F(T_e)$ is expressed as [101]

$$F(T_e) = (1 - \beta^2 \frac{T_e}{T_m}), \tag{3.5}$$

where T_m is the classical upper limit on the energy that can be transferred to an atomic electron in a single collision with a monopole. As the mass of the monopole is predicted to be much larger than the electron mass, the maximum energy transfer can be approximated by

$$T_m = 2m_e c^2 \beta^2 \gamma^2, \tag{3.6}$$

However, the maximum energy that can be transferred to an electron in a collision with a magnetic monopole is written as

$$T_{max} \approx 0.69 \cdot T_m, \tag{3.7}$$

The factor 0.69 takes into account the correction of the impact parameter [81]. Thus T_{max} should be used in Eq. (3.5) instead of T_m. The distribution of δ-rays produced by a monopole then becomes

$$\frac{d^2N_e}{dT_e dx} = \frac{2\pi N g^2 e^2}{m_e c^2} (\frac{1}{T_e^2} - \frac{\beta^2}{T_e T_{max}}), \tag{3.8}$$

The distribution of δ-rays that are produced with kinetic energies of at least T_0 by a monopole with g_D in water is shown in Fig. 3.5 for different monopole velocities.

Fig. 3.6 shows the number of δ-electrons, with a kinetic energy greater than $T_0 =$ 0.25 MeV, produced per centimeter as a function of the magnetic monopole velocity.

It is determined by integrating Eq. (3.8) between T_0 and T_{max}.

Cherenkov light emission by δ-rays

The number of Cherenkov photons, having a wavelength between 300 and 600 nm, emitted per unit length by an electron is written as

$$\frac{dN_\gamma}{dx_e} \approx 764(1 - \frac{1}{\beta_e^2 n^2})cm^{-1}), \tag{3.9}$$

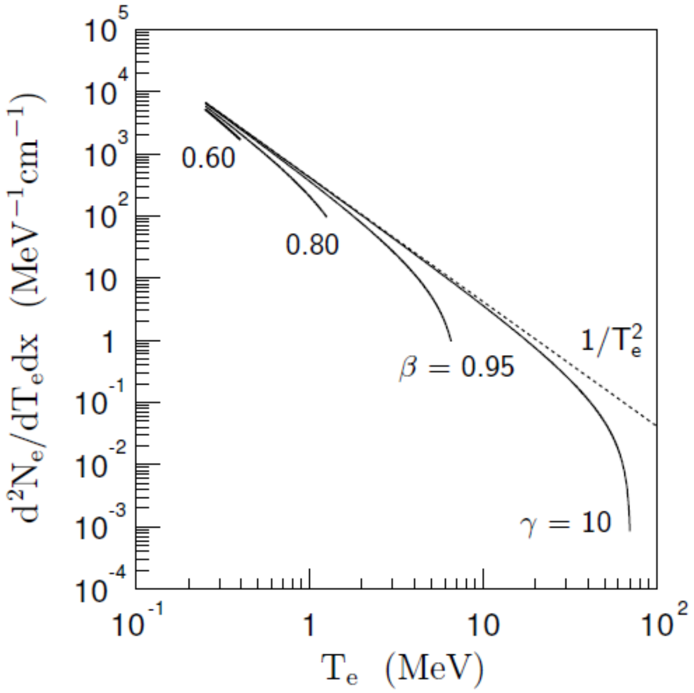

FIGURE 3.5: The distribution of δ-rays with kinetic energies above 0.25 MeV produced by a monopole with one Dirac charge g_D passing through water. The distribution is shown for monopole velocities β c = 0.60 c, 0.80 c, 0.95 c and γ = 10. The dashed line indicates a spectrum that is proportional to $1/T_e^2$.

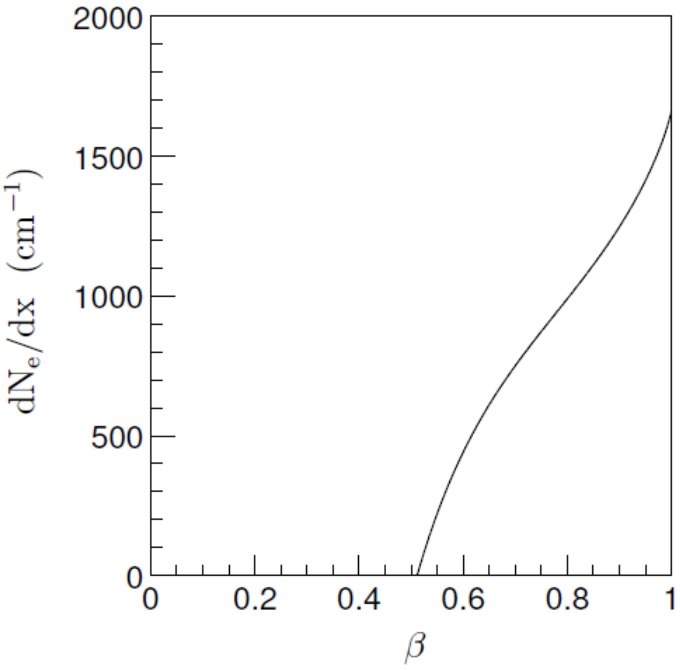

FIGURE 3.6: The total number of δ-rays with kinetic energies above 0.25 MeV produced per centimetre path length by a monopole with g_D, as a function of the monopole velocity. The assumed medium corresponds to sea water.

where $\beta_e c$ is the velocity of the δ-ray. Before calculating the total number of Cherenkov photons N_γ emitted by a δ-electron with an initial kinetic energy T_e, it is necessary to know the losses of energies by ionization of an electron in water. They can be calculated via the Seltzer and Berger formula [103], valid for kinetic energies below 10 MeV:

$$\frac{dE_e}{dx_e} = \frac{2\pi N e^4}{m_e c^2 \beta_e^2}(B(T) - 2ln\frac{I}{m_e c^2} - \delta), \tag{3.10}$$

where T is the kinetic energy of the δ-ray as it moves through the water, δ is the density effect correction, and the factor $B(T)$ depends only on the kinetic energy as

$$B(T) = ln\frac{\tau^2(\tau^2+2)}{2} + \frac{1+\tau^2/8-(2\tau+1)ln2}{(\tau+1)^2}, \tag{3.11}$$

with $\tau = T/m_e c^2$. Thus, the total number of Cherenkov photons emitted by a δ-ray of a kinetic energy T_e can be obtained:

$$N_\gamma = \int_{T_0}^{T_e} \frac{dN_\gamma}{dx_e}(\frac{dE_e}{dx_e})^{-1} dE_e. \tag{3.12}$$

The result is shown in Fig. 3.7 as a function of T_e.

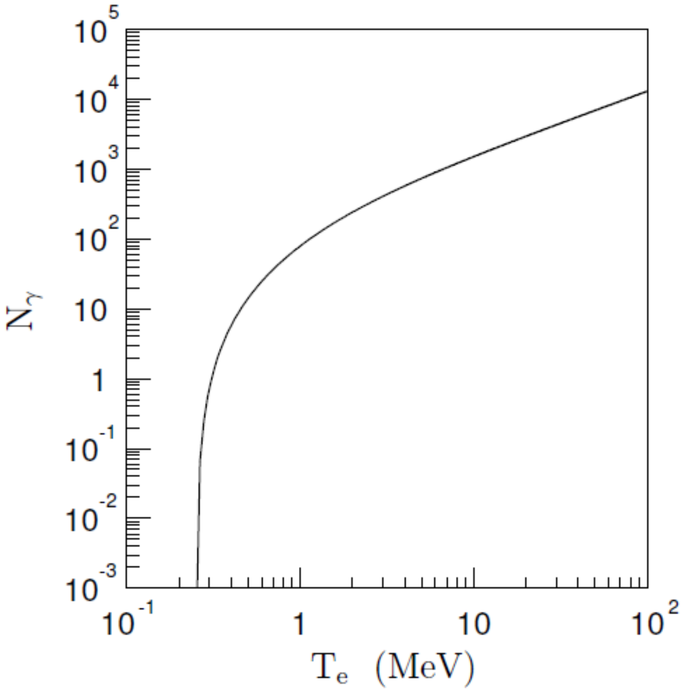

FIGURE 3.7: The total number of Cherenkov photons with wavelengths between 300 and 600 nm emitted by a δ-ray with initial kinetic energy T_e. The assumed medium corresponds to sea water.

Therefore, the total number of Cherenkov photons emitted by all the δ-rays that are produced per unit length, through the passage of a magnetic monopole, may be determined by:

$$\frac{dn_\gamma}{dx_e} = \int_{T_0}^{T_{max}} \frac{d^2N_e}{dT_e dx} \int_{T_0}^{T_e} \frac{dN_\gamma}{dx_e} (\frac{dE_e}{dx_e})^{-1} dE_e dT_e. \tag{3.13}$$

This is illustrated in Fig. 3.8. In comparison with the light emitted by a muon, it is observed that a magnetic monopole having a speed below the Cherenkov threshold could be detectable by ANTARES up to speeds of the order of 0.55, given the large quantity of light emitted by the δ-electrons.

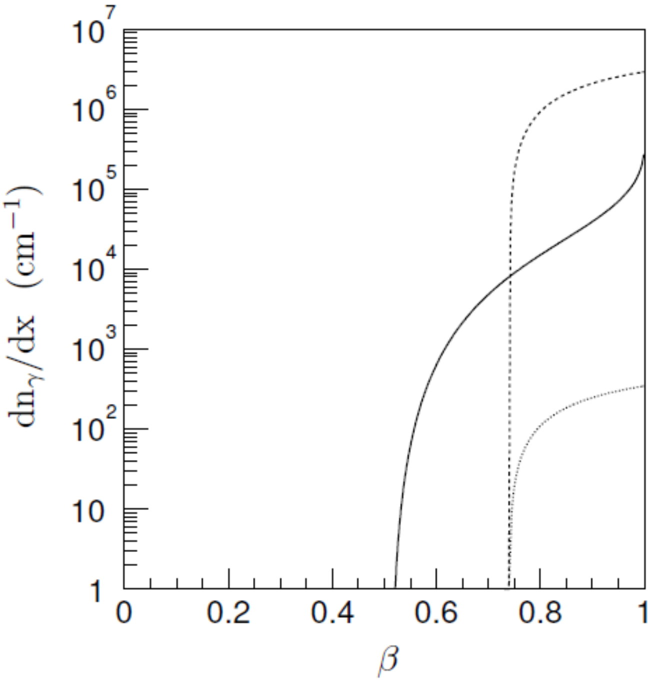

FIGURE 3.8: The total number of Cherenkov photons with wavelengths between 300 and 600 nm emitted by δ-rays that are produced per centimetre path length by a monopole with g_D (solid line), as a function of the monopole velocity. The number of Cherenkov photons emitted directly by a monopole (dashed line) and by a minimum ionising muon (dotted line) are also shown as a function of the velocity.

Angular distribution of indirect Cherenkov light

In order to simulate the photons emitted by δ-rays produced in the passage of a monopole, it is necessary to know their angular distribution. The Cherenkov photons are emitted at the characteristic Cherenkov angle θ_c with respect to the direction of the δ-ray. The Cherenkov angle can be expressed as

$$\cos\theta_c = \frac{1}{n\sqrt{1 - m_e^2c^4/(m_ec^2 + T)^2}}, \tag{3.14}$$

where T is the kinetic energy of the δ-ray as it passes through the water. The photons are distributed uniformly in the azimuthal angle ϕ_c around the path of the δ-ray.

The δ-ray production angle θ_e and the Cherenkov angle θ_c can be combined to determine the emission angle θ_γ of the δ-ray photons with respect to the direction of the monopole,

$$\cos\theta_\gamma = \sin\theta_e \sin\theta_c \cos\phi_c + \cos\theta_e \cos\theta_c. \tag{3.15}$$

Since both θ_e and θ_c are related to the kinetic energy of the δ-rays, the integral in Eq. (3.13) can be used to obtain the angular distribution of the photons in θ_γ. The result is shown in Fig. 3.9. It is assumed here that the angle between the δ-ray and the monopole is constant for the entire path of the δ-ray, i.e. the directional deviations of the δ-ray due to multiple scattering are ignored. The photons have a uniform distribution in the azimuthal angle.

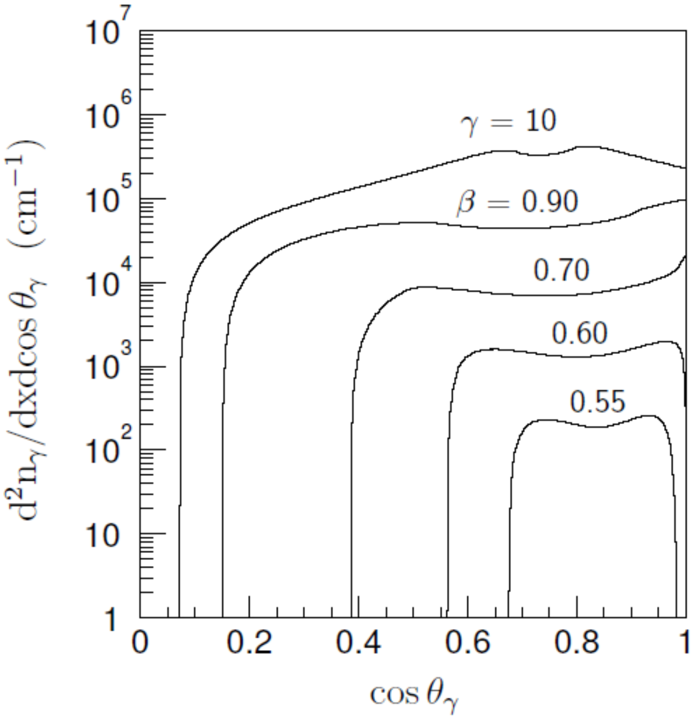

FIGURE 3.9: Angular distributions of the Cherenkov photons emitted by the δ-rays that are produced per centimetre path length by a monopole with g_D in the sea water, as a function of the emission angle θ_γ between the photons and the monopole. The angle between the δ-rays and the monopole is assumed to be constant. The distribution is shown for β = 0.55, 0.60, 0.70, 0.90 and γ = 10.

The angular spread of the photon emission in θ_γ increases with increasing velocity. Nevertheless, all photons are still emitted in forward directions with respect to the monopole, i.e. in directions with $\cos\theta_\gamma \geq 0$.

As a δ-ray passes through the water, it is detected continuously due to multiple scattering of atomic electrons and nuclei. The distribution of the corresponding scattering angle can be approximated by a Gaussian distribution with standard deviation [104]

$$\theta_0 = \frac{13.6MeV}{E_e\beta_e^2}\sqrt{\frac{x_e}{X_0}}(1+0.038ln\frac{x_e}{X_0}), \tag{3.16}$$

where E_e is the total energy of the δ-ray, x_e is the distance it travelled and $X_0 = 36.1$ cm is the radiation length of water [105]. As follows from this relation, the δ-ray undergoes larger scattering at lower energies. The scattering thus increases along the path of the δ-ray due to the δ-ray's energy loss. When multiple scattering of the δ-rays is taken into account, the angle between the δ-rays and the monopole varies continuously, which results in a larger angular spread of the Cherenkov photon emission. This is reflected by the angular distributions shown in Fig. 3.10 For monopole velocities above 0.60 c, the photons can even be emitted in backward directions.

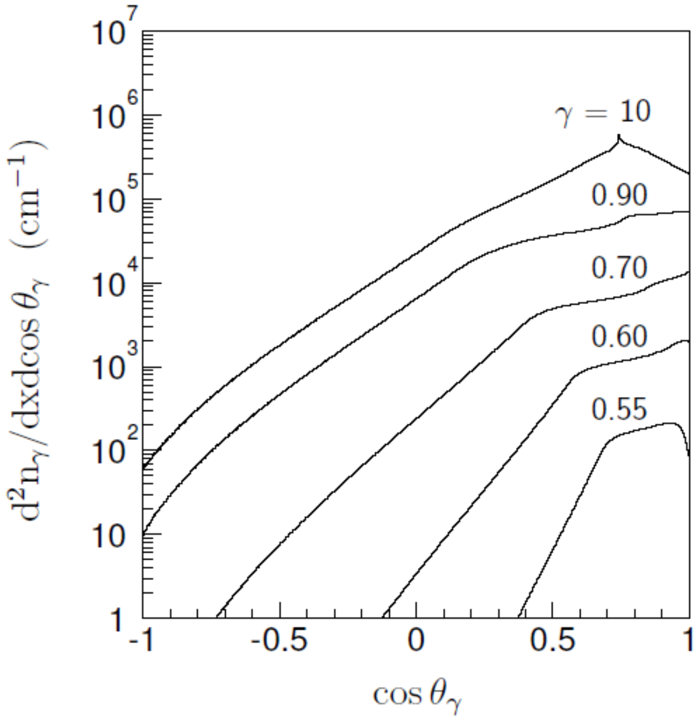

FIGURE 3.10: Angular distributions of the Cherenkov photons (see figure 4.7) with multiple scattering of the δ-rays taken into account.

The angular distribution for γ = 10 has a peak at $\cos\theta_\gamma \approx 0.74$. This is due to the contribution of the most energetic δ-rays at this velocity, which are produced in directions very close to the monopole direction. Due to their relatively high energies, these δ-rays travel larger distances and are less influenced by multiple scattering than less energetic δ-rays. They emit a considerable number of Cherenkov photons at the typical Cherenkov angle $\cos\theta_c \approx 0.74$, of which many are thus emitted at the same angle with respect to the monopole direction.

The angular distribution is more diffuse which might change the monopole signature. Therefore in the simulation indirect Cherenkov light is used in addition to the direct Cherenkov light for velocities above the Cherenkov threshold.

3.4 Conclusion

Neutrino telescopes are based on Cherenkov radiation emitted by electrically charged particles that pass through the detector. However, the electromagnetic energy losses of a magnetic monopoles in matter would be similar to that of an electrically charged heavy nucleus. Monopoles with sufficient speed could emit Cherenkov light in water, and thus be detectable by ANTARES.

Chapter 4

Data processing and simulation

4.1 Introduction

For any neutrino experiment, the software part, i.e simulation of events, different interactions and response of the detector as well as the reconstruction, is necessary. Thus, Monte Carlo production chains are used to simulate events one by one and their interactions in the medium, then their propagation into the detector and the response of PMTs is performed. The simulation covers also the surrounding background noise, the acquisition electronics and the triggering system of the telescope. After that, the event tracks are reconstructed.

4.2 Data processing

Data registred by the telescope are stored under HPSS disks at CC-Lyon [1] in a set of runs[2], each with a run number. They are ready for processing and reconstruction.

The simulation includes:

- generation of fundamental parameters (position, time, direction, velocity, energy etc.) of standard model particles, such as muons and neutrinos, as well as magnetic monopoles (see sections 4.3 and 4.5)
- propagation of background and signal particles through the Earth and the water, taking into account decay and interaction probabilities and propagating all secondary particles
- generation of Cherenkov light when the background or signal particle is close to the detector
- propagation of light through water
- calculation of the response of the PMTs and OM electronics including the generation of noise hits
- triggering (i.e. starting) the event readout if trigger conditions are fulfilled

The simulation is performed with the standard codes used in ANTARES. It is treated differently for various particle types and is therefore described separately for magnetic monopoles and background in sections 4.3 and 4.5.

---

[1] High Performance Storage System at the Computing Center of Lyon (in2p3).

[2] A run is a set of events with the same data taking conditions

The reconstruction refers to the production of the track of an incoming particle using the parameters of simulation or those registred by the detector (in the case of real data). The arrival time of Cherenkov light at an OM with known position and its amplitude is used to do the reconstruction using the BBfit algorithm described in 4.6.

4.3 Monopole simulation

Up-going MMs with one unit of Dirac charge, $g = g_D$, have been simulated using nine equal width ranges of velocity in the region $\beta_s = [0.5945, 0.9950]$. The nine intervals of the velocity are defined in Table 4.1.

β_s range number	β_s range simulated
1	[0.5945 , 0.639]
2	[0.639 , 0.6835]
3	[0.6835 , 0.728]
4	[0.728 , 0.7725]
5	[0.7725 , 0.817]
6	[0.817 , 0.8615]
7	[0.8615 , 0.906]
8	[0.906 , 0.9505]
9	[0.9505 , 0.995]

TABLE 4.1: The monopole velocity ranges.

MMs have been simulated using a Monte Carlo program based on GEANT3 [106]. This was developed by Bram van Rens [107]. The simulation is independent of the MM mass and the incoming direction of MMs was distributed isotropically over the lower hemisphere. The propagation and detection of emitted photons is processed inside a virtual cylindrical surface named the *CAN* surrounding the instrumented volume around the detector. A high radius is chosen to take into account the large amount of light emitted by MMs. Fig. 4.1 represents the CAN.

4.3.1 Generating monopoles with *genmon*

The genmon package is based on genneu v5r1 [106]. It generates monopole tracks in the CAN surface. Several run scripts are present in the code, each generating monopole tracks in a specific velocity range. In this way different CAN sizes can be used for different velocities, which is preferable because of the strong dependence of the light yield on the velocity. The velocity range is defined by the energy values of the CUT parameter in the run scripts. The monopole has been defined in geamon (described in section 4.3.2) as a particle with a mass of 10 GeV and particle ID 666. The energy is then related to the velocity by

$$E = \frac{10GeV}{\sqrt{(1-\beta^2)}}. \tag{4.1}$$

The velocity intervals used in the code are in the range $0.55 < \beta_{mon} < 0.995$, with the use of logarithmic interpolation to determine the Cherenkov emission for unavailable intervals.

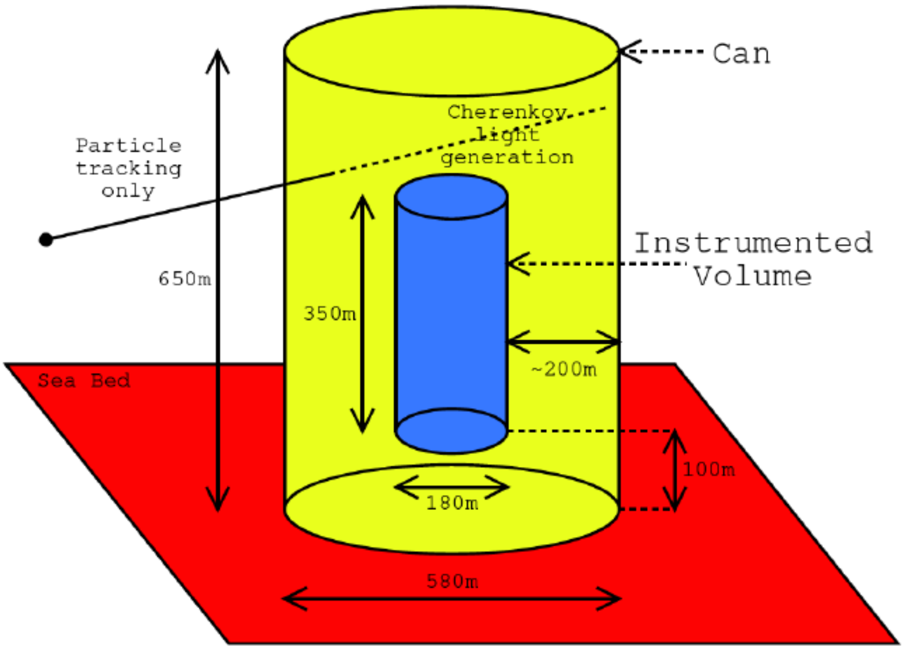

FIGURE 4.1: The cylindrical volume (CAN) where events are generated. It is surrounding the instrumented volume which is supposed to represent the detector. The radius of the CAN is chosen to be big enough to take into consideration the large amount of light emitted by MMs.

4.3.2 Tracking with *geamon*

The code geamon is based on GEASIM [108]. It uses the files produced by genmon as input, and produces event files containing the detector's response to the monopole signal.

For direct Cherenkov radiation, the light intensity I as a function of the length traveled L by the photons and the length of attenuation λ_{att}

$$I(L) \propto \frac{e^{-L/\lambda_{att}}}{L} \tag{4.2}$$

has been taken into account in the simulation.

For indirect Cherenkov radiation, this light intensity is

$$I(L) \propto \frac{1}{L^2} e^{-L/\lambda_{att}} \tag{4.3}$$

because of the quasi-isotropic nature of photons (Fig. 3.10).

4.4 Magnetic monopole Trigger

As mentioned before, a system of triggers is applied to the data. Therefore, it is important to evaluate the trigger effeciency in ANTARES for magnetic monopoles. In general, only hits that passed a threshold of 0.3 photo-electrons (pe) are considered. Before introducing different triggers existing, these are some common notations:

- L1 corresponds to either a hit with a large amplitude (3 pe) or a coincidence of at least two hits on the same storey in an interval of 20 ns.
- T3 is a coincidence of two L1 on two storeys among three adjacents, in an interval of 100 ns or 200 ns.

Other triggers are defined in ANTARES for other purposes (or other analyses). It is necessary to evaluate different triggers and select the one that is suitable for magnetic monopoles (trigger efficiency) given the large amount of light they would emit in a neutrino telescope.

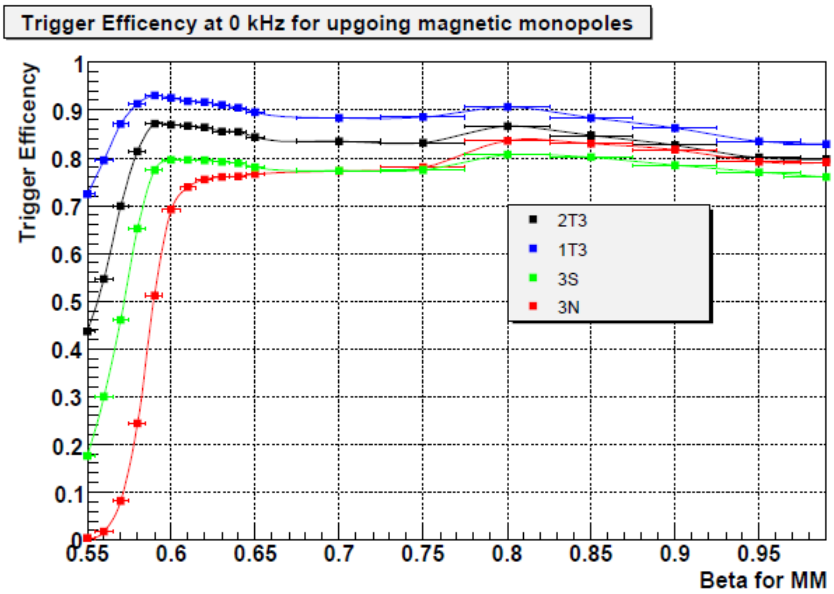

FIGURE 4.2: Trigger efficiency of up-going magnetic monopoles as a function of their velocity (β).

Among all triggers presented in Fig. 4.2, T3 is the most efficient. Thus, only T3 triggers are considered in this analysis. The definition of the other triggers 3S and 3N are given in [29].

4.5 Background simulation

Unlike magnetic monopoles, before reaching the CAN, the interactions of muons and atmospheric neutrinos are simulated, as well as their possible secondary particles. Then, once these particles in the CAN, the detailed simulation of the Cherenkov photon propagation to the detector is performed, as well as the response of photomultipliers. Finally, the surrounding background noise is simulated, as well as acquisition electronics and triggering systems of the telescope.

The simulation of atmospheric muons is carried out using the generator MUPAGE [109] based on the parametrisation of the angle and energy distributions of muons under-water as a function of the muon bundle multiplicity [110]. MUPAGE produces muon events on the surface of the virtual cylinder.

Up-going atmospheric neutrinos from the decay of pions and kaons are simulated using the package GENHEN [111, 112] assuming the model from the Bartol group [113, 114] which does not include the decay of charmed particles. The Bartol model [113] combined to RPQM model [118] have been used, as they predict the higher flux of neutrinos and are the most conservative.

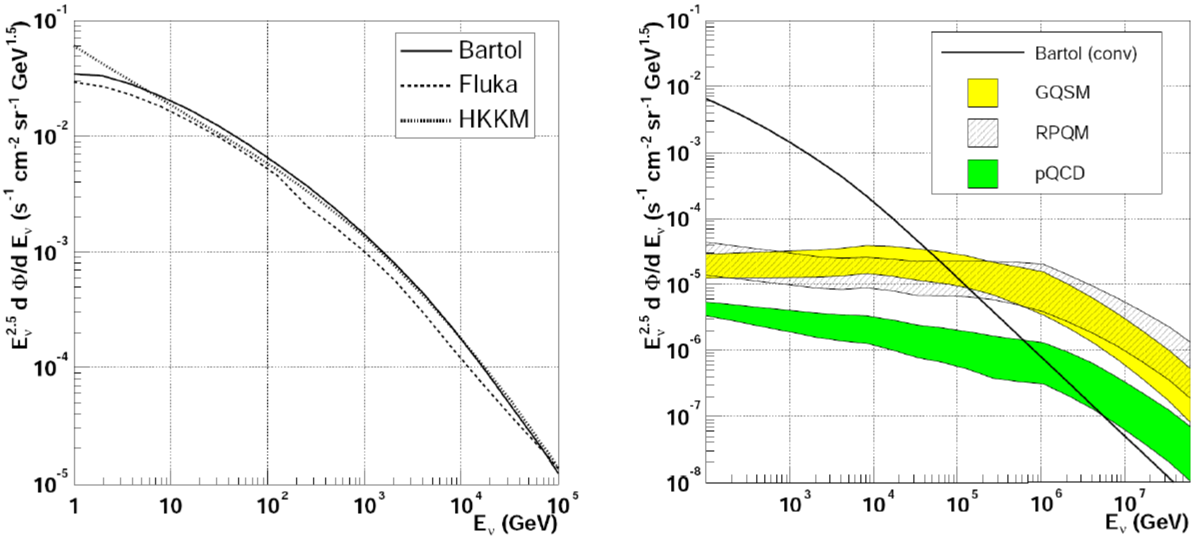

FIGURE 4.3: Left: atmospheric neutrino spectrum with energies $\leq 10^5$ GeV, calculated with the model Bartol [113], Fluka [115] and HKKM [116]. Right: flux of atmospheric neutrinos from the decay of charmed mesons, calculated with the models GQSM, RPQM, pQCD [117] and compared with the flux predicted by the Bartol model.

4.5.1 Propagation to the CAN

To propagate muons into the CAN, GENHEN uses the package MUSIC [119] that simulates their energy loss and their multiple scattering. Only events that could reach the CAN are kept and used in the next step.

4.5.2 Generation of photons in the CAN and detection

The program KM3 [120] propagates muons in the CAN and simulates Cherenkov photons produced, as well as their dispersion, their absorption and their scattering in watter. The photons produced from the interaction of neutrinos inside the CAN are also simulated with the program GEASIM [108].

The response of PMTs is simulated considering the efficiency and the optical properties.

4.6 Reconstruction

The reconstruction algorithm called BBfit (described in [121]) has been developed as a robust reconstruction method, which produces reliable results without precise positioning calibration. Its strict hit selection leads to an excellent up-down separation while keeping a good effeciency.

The BBfit concept is based on the fact that both a detector line and a muon track can be considered as straight lines in space. Apart from the special case that these two lines are parallel (as in the case of an exactly vertical track) one can define on the muon track a point of closest approach with respect to the detector line. Most of the Cherenkov light must be seen in the vicinity to this point of closest approach. This fact is used in the hit selection as well as in the fitting algorithm.

Only hits due to direct Cherenkov photons are selected for the fit. Tails due to scattering and electromagnetic activity are ignored, keeping the fit simple. A χ^2-like function is defined and minimized.

4.6.1 Hit treatment

The geometry of the three optical modules on a storey is ignored in BBfit. A storey is considered as space point centered on the detector line. The procedure always starts from the list of snapshot hits. Triggered hits are only considered if snapshot hits are absent (in LED beacon events for instance). As a first step, time and charge calibration is applied. For real data the default method is the automatic selection of a calibration set based on the method described in [122]. The calibrated hit times t_i are given in ns with respect to the start of the run and the hit amplitudes a_i are given in photoelectrons. In order to avoid large numbers during the fitting procedure the hit times are reset to time differences with respect to the first triggered hit.

Only one hit per storey is allowed in the fitting procedure. Therefore the following treatment of the calibrated snapshot hits of a physics event is applied:

- All hits from the same storey are time ordered, regardless from which optical module they originate
- Hits which are closer in time than 20 ns are merged
- Merging implies adding their amplitudes and keeping the time of the earlier hit
- When hits from different optical modules are merged, the merged hit obtains a bonus charge of 1.5 photoelectrons
- A bonus charge is only given once to a merged hit

The bonus charge gives a higher weight to coincidences between two hits on different optical modules compared to a single high charge pulse. This becomes important when forming the T3 condition. All subsequent steps are based on the pre-treated hit list.

4.6.2 Fitting procedure

Before starting any fit, the list of selected hits is examined. If less than 5 hits are in this list, no fit attempt is made. If all selected hits are on a single detector line, a procedure for single line fits is started. If the hits are distributed over several detector lines, a multi-line fit procedure is performed.

Fit object

Particle track

A particle track is considered as a straight line in space (multiple scattering and other effects which could deviate the particle from its straight trajectory are ignored). It is illustrated in Fig. 4.4. The particle is assumed to move with the speed of light in vacuum (a value of 0.3 m/ns is used in the code). All space-time points which are part of the track can be parameterized as

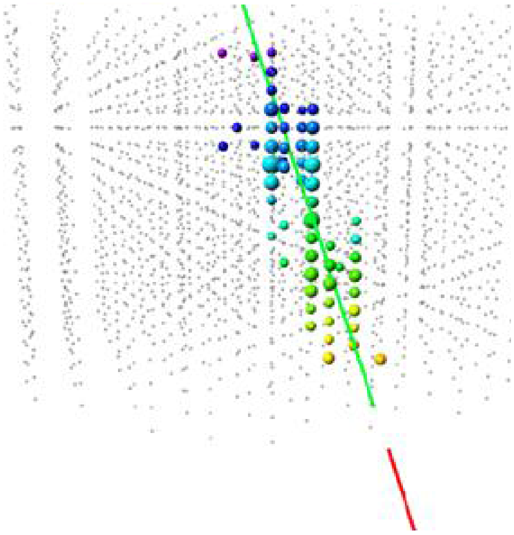

FIGURE 4.4: Illustration of a track passing through a neutrino telescope. The gray points represent the floors.

$$\vec{p}(t) = \vec{q}(t_0) + c(t - t_0)\vec{v} \tag{4.4}$$

The particle passes through point ($\vec{q}$) at time t_0 and moves in the direction $\vec{v}$. ($\vec{q}$) can be shifted along the track by redefining t_0. Therefore the track is defined by a total of 5 parameters (Fig.4.5): three values to fix ($\vec{q}$) for a given time and two angles to define $\vec{v}$. Now an exactly vertical detector line along the z-axis is considered, i.e. given by (0, 0, z). From purely geometrical considerations the point of closest approach between the detector line and the particle track can be defined. The point of closest approach along the z-axis is:

$$z_c = \frac{q_z - v_z(\vec{q} \cdot \vec{v})}{1 - v_z^2} \tag{4.5}$$

through which the particle passes at time:

$$t_c = t_0 + \frac{q_z v_z - (\vec{q} \cdot \vec{v})}{c(1 - v_z^2)} \tag{4.6}$$

at a distance

$$d_c = \sqrt{p_x^2(t_c) + p_y^2(t_c) + (p_z(t_c) - z_c)^2}. \tag{4.7}$$

If the track is exactly vertical, and therefore parallel to the detector line, then $t_c = t_0$ and $z_c = q_z$ are chosen.

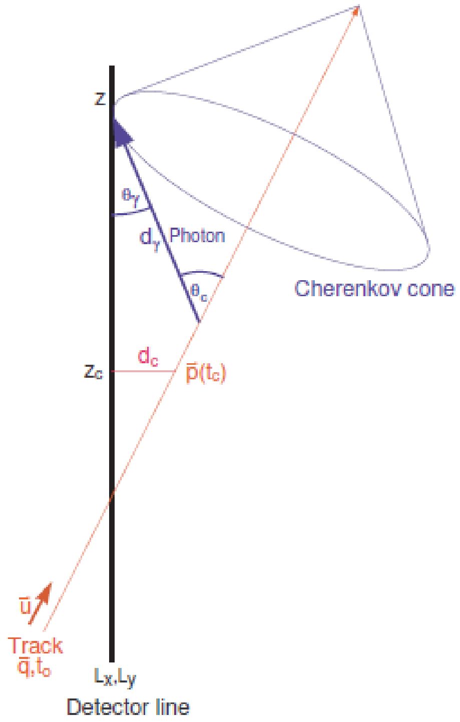

FIGURE 4.5: The track and the variables used to describe it.

The arrangement of a track and a single detector line is invariant against rotations around the z-axis. The track can be conveniently reparametrized in terms of z_c, t_c, d_c and v_z (the latter being nothing other than the cosine of its zenith angle). This means that the track is now fully defined by only 4 parameters. To build a fitting function it is necessary to know (a) the arrival time t_γ of a Cherenkov photon at the detector line position (0, 0, z), (b) its corresponding travel path d and (c) its inclination with respect to the detector line $\cos\theta_\gamma$. All three values can be derived from the four track parameters defined above:

$$d_\gamma(z) = \frac{n}{\sqrt{n^2-1}}\sqrt{d_c^2 + (z - z_c)^2(1 - v_z^2)} \tag{4.8}$$

$$t_\gamma(z) = (t_c - t_0) + \frac{1}{c}\left((z - z_c)v_z + \frac{n^2-1}{n}d_\gamma(z)\right) \tag{4.9}$$

$$\cos\theta_\gamma(z) = (1 - v_z^2)\frac{z - z_c}{d_\gamma(z)} + \frac{v_z}{n}. \tag{4.10}$$

These equations hold exactly for Cherenkov photons of a given wavelength. Dispersion and group velocity effects, as well as delays due to light scattering in a medium, are ignored. A refractive index $n = 1.38$ is used in the code.

Bright point

Contrary to a particle track, a bright point is a point-like light source which emits a single light flash at a given moment. It is illustrated in Fig. 4.6. The light emission is assumed to be isotropic. The model of a bright point applies not only to artificial light sources such as LED and laser beacons, but also to sparks (as have been observed in some optical modules) and to light from hadronic and electromagnetic showers, for which the actual extension of the shower is significantly smaller than the relevant scales of the detector. A bright point is defined by four parameters: its position $\vec{q}$ and its time t_0. In analogy with the definitions of the point of closest approach as done for particle tracks, it is straightforward to see that for a bright point $z_c = q_z$, $t_c = t_0$ and

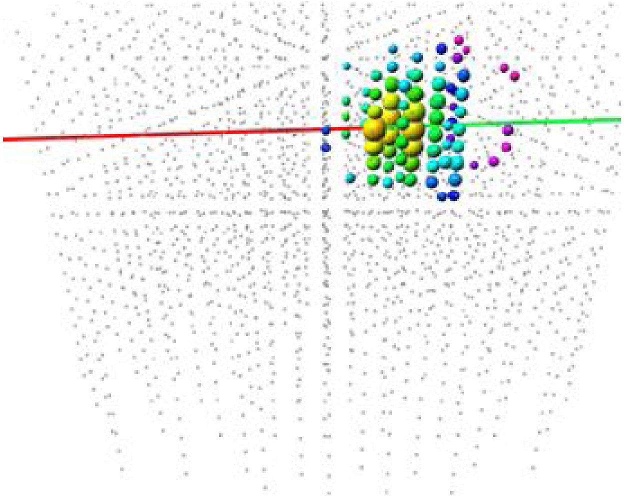

FIGURE 4.6: Illustration of a bright point-like event in a neutrino telescope. The gray points represent the floors.

$$d_c = \sqrt{q_x^2 + q_y^2} \tag{4.11}$$

The three parameters z_c, t_c, d_c fully determine the bright point with respect to a single detector line at (0, 0, z), which again means that the number of parameters is reduced by one in this particular case. The photon arrival time t_γ, its travel length d_γ and its angle with respect to a given arrival point z along the detector line can thus be determined in analogy to the case of a particle track.

$$d_\gamma(z) = \sqrt{d_c^2 + (z - q_z)^2} \tag{4.12}$$

$$t_\gamma(z) = t_0 + \frac{n}{c} d_\gamma \tag{4.13}$$

$$\cos\theta_\gamma(z) = \frac{z - q_z}{d_\gamma}. \tag{4.14}$$

As for particle tracks, it is assumed that all photons have one particular wavelength, such that a refractive index of $n = 1.38$ is appropriate.

Fit function

The fitting function exploits the time difference between the hit times t_i and the expected arrival time of photons from the track or bright point t_γ, as in a standard χ^2 fit. Further the expected amplitude versus distance relation of the measured hit amplitudes a_i is used.

$$Q = \sum_{i=1}^{N_{hit}} [\frac{(t_\gamma - t_i)^2}{\sigma_i^2} + \frac{a(a_i)d(d_\gamma)}{< a > d_0}]. \tag{4.15}$$

The timing error, σ_i, is set to 10 ns for $a_i > 2.5$ photoelectrons and to $\sigma_i = 20ns$ otherwise. This might seem large with respect to the transit time spread of 1.3 ns for the ANTARES phototubes, but it has been confirmed by exploring the time residuals of typical track fits.

The second term is not organized as a difference between theoretical value and measured amplitude in order to avoid penalties from large theoretical amplitudes. Instead, the chosen form gives a penalty to the combination of high amplitude and large distance. The product is normalized by the average amplitude, $< a >$, to compensate for the fact that higher energy tracks or showers will produce more light at the same distance. The normalization $d_0 = 50m$ serves to balance the weight between the two terms. Hit amplitudes a_i and photon travel distances d_γ are not taken directly from the calibrated detector measurements. The amplitudes are first corrected for the angular acceptance of the floor. A very simple form (moon phases) can be numerically derived from the arrangement of the optical modules in a floor and the corresponding angular acceptance function of a single optical module. This leads to a corrected hit amplitude a_i' of

$$a_i' = \frac{2a_i}{\cos\theta_\gamma + 1} \tag{4.16}$$

The average amplitude $< a >$ is calculated from these corrected hit amplitudes

$$< a >= \frac{1}{N_{hit}} \sum_1^{N_{hit}} a_i' \tag{4.17}$$

To be used in the fit function, the amplitudes are further modified

$$a(a_i) = \frac{a_0 a_i'}{\sqrt{a_0^2 + a_i'^2}} \tag{4.18}$$

The function $a(a_i)$ introduces an artificial saturation such that for $a_i' << a_0$ one finds back $a \approx a_i'$, whereas for $a_i' >> a_0$, one gets $a \approx a_0$: the saturation value of $a_0 =$ 10 photoelectrons. This limits the influence of the large dispersion in the dynamic ranges of the different modules which is currently not simulated.

A similar trick is applied to the photon travel distance.

$$d(d_\gamma) = \sqrt{d_1^2 + d_\gamma^2} \tag{4.19}$$

For large distances $d_\gamma >> d_1$ one finds back $d \approx d_\gamma$, whereas for very small distances $d_\gamma << d_1$ one gets $d \approx d_1$ with $d_1 = 5m$. This avoids an excessive pull of the fit object towards the detector line.

Minimization procedure

The MIGRAD function of the MINUIT package [123] is used to perform the actual minimization. To perform a single line fit, the fit object is parameterized through its point of closest approach, i.e. z_c, t_c, d_c and v_z for the track fit. Eq. (4.8) and (4.12) are used to obtain d_γ, t_γ, $\cos\theta_\gamma$ for a given particle track or bright point. The multi-line fits use the same set of equations. A loop is performed over all detector lines which have selected hits, and for each line a coordinate transformation is done to place the line at the nominal position (x,y) = (0,0). The multi-line arrangement breaks rotational symmetry, therefore all parameters are needed to determine the track or the bright point, as indicated in Table 4.2.

	single line	multi line
track	4	5
bright point	3	4

TABLE 4.2: Number of fit parameters.

Therefore, two parameters defining the quality of these reconstructions are introduced, $t\chi^2$ for the track fit, and $b\chi^2$ for the bright-point fit. The reconstruction gives for each event a $t\chi^2$ and a $b\chi^2$ value, such that if $t\chi^2 < b\chi^2$, the event should be considered a track, and if $t\chi^2 > b\chi^2$ it should be considered a bright point.

4.7 Run-by-run MC strategy

Environmental conditions in a marine environment are not stable and constant in time. Variations affect data acquisition in an under-sea neutrino telescope like ANTARES. Biological [124] and physics phenomena [125] show evolving trends on seasonal timescales producing a periodical change of the background optical rates registered at the detector. Short term variations are also present as the optical rates are modified by the sea current velocity. In addition to environmental effects, the detector elements might not collect data continuously, because of temporary or permanent malfunctioning of the optical modules or lack of connection to some part of the apparatus, besides, the lines of the detector are always moving because of the sea current. Finally, it is possible to modify the trigger algorithms applied to the data taking along the life of the detector.

A reliable Monte Carlo simulation of the detector should reproduce all these effects. An efficient way to account for the variations of the optical background is to extract related information directly from the data. The TriggerEfficiency program takes this information from raw data files. It considers the counting rate in short segments of the data stream, about 100 ms long, and simulates the corresponding optical background according to the measured charge distribution of hits. DAQ conditions (the status of each detector element, the active triggers, the data filtering parameters) for each run are stored in the ANTARES database, which is accessed by the TriggerEfficiency code, and used during the simulation.

The resulting output has the same format of raw data and is processed using the available reconstruction algorithm to extract physics information from data. This approach called the run-by-run strategy [126] has significantly improved the data/MC agreement, and allowed for a better monitoring of the time evolution of the data acquisition.

4.8 Blind approach and burn sample

The analysis considered in this report uses five years of ANTARES data collected between January 2008 and December 2012 giving rise to a total livetime of 1121 active days. To avoid any experimental bias, the analysis is based on a unblinding policy which consist in performing the study on MonteCarlo data, and using a test sample of data corresponding to 109 days in order to make a comparison data/MC. The test sample is about 10% of the total data set (only 0-ending runs).

4.9 Conclusion

After the simulation of magnetic monopoles and atmospheric background and the reconstruction of events, the blind approach allows the use of a sample of 10% of the total amount of data. This sample is used only to make a comparison between data and Monte Carlo distributions, which shows a good agreement as will be presented in section 5.5. The event selection and the optimization of the cuts will be discussed in the next chapter, in order to obtain the best expected sensitivity.

Chapter 5

Analysis and results

5.1 Introduction

Using the blinding policy, the study has been performed on Monte Carlo data to obtain the sensitivity on magnetic monopoles. A comparison between real and Monte Carlo data has been done using about 10% of the total sample collected by ANTARES between 2008 and 2012. In this study the Model Rejection Factor is optimised for the full collection of Monte Carlo data corresponding to 5 years of data taking.

5.2 Analysis strategy

The principle of the analysis strategy for upgoing magnetic monopoles, in the case of a blinding policy, can be synthesized in four steps:

- Definition of the discriminative variables to be used to isolate magnetic monopoles from the atmospheric background.
- Optimisation of the Model Rejection Factor to obtain the best sensitivity for magnetic monopoles.
- Checkout of the agreement of distributions between Monte Carlo simulations and a sample of real data.
- Definition of the optimal cuts and calculation of the sensitivity for each velocity interval of magnetic monopoles.
- Unblinding request for all data taken between 2008 and 2012 and calculation of the final limits on flux.

Before proceeding to all of this, some preliminary cuts have to be applied in order to reduce the high amount of atmospheric background.

5.2.1 Preliminary cuts and reduction of background

Some basic quality cuts have been applied to the data to ensure good data taking conditions [127].

Since this is a search for up-going magnetic monopoles, a selection cut which seems reasonable and which is expected to remove a large part of down-going muons and neutrinos concerns the zenith angle.

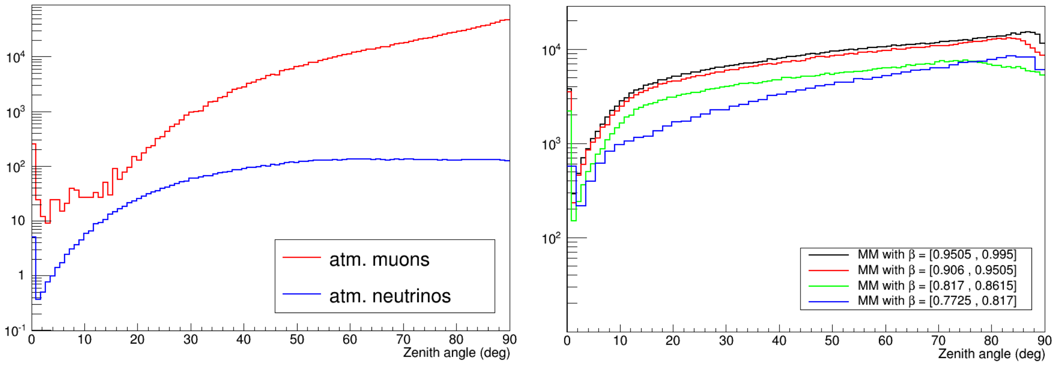

FIGURE 5.1: Left panel: Number of events as a function of the reconstructed zenith angle for up-going atmospheric muons (red) and up-going atmospheric neutrinos (blue). Right panel: Number of up-going magnetic monopole events as a function of the reconstructed zenith angle, for $\beta_s \approx 0.97$ (black), $\beta_s \approx 0.93$ (red), $\beta_s \approx 0.83$ (green) and for $\beta_s \approx 0.79$ (blue).

The cut $\theta_{zen} \leq 90^\circ$, where θ_{zen} is the reconstructed zenith angle, allows to exclude a large proportion of down-going particles. Nevertheless, some tracks are badly reconstructed, and the track reconstruction quality parameter $t\chi^2$ (see Fig. 5.2) should be used as well to improve the purity of up-going signals.

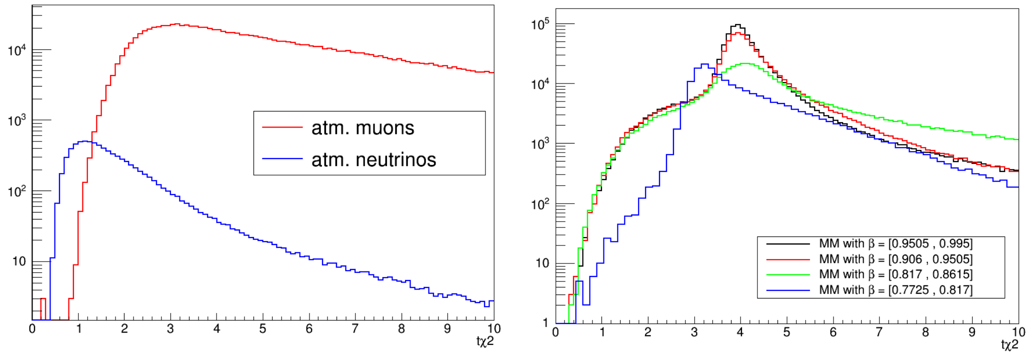

FIGURE 5.2: Left panel: Number of events as a function of the quality parameter of the track reconstruction $t\chi^2$ for up-going atmospheric muons (red) and up-going atmospheric neutrinos (blue). Right panel: Number of up-going magnetic monopole events as a function of $t\chi^2$, for $\beta_s \approx 0.97$ (black), $\beta_s \approx 0.93$ (red), $\beta_s \approx 0.83$ (green) and for $\beta_s \approx 0.79$ (blue).

Therefore, additional cuts on the track fit quality parameter are implemented to remove misreconstructed atmospheric muon tracks. In particular, the requirement $t\chi^2 \leq b\chi^2$ is applied to favour events reconstructed as a track rather than those reconstructed as a bright point.

5.2.2 Discriminative variables

The strategy followed in this study divides the whole velocity ranges of magnetic monopoles into two regions, for low and high speeds. The aim is to distinguish between the region where to use the velocity as a free parameter to be fitted in the reconstruction, and the region where the velocity of particles is assumed to be equal to 1.

High velocity ranges

At high velocity intervals ranging from $\beta_s = 0.8170$ to $\beta_s = 0.9950$ (four bins), magnetic monopoles emit a large amount of light compared to that emitted from atmospheric muons and neutrinos, which allows their signal to be isolated. Hence, a discriminative parameter representing the amount of light emitted by each particle should be found to distinguish the MM signal.

The number of hits called N_{hit} in the used reconstruction algorithm BBfit (4.6) seems to be the most suitable. The so-called *track hit* in BBfit are the hits belonging to the same floor such as the center of the floor is its coordinates, the time of the first hit represents its time and the sum of the hits charges represents its charge. N_{hit} is then the number of floors with selected track hits (see Fig. 5.3).

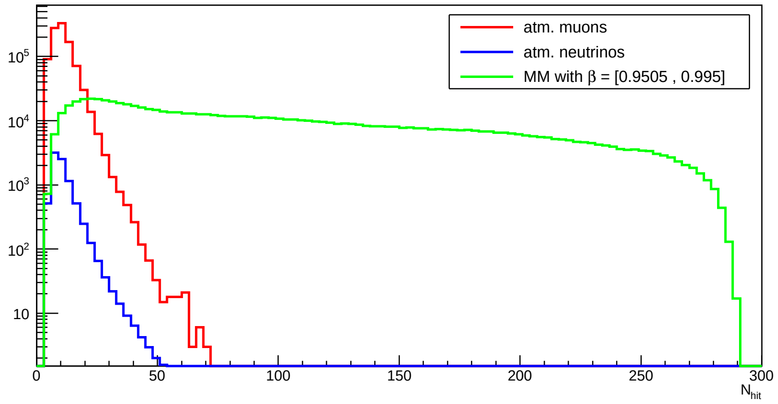

FIGURE 5.3: N_{hit} distribution for atmospheric muons (red histogram), and atmospheric neutrinos (blue histogram). For comparison, the distribution of N_{hit} for MMs simulated in the velocity range $[0.9505, 0.9950]$ (green histogram) is also shown. At high velocities, N_{hit} provides a good discrimination for MM signals after applying the cuts zenith $\leq 90^\circ$ and $t\chi^2 \leq b\chi^2$.

However, N_{hit} becomes less efficient at lower velocities as the light emission by particles is lower below the Cherenkov threshold. Hence, a second discriminative variable needs to be introduced to further reduce the background. Following [121], the variable α is defined from a combination of the track fit quality parameter and N_{hit}:

$$\alpha = \frac{t\chi^2}{1.3 + \left(0.04 \times (N_{hit} - N_{df})\right)^2}, \tag{5.1}$$

$N_{df} = 5$ is the number of free parameters in the reconstruction algorithm. Example of α distribution is shown at Fig. 5.4. This parameter has the advantage of including the track fit quality parameter balanced with the brightness of the events, avoiding that bright events get cut by the condition applied on the $t\chi^2$ variable.

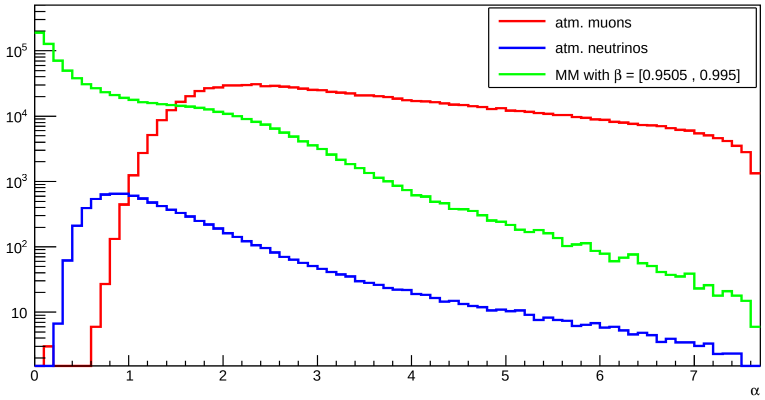

FIGURE 5.4: Distribution of the α variable for atmospheric muons (red histogram) and atmospheric neutrinos (blue histogram). For comparison, the distribution of the α variable for MMs simulated in the velocity range $[0.9505, 0.9950]$ (green histogram) is also shown. The cuts zenith $\leq 90°$ and $t\chi^2 \leq b\chi^2$ have been applied.

Low velocity ranges

At lower velocities, as mentioned before, the light emission by magnetic monopoles becomes low making the variable N_{hit} less efficient to distinguish their signal from atmospheric background. However, a large part of atmospheric background has a velocity $\beta = 1$ in seawater.

The reconstruction algorithm has been modified to include β_{fit} as a free parameter to be reconstructed for all particles instead of assuming $\beta = 1$. It seems that this modified BBfit is appropriate to the region of low velocities between bs = 0.5945 and bs = 0.8170 (five bins). While atmospheric muons and neutrinos have high speeds, magnetic monopoles with low speeds could be distinguished. For each of the five low beta bins, only events reconstructed with β_{fit} in the range of simulated β were used in the final selection. For example, at the range $\beta_s = [0.5945, 0.6390]$, only events with reconstructed velocity $\beta_{fit} = [0.5945, 0.6390]$ were selected.

Fig. 5.5 shows the distributions of β_{fit} for atmospheric muons, neutrinos and magnetic monopoles compared to the burn sample of real data, for different velocity ranges of MMs.

This leads to define the β resolution for monopoles. The reconstructed resolutions ($\beta_{simulated} - \beta_{fitted}$) are shown in Fig. 5.6.

The same discriminative variables N_{hit} and α are used, with a slight difference in the definition of the last one since $N_{df} = 6$ in this case because β_{fit} is taken as an additional variable in the reconstruction.

The following step consists in applying specific cuts on the N_{hit} and α parameters in order to maximize the signal-to-noise ratio. Fig. 5.7 shows a 2D distribution of α as a function of N_{hit} for one range of MM velocity. On the left upper quadrant, it is shown that the magnetic monopole signal is well isolated from atmospheric background. This quadrant has been determined by a couple of cuts on N_{hit} and α

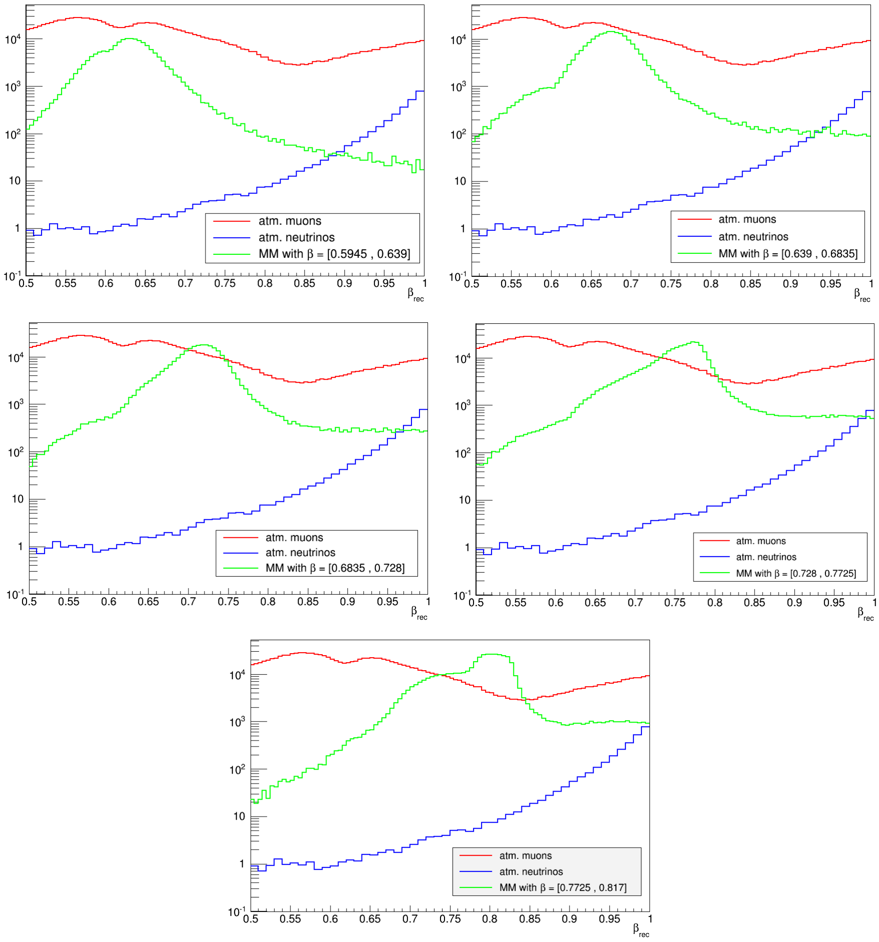

FIGURE 5.5: Distributions of β_{fit} for atmospheric muons (red histogram), atmospheric neutrinos (blue histogram) and data (black histogram). Different plots corresponding to different ranges of simulated velocity for MMs are presented. The cuts zenith ≤ 90° and $t\chi^2 \leq b\chi^2$ have been applied.

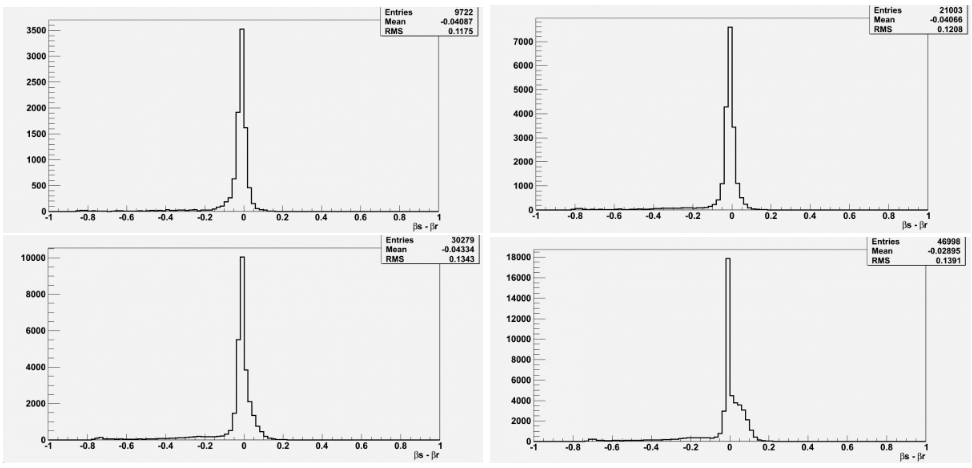

FIGURE 5.6: MM β resolutions ($\beta_{simulated} - \beta_{fitted}$) for different ranges of simulated velocity, $0.639 < \beta_s \leq 0.6835$ (top left), $0.6835 < \beta_s \leq 0.728$ (top right), $0.728 < \beta_s \leq 0.7725$ (bottom left) and $0.7725 < \beta_s \leq 0.817$ (bottom right).

represented by the horizontal and vertical lines in the figure.

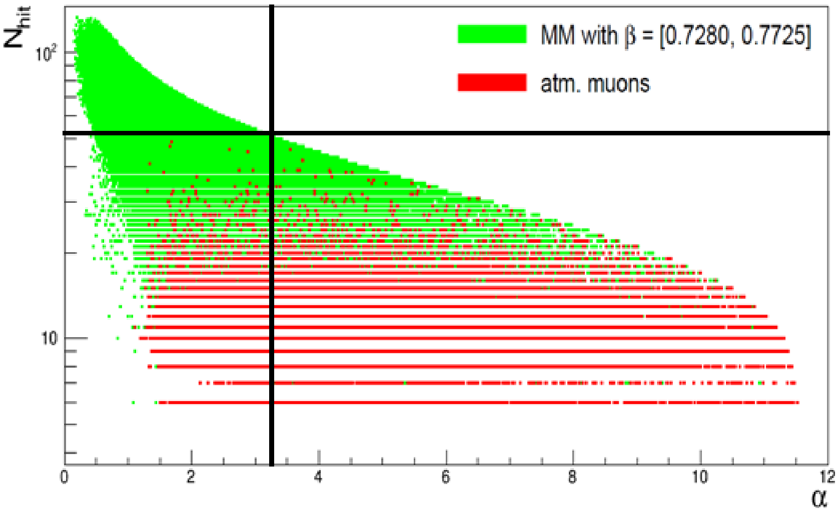

FIGURE 5.7: Two-dimensional distribution of α and N_{hit}, for atmospheric muons and MMs simulated in the velocity range $[0.7280, 0.7725]$. The cuts zenith $\leq 90°$ and $t\chi^2 \leq b\chi^2$ have been applied, as well as the cut $\beta_{fit} = [0.7280, 0.7725]$. The vertical and horizontal lines show the cuts applied after optimization. No neutrinos survived at this range of β_s.

Fig. 5.7 shows also that atmospheric neutrinos are rejected (or at least, a very low number of events remained) because of the applied cut $\beta_{fit} = [0.7280, 0.7725]$ which removes all the events whose velocities are out of this range.

5.2.3 MRF optimisation

In order to perform an optimization to obtain the best sensitivity, i.e to set the best limit if no signal is present, the model of the rejection factor [128] has been widely used in high energy neutrino detectors (AMANDA, IceCube , ANTARES). The method is only based on the expected background, derived from MonteCarlo simulations, and not looking to real data to avoid any experimental bias. The Model Rejection Factor (MRF) consists in playing with cuts such as the maximum of sensitivity is obtained. The 90% C.L. sensitivity $S_{90\%}$ is calculated with the usual Feldman/Cousins formula [129], considering events which follow a poisonnian distribution :

$$S_{90\%}(cm^{-2} \cdot s^{-1} \cdot sr^{-1}) = \frac{\bar{\mu}_{90}}{S_{eff} \times T(s)}, \tag{5.2}$$

where T is the duration of data taking, and S_{eff} and $\bar{\mu}_{90}$ are defined as :

$$S_{eff} = \frac{N_{MM}}{Flux} and \bar{\mu}_{90} = \sum_{n=0}^{\inf} \mu_{90}(b,n) \frac{b^n e^{-b}}{n!}, \tag{5.3}$$

with N_{MM} the number of remaining up-going magnetic monopole events after cuts, and the $Flux$ given by:

$$Flux(cm^{-2} \cdot sr^{-1}) = \frac{N_{gen}}{A_{can} \times 2\pi}, \qquad (5.4)$$

where N_{gen} is the number of generated up-going monopoles, A_{can} is the CAN area, and where b is the number of expected background events remaining after cuts, and $\mu_{90}(b, n)$ is given by the Feldman-Cousins tables.

Cuts on α and N_{hit} will be optimized so as to minimize the model rejection factor, which is the ratio:

$$MRF = \frac{\bar{\mu}_{90}}{N_{MM}}. \qquad (5.5)$$

The MRF is then computed for a given N_{hit} varying from 0 to 300, and for a given α varying from 0 to 10. As an example, Fig. 5.8 illustrates the MRF optimisation for the monopole velocity $\beta_s = [0.7725, 0.817]$.

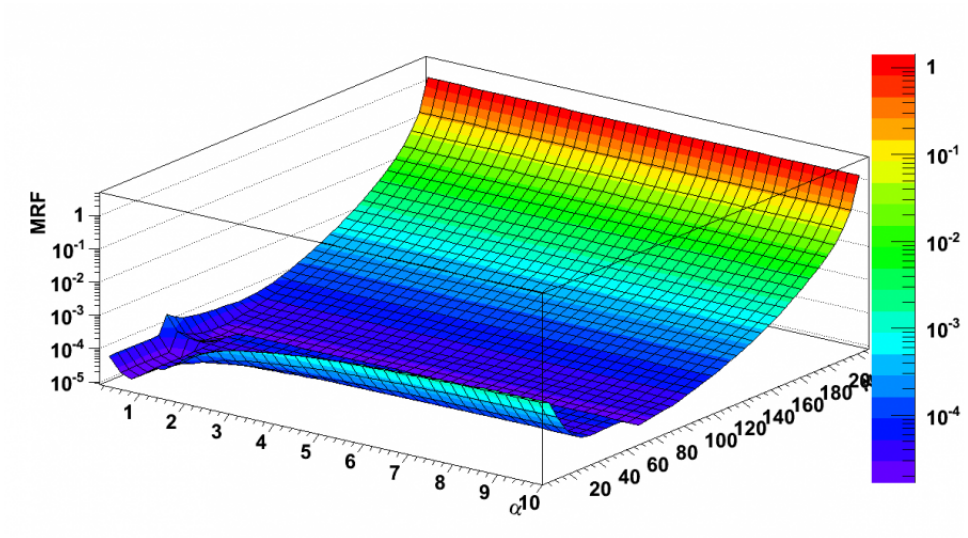

FIGURE 5.8: The Model Rejection Factor as a function of α and N_{hit} cuts. The optimal cut corresponds to the minimal value of MRF. This optimization is obviously performed for each interval of velocity.

One can notice that the MRF displays, as expected, a minimum region, giving rise to a maximisation of the sensitivity. However, this maximisation of sensitivity is not the same for the whole monopole velocity ranges. Thus, the MRF optimisation has been performed for each interval of monopole velocity. Table 5.1 presents the optimal cuts obtained at each range of velocity.

One should mention that the cuts applied on β_{fit} have been applied before the MRF optimisation. They are chosen such as they correspond to the intervals of β_s, so as atmospheric muons and neutrinos with high velocities will be reduced against magnetic monopoles with these specific intervals of β_s. The number of events remaining after the optimization are presented in Table 5.2.

β ranges	α cut	N_{hit} cut	β_{fit} cut
[0.5945 , 0.639]	<5.5	≥36	$]0.5945, 0.639]$
[0.639 , 0.6835]	<5	≥39	$]0.639, 0.6835]$
[0.6835 , 0.728]	<3.4	≥51	$]0.6835, 0.728]$
[0.728 , 0.7725]	<3.3	≥51	$]0.728, 0.7725]$
[0.7725 , 0.817]	<1.8	≥73	$]0.7725, 0.817]$
[0.817 , 0.8615]	<0.8	≥91	none
[0.8615 , 0.906]	<0.6	≥92	none
[0.906 , 0.9505]	<0.6	≥94	none
[0.9505 , 0.995]	<0.6	≥95	none

TABLE 5.1: The optimal cuts on α and N_{hit} obtained for each range of velocity. β_{fit} was reconstructed only for the first 5 ranges.

β ranges	monopoles	muons	neutrinos
[0.5945 , 0.639]	1121	0	0.00016
[0.639 , 0.6835]	15043	0	0.00015
[0.6835 , 0.728]	26300	0	0.00012
[0.728 , 0.7725]	62624	0	0.00928
[0.7725 , 0.817]	114208	0	0.00100
[0.817 , 0.8615]	128444	0	0.17721
[0.8615 , 0.906]	249150	0	0.15641
[0.906 , 0.9505]	330565	0	0.13312
[0.9505 , 0.995]	392010	0	0.12604

TABLE 5.2: MM, muon and neutrino events remaining after the final event selection.

5.3 Uncertainties

In such studies, two types of uncertainties are considered in order to make an analysis with a certain accuracy. Statistical uncertainties are related to the flux of the MC data, whereas Systematic uncertainties are related to the detector efficiency.

5.3.1 Statistical uncertainties

In any similar analysis, the statistical errors should be taken into account. These statistical uncertainties are observed in the distribution of N_{hit} for atmospheric muons where some empty bins are noticed in the region of signal (at high values of N_{hit}). In order to recover this issue, an extrapolation has been performed for the N_{hit} distribution in these regions.

The distribution was fitted as shown in Fig. 5.9, using a Landau type function (red), and then the function was extrapolated to the region of interest (pink). In this region, each bin content is equal to the value given by the Landau function added to the number of muon events given by the histogram.

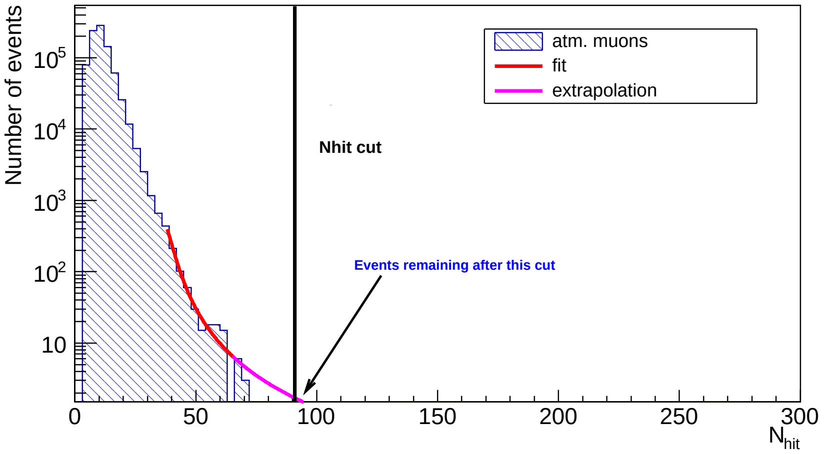

FIGURE 5.9: The distribution of N_{hit} for atmospheric muons, extrapolated using a Landau fit function. The contribution of the extrapolation in the total number of events was taken into account in the optimization and the extrapolation uncertainties were computed. For this bin $\beta = [0.8170, 0.8615]$, 1.4 events are found after the cut $N_{hit} \geqslant 91$.

Further information about Landau function is given in Appendix. B. The errors of the extrapolation rely on the fit parameters and their associated errors. This fit is based on 3 parameters $P1$, $P2$ and $P3$, defining the Landau distribution. For each parameter P we calculate P_+ and P_- defined as: $P_+ = P + dP$ and $P_- = P - dP$, where dP is the error associated to the parameter P.

Table 5.3 presents, for all β_s ranges, P_+ and P_- corresponding to each one of the 3 fit parameters given by the Landau function.

β ranges	$P1_+$	$P2_+$	$P3_+$	$P1_-$	$P2_-$	$P3_-$
[0.5945 , 0.639]	77938.28	22.691059	0.0655252	75168.32	21.869541	0.0330465
[0.639 , 0.6835]	77938.28	22.691059	0.0655252	75168.32	21.869541	0.0330465
[0.6835 , 0.728]	352.2171	34.50491	1.191997	282.2509	26.82049	0.785877
[0.728 , 0.7725]	325366.6	38.70069	0.0291231	302293.4	36.00631	0.0195091
[0.7725 , 0.817]	318.0773	38.97379	1.805932	241.1267	36.77781	1.211808
[0.817 , 0.8615]	2580.038	40.248	1.432946	1218.802	37.644	1.180254
[0.8615 , 0.906]	2580.038	40.248	1.432946	1218.802	37.644	1.180254
[0.906 , 0.9505]	2580.038	40.248	1.432946	1218.802	37.644	1.180254
[0.9505 , 0.995]	2580.038	40.248	1.432946	1218.802	37.644	1.180254

TABLE 5.3: P_+ and P_- corresponding to each one of the 3 fit parameters.

After that, the extrapolation has been performed for 8 combination of parameters in each β range as shown in Table 5.4.

$P1_+$ $P2_+$ $P3_+$
$P1_+$ $P2_+$ $P3_-$
$P1_+$ $P2_-$ $P3_+$
$P1_+$ $P2_-$ $P3_-$
$P1_-$ $P2_+$ $P3_+$
$P1_-$ $P2_+$ $P3_-$
$P1_-$ $P2_-$ $P3_+$
$P1_-$ $P2_-$ $P3_-$

TABLE 5.4: The 8 combination of parameters.

Extrapolation errors

The extrapolation has been made for the 8 combinations of fit parameters presented in Table 5.4. Table 5.1 presents the extrapolation events remaining after cuts, for each combination.

To determine the error on extrapolation, the extreme values are used. For example at $\beta \sim 0.57225$, the values 5.33382 and 3.79083 are taken. The error is then $(5.33382 - 3.79083)/2 = 0.77$. This represent the errors on muon statistics since the extrapolation was performed for muons. These errors are shown in column 3 of Table 5.8.

5.3.2 Systematic uncertainties

In addition to the statistical uncertainties, the uncertainties related to the detector response are also taken into account in some cases. In the current thesis, the extrapolation performed for the expected atmospheric muons is dominant. The related errors grouped in column 3 of Table 5.8 give a sufficient recovery of the expected background events.

β ranges	$P1_+P2_+P3_+$	$P1_+P2_+P3_-$	$P1_+P2_-P3_+$	$P1_+P2_-P3_-$	$P1_-P2_+P3_+$	$P1_-P2_+P3_-$	$P1_-P2_-P3_+$	$P1_-P2_-P3_-$
[0.5945 , 0.639]	2.13254	0.53245	1.87931	0.46961	2.05674	0.51353	1.81252	0.45292
[0.639 , 0.6835]	1.39063	0.34812	1.25479	0.31430	1.3412	0.33575	1.21019	0.30313
[0.6835 , 0.728]	2.37831	1.02097	1.0732	0.45328	1.90587	0.81816	0.86001	0.36324
[0.728 , 0.7725]	1.4816	0.90577	1.34194	0.59861	1.60233	0.84154	1.24678	0.55616
[0.7725 , 0.817]	1.11368	0.48869	0.97774	0.42839	0.84425	0.37047	0.74120	0.32475
[0.817 , 0.8615]	2.42256	1.61911	2.18117	1.45794	1.14441	0.76486	1.03038	0.68872
[0.8615 , 0.906]	2.32539	1.55422	2.09788	1.40233	1.0985	0.73421	0.99103	0.66245
[0.906 , 0.9505]	2.14761	1.43553	1.94485	1.30018	1.01452	0.67814	0.91874	0.61419
[0.9505 , 0.995]	2.06619	1.38118	1.87448	1.2532	0.97606	0.65246	0.88549	0.592

TABLE 5.5: Number of events remaining from the extrapolation, for each one of the 8 combinations of parameters presented in Table 5.4.

However, The effects on the muon and neutrino rates due to the detector uncertainties are widely discussed in [33, 127, 130, 131]. For the atmospheric neutrinos, the systematic uncertainties as a function of the energy are detailed in [130]. As shown in Table 5.8, the contribution of atmospheric neutrinos is almost negligible with respect to atmospheric muons, thus the effects of these uncertainties can be egnored. Concerning atmospheric muons, the dominant detector effects are related to the angular acceptance of the optical module [132] and to the absorption and scattering lengths in water [133]. The maximum ±15% uncertainty on the optical module acceptance and the ±10% on the light absorption length in water over the whole wavelength spectrum yields an overall $^{+35\%}_{-30\%}$ effect on the expected muon rate [33] (see Fig. 5.11 for instance).

5.4 Sensitivity

Using the Feldman-Cousins approach 5.2 and based on the MRF optimisation giving the number of background events remaining, table 5.6 presents the sensitivities found for each interval of velocity.

β ranges	Sensitivity ($cm^{-2} \cdot s^{-1} \cdot sr^{-1}$)
[0.5945 , 0.639]	$5.87 \cdot 10^{-16}$
[0.639 , 0.6835]	$3.65 \cdot 10^{-17}$
[0.6835 , 0.728]	$2.11 \cdot 10^{-17}$
[0.728 , 0.7725]	$9.17 \cdot 10^{-18}$
[0.7725 , 0.817]	$4.47 \cdot 10^{-18}$
[0.817 , 0.8615]	$4.88 \cdot 10^{-18}$
[0.8615 , 0.906]	$2.48 \cdot 10^{-18}$
[0.906 , 0.9505]	$1.83 \cdot 10^{-18}$
[0.9505 , 0.995]	$1.53 \cdot 10^{-18}$

TABLE 5.6: Sensitivities found for each range of β_s.

Fig. 5.10 presents the graph of the sensitivities obtained, compared with other experiments.

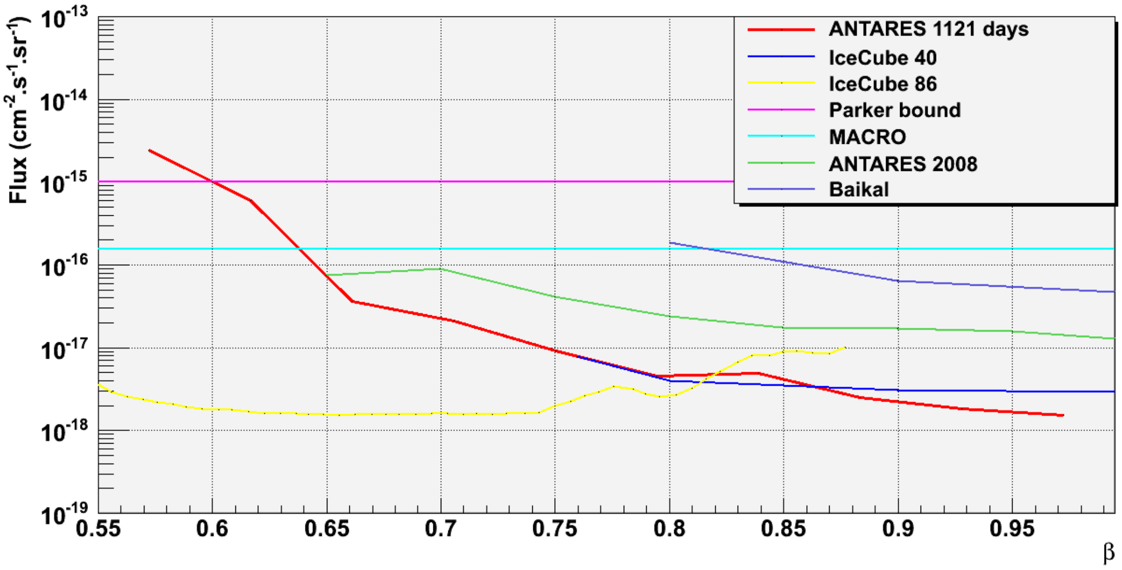

FIGURE 5.10: The sensitivities obtained (red graph) based on the MRF optimisation and calculated using the Feldman-Cousins tables for a number of background events remaining. For comparison, other limits on flux found by some experiments have been presented, including the ANTARES result of 2008.

The sensitivities obtained show a good result at high velocity ranges where there are minimum values. After unblinding, i.e using the same optimized cuts and taking into consideration the full collection of real data, the final limits on flux will be calculated. Before that, a comparison between data and MC distributions is useful to assess the analysis.

5.5 Data/MC comparison

A sample of 10% of runs with numbers ending with 0 (0-runs) have been taken to do the comparison and to take care of the agreement MC/data.

Fig. 5.11 and Fig. 5.12 show that real data are dominated by atmospheric background. Taking into account an uncertainty band around the atmospheric muon flux, the data/MC agreement oberved explains the accuracy of the performed simulation.

5.6 Limits on flux

The 90% confidence level interval $\mu_{90}(n_b, n_{obs})$ shown in Eq. (5.2.3), will be used instead of $\bar{\mu}_{90}$ to calculate the final limits on flux. It depends on the number of

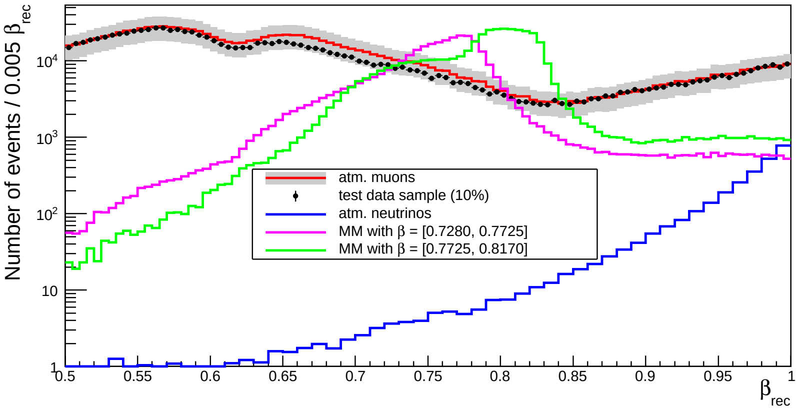

FIGURE 5.11: Distribution of the reconstructed β_{fit} for atmospheric muons (red histogram) with an uncertainty band of 35% (filled in gray), atmospheric neutrinos (blue histogram) and data (points with error bars). For comparison, the distributions of the reconstructed β_{fit} for MMs simulated in the velocity ranges $[0.7280, 0.7725]$ (magenta histogram) and $[0.7725, 0.8170]$ (green histogram) are also shown. All distributions correspond to events reconstructed as up-going.

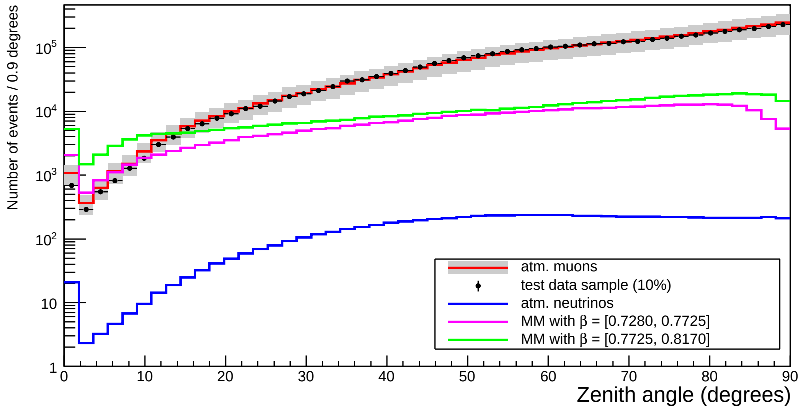

FIGURE 5.12: Distribution of zenith angle for atmospheric muons (red histogram) with an uncertainty band of 35% (filled in gray), atmospheric neutrinos (blue histogram) and data (points with error bars). For comparison, the distributions of the reconstructed β_{fit} for MMs simulated in the velocity ranges $[0.7280, 0.7725]$ (magenta histogram) and $[0.7725, 0.8170]$ (green histogram) are also shown. All distributions correspond to events reconstructed as up-going.

observed events in addition to the number of background events. The limit on flux will be then defined as :

$$\Phi_{90\%}(cm^{-2} \cdot s^{-1} \cdot sr^{-1}) = \frac{\mu_{90}}{S_{eff} \times T(s)}, \tag{5.6}$$

After unblinding, the optimal cuts have been applied on the total set of data collected by the ANTARES telescope during five years, which corresponds to 1012 active days live time after subtracting the 10% burn sample. In the first five bins, a different interval of β_{fit} has been applied in each bin in such a way that the interval of β_{fit} should be compatible to the interval of simulated velocity of magnetic monopoles β_s. Therefore, the event samples in these ranges are exclusive and must be added. However, in the last four bins no cuts have been applied on β_{fit} which is not reconstructed in this region ($\beta_{fit} = 1$), thus bin 7 is a subset of bin 6 for example, and the number of events remaining is given here by bin 6 already.

Two events survived the final cuts, the first one corresponds to $\beta_s \approx 0.75025$, and the second has $\beta_s \geq 0.83925$. Table 5.7 shows the number of events remaining for each range of β_s.

β_s ranges	Events remaining
[0.5945 , 0.639]	0
[0.639 , 0.6835]	0
[0.6835 , 0.728]	0
[0.728 , 0.7725]	1
[0.7725 , 0.817]	0
[0.817 , 0.8615]	1
[0.8615 , 0.906]	1
[0.906 , 0.9505]	0
[0.9505 , 0.995]	0

TABLE 5.7: The real events remaining for each range of β_s.

The first event has N_{hit} = 93, α = 0.5 and zenith = 27.4° and passes the cuts optimized of two bins of β. It is identified as a bright well-reconstructed neutrino event regarding its physical properties, compatible with the total background observed at this range of high velocities. The second event with $\beta \geq 0.728$ is consistent with a down-going (zenith = 108.1°) atmospheric muon yielding a bright shower. Fig. 5.13 shows the event displays of these two events.

A summary of the optimal cuts applied and the number of expected background and observed events as well as the 90% C.L. upper limits on the MM flux for each bin of β_s is given in Table 5.8.

No significant excess of data events is observed over the expected background. The sum of background events in the first five ranges adds up to 5.4 events whereas only one event has been observed. This indicates a rather conservative method of extrapolating the atmospheric muon sample into the region defined by the final cuts. The upper limits on flux have been found using Eq. (5.6) [134] and represented by the red graph in Fig. 5.14.

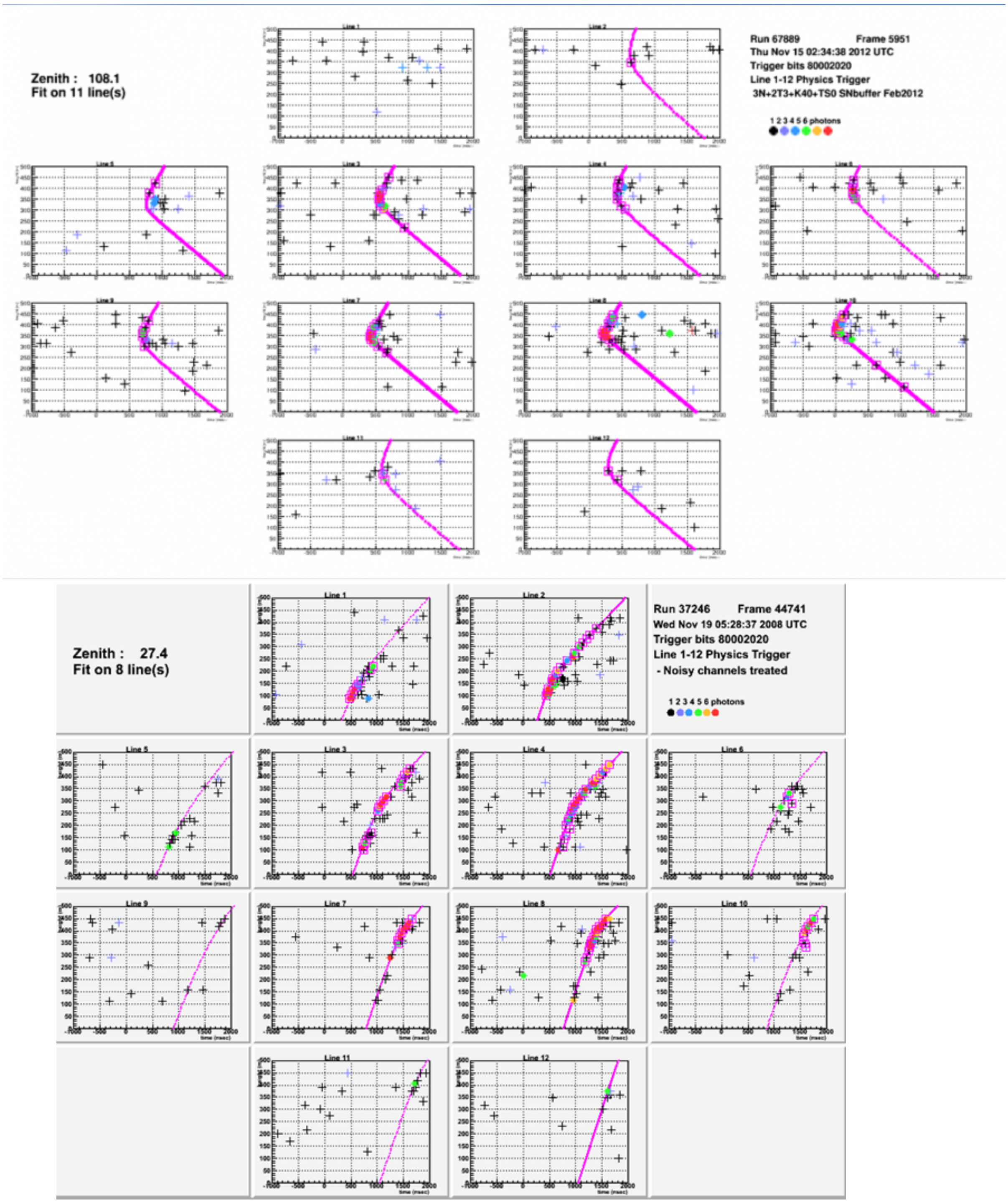

FIGURE 5.13: The event displays for the two observed events.

β range	Selection cuts		Number of atm. muons	Number of atm. neutrinos	Number of obs. events	Flux Upper Limits 90% C.L. ($\mathrm{cm}^{-2}\cdot\,\mathrm{s}^{-1}\cdot\,\mathrm{sr}^{-1}$)
	α	N_{hit}				
[0.5945, 0.6390]	< 5.5	$\geqslant 36$	1.9 ± 0.8	1.6×10^{-4}	0	5.9×10^{-16}
[0.6390, 0.6835]	< 5.0	$\geqslant 39$	0.9 ± 0.5	1.5×10^{-4}	0	3.6×10^{-17}
[0.6835, 0.7280]	< 3.4	$\geqslant 51$	0.9 ± 1.0	1.2×10^{-4}	0	2.1×10^{-17}
[0.7280, 0.7725]	< 3.3	$\geqslant 51$	1.1 ± 0.5	9.3×10^{-3}	1	9.1×10^{-18}
[0.7725, 0.8170]	< 1.8	$\geqslant 73$	0.6 ± 0.4	1.0×10^{-3}	0	4.5×10^{-18}
[0.8170, 0.8615]	< 0.8	$\geqslant 91$	1.4 ± 0.9	1.8×10^{-1}	1	4.9×10^{-18}
[0.8615, 0.9060]	< 0.6	$\geqslant 92$	1.3 ± 0.8	1.6×10^{-1}		2.5×10^{-18}
[0.9060, 0.9505]	< 0.6	$\geqslant 94$	1.2 ± 0.8	1.3×10^{-1}	0	1.8×10^{-18}
[0.9505, 0.9950]	< 0.6	$\geqslant 95$	1.2 ± 0.7	1.3×10^{-1}	0	1.5×10^{-18}

TABLE 5.8: Results after unblinding of the data (1012 active days live time corresponding to 5 years of data taking) [134]. The selection cuts, the number of expected (muons and neutrinos) background and observed events and the upper limits on the flux are presented for each range of velocity (β). The table was divided into two parts to distinguish the first five bins where β_{fit} was assumed as a free parameter from the four bins where $\beta_{fit} = 1$.

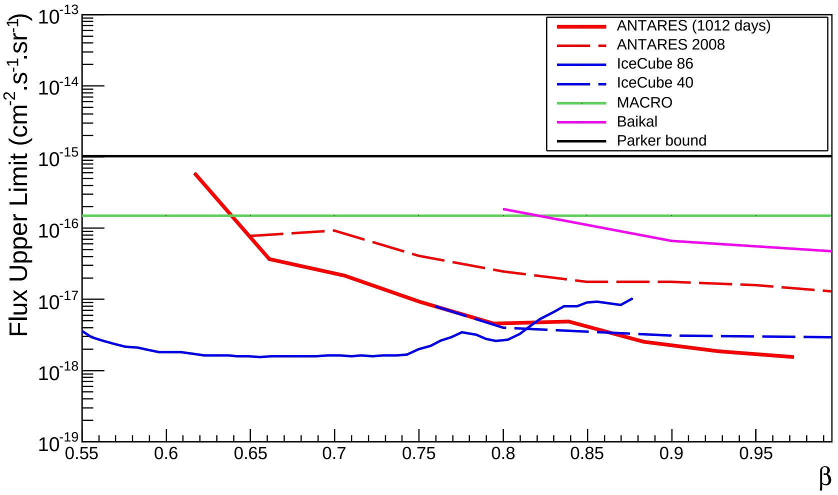

FIGURE 5.14: ANTARES 90% C.L. upper limit on flux for MMs using five years of data with 1012 active days live time (solid red line) [134], compared to the upper limits obtained by other experiments [9, 72, 135], as well as the previous analysis of ANTARES (dashed red line) [8] and the theoretical Parker bound [69]. In [9] a more optimistic model for δ-rays production of MMs is used, making a direct comparison difficult.

In Fig. 5.14 the ANTARES upper limits as a function of β are presented, together with other experimental results from IceCube [9], MACRO [72] and Baikal [135], as well as the previous result from ANTARES [8] and the theoretical Parker bound [69].

5.7 Conclusion

New limits on magnetic monopole flux have been obtained using 1012 active days of ANTARES data. The analysis was performed with Monte Carlo data assuming a blind policy, then a test data sample has been used to make a comparison with the simulation giving rise to a good agreement data/MC. It turned out that the two events observed after applying the final cuts do not exceed the atmospheric background expectation.

Summary and conclusion

Grand Unification Theories predict that the universe underwent phase transitions due to temperature decrease caused by the expansion. During these phase transitions, stable entities called topological defects have been created. Among these topological defects, there could be a class, having all the characteristics of an exotic particle that can be observed in the detectors of cosmic particles. The so-called magnetic monopoles carrying a single magnetic charge are predicted by many gauge theories and proposed by Dirac since 1931.The existence of magnetic monopoles leads to a perfect symmetry of electromagnetisme theory. In addition, it would explain the quantization of electric charges.

Magnetic monopoles should have survived to this day, but major constraints on their flux have been posed, including the theoretical constraint of Parker, which requires a flux less than $10^{-15} cm^{-2} \cdot s^{-1} \cdot sr^{-1}$ so that the galactic magnetic field can regenerate. Though, they could be accelerated by Galactic magnetic fields into relativistic speeds. With sufficiently high energies, they would cross the earth and emit a significant signal in a neutrino detector. With one or more magnetic charges, according to the model predicting them, monopoles crossing a medium, will emit an electric field that is perpendicular to their direction. like electrically charged particles, monopoles will then be able to emit Cherenkov light if their speed allows them, with an intensity 8500 times higher than a muon of the same speed. In addition to being detectable by direct Cherenkov emission, a monopole could emit indirect Cherenkov light from electrons extracted from their atoms during its passage, even for velocities below Cherenkov threshold ($\beta \approx 0.74$ in sea water), greater than $\beta \approx 0.50$.

This thesis shows the sensitivity offered by the ANTARES neutrino telescope to search for magnetic monopoles. For this study, 5 years of the ANTARES detector data have been used corresponding to 1121 active days of livetime. The reconstruction algorithm BBfit was employed to reconstruct tracks crossing the detector with the speed of light. Then it was modified to implement β as a free parameter in order to distinguish monopoles with low velocities from other particles. This was based on the run-by-run Monte Carlo simulation which takes into account the real data taking environmental conditions in water.

After the optimisation performed with Monte Carlo data, a sample of real data have been taken and compared to Monte Carlo distributions, leading to more restrictive cuts to get a fair agreement between real and Monte Carlo data, and finally allowing to do the last optimization using cuts on the quantity of detected light merged with the track fit quality parameter in order to obtain the best expected sensitivity.

No significant excess has been observed beyond the atmospheric background expected, leading to find new upper limits on flux. The limits found present a competitive result, especially at high velocities ($\beta \geq 0.74$) where ANTARES provides the best sensitivity compared to other neutrino experiments. The fluctuation of the limit at low speeds is due to the model of cross section used (Mott) which describes the interaction of magnetic monopoles with electrons in sea water below Cherenkov radiation. This model is more conservative in terms of the amount of light emitted by δ-rays leading to a minimisation of systematic uncertainties. Nevertheless, this amount of light is not enough to get the best sensitivity at these regions of low speeds. However, a different model (KYG) that was used by IceCube in their analysis is being implemented to perform a new simulation of magnetic monopoles for future analyses. The larger amount of light provided by the "KYG" model will certainly lead to get better limits on flux. This model is discussed in App. A.

As mentioned earlier, the ANTARES collaboration is developing the new neutrino telescope KM3NeT [17] that will have a larger volume and a high detection performance. A short description of the KM3NeT telescope is given in App. C. This new project will certainly improve the search for magnetic monopoles and contribute to the development of knowledge in astrophysics and neutrino physics.

Appendix A

Monopole interaction cross section

The interaction cross section gives the probability for Coulomb scattering of an atomic electron in the field of a monopole. The cross section depends on the transition matrix M_{fi} [136] from an initial ψ_i to a final ψ_f state.

Usually the interaction cross section is given in a differential form $d\sigma/d\Omega$. $d\Omega$ is defined to be the flux of particles in state ψ_f scattered into the space angle $d\Omega$ per unit time, divided by the flux density of the initial wave ψ_f. Additionally, cross sections are often shown as a form factor F which is defined as the ratio to the Rutherford cross section σ_R described in the next section

$$F = \frac{\sigma}{\sigma_R} \tag{A.1}$$

or corresponding differential forms.

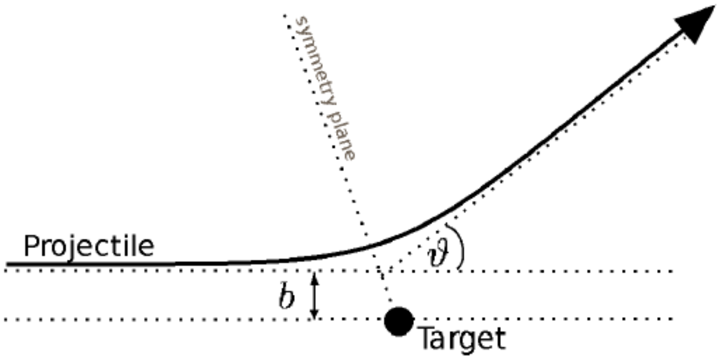

FIGURE A.1: Coloumb scattering of an electron off a heavy electric charge or a magnetic monopole where b is the impact parameter and θ is the scattering angle. The impact parameter is defined as the perpendicular distance from the target to the direction of the incident particle if there were no interactions between them.

A.1 Rutherford cross section

The Rutherford cross section σ_R assumes an elastic scattering where:

- both particles are point-like, have no spins and no magnetic moment
- the incoming particle is not relativistic

- the recoil of the target is negligible

For an electric charge scattering off a target, which is a comparably heavy electric charge, the Rutherford cross section [137] is

$$(\frac{d\sigma}{d\Omega})_R = (\frac{Z'e \cdot Ze}{4T_0})^2 \frac{1}{\sin^4 \frac{\theta}{2}}, \tag{A.2}$$

where θ is the scattering angle (see definition in Fig. A.1), $Z'e$ is the charge of the incident particle ($Z' = 1$ for electrons), and T_0 is the kinetic energy of the projectile before the scattering.

A.2 Mott cross section

Differing from the Rutherford cross section, the Mott cross section assumes an elastic scattering where:

- the incoming particle has a relativistic velocity
- the electron has the spin $\frac{1}{2}$ and magnetic moment; the monopole target has no spin
- the recoil of the target is taken into account

The result is the modification of the Rutherford cross section with the form factor [81, 82]

$$F_M(\beta) = 1 - \beta^2 \sin^4 \frac{\theta}{2}. \tag{A.3}$$

To show the cross section in dependence of the final electron energy T, the following approximation for the scattering angle is used [81]

$$\sin^4 \frac{\theta}{2} \approx \frac{T}{T_{max}}, \tag{A.4}$$

where T_{max} is the maximum energy transfer between monopole and electron [138] which is illustrated in Fig. A.2

A.3 KYG cross section

To be consistent with both quantum mechanics and special relativity, the so-called KYG cross section [85] was introduced, taking into account (additionally to the Mott cross section):

- helicity flip and non-flip amplitudes of the cross section for relativistic velocities taking the spin into account[1]
- the vector potential $\vec{A}$ (in opposite to the magneto static way before)

The KYG form factor is

$$F_K = (\frac{g\beta}{Ze})^2 [\frac{T^2}{(Zeg)^2} \sin^4 \frac{\theta}{2} + 2(\sin \frac{\theta}{2})^{4Zeg+2}], \tag{A.5}$$

---

[1] The helicity is defined as the projection of the spin onto the direction of the momentum.

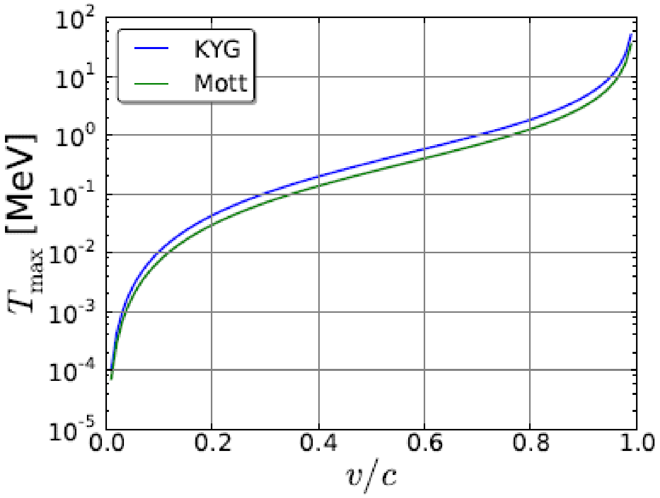

FIGURE A.2: Maximum energy T_{max} transferred between monopole and electron using the correction factor for Mott, taken from [51].

The form factor is given as tabulated values in [85].

A future analysis will be performed in ANTARES using KYG model since it is most advanced, fully respecting electro-dynamics, quantum mechanics, and special relativity. For this purpose, a new simulation of magnetic monopoles is being performed. The angular distribution presented in 3.10 has been restablished for KYG as shown in Fig. A.3.

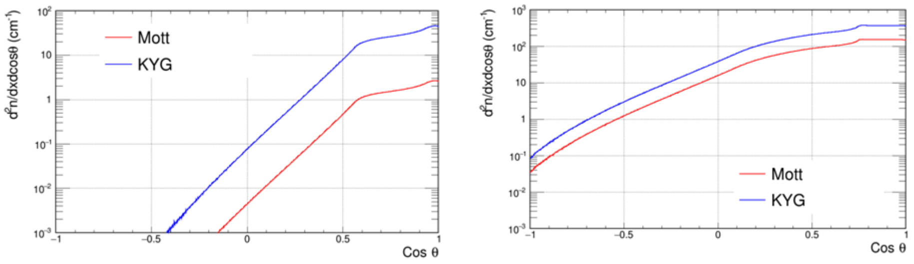

FIGURE A.3: The angular distribution for monopoles simulated with $\beta = 0.60$ (left) and $\beta = 0.95$ (right). A comparison with Mott is shown.

At high velocities (above Cherenkov threshold), Cherenkov light is emmitted directly and the models of cross sections do not really matter, while at lower velocities δ-electrons yield the total light. The difference between the two models can be easily observed in A.3. The simulation based on this new model is presented in terms of N_{hit} as an example (see Fig. A.4).

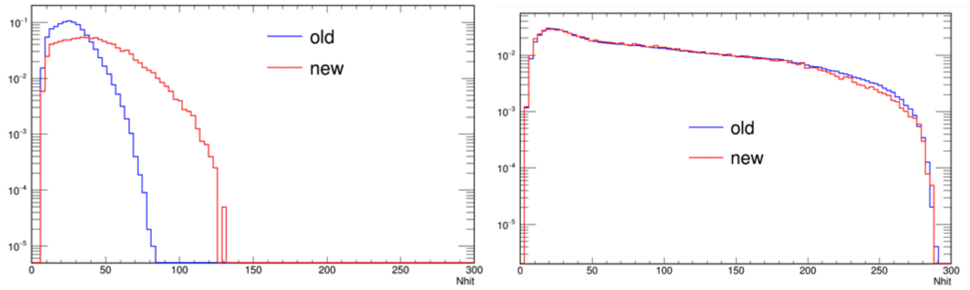

FIGURE A.4: N_{hit} distribution for monopoles with a low velocity interval (left) and a high interval (right). A comparison with the old simulation based on Mott is performed.

The new simulation based on KYG will allow to improve the sensitivity for monopoles and get the best upper limit on flux in the future analysis, since it provides more light yield which is a very important discriminative variable.

Appendix B

Landau distribution

It is well known that the Bethe-Bloch formula [87, 139] describes the average energy loss of charged particles when travelling through matter. The fluctuations of energy loss by ionization of a charged particle in a thin layer of matter was theoretically described by Landau [140].

This description ends with a universal asymmetric probability density function characterized by a narrow peak with a long tail for positive values B.1. This tail towards positive values comes from the small number of individual collisions, each with a small probability of transferring comparatively large amounts of energy. An integral representation of the Landau probability density function reads

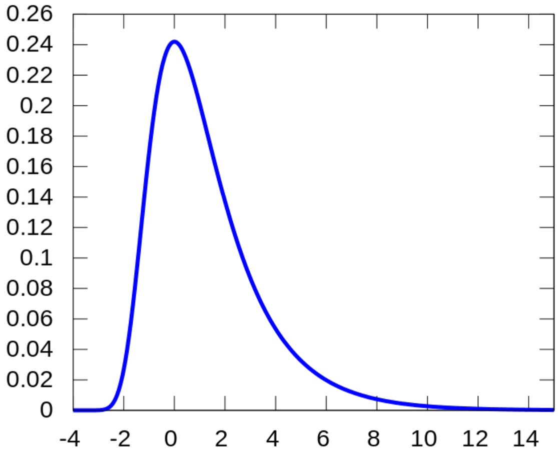

FIGURE B.1: The probability Density Function called Landau distribution.

$$\phi(c) = \frac{1}{\pi}\int_0^\infty x^{-x}\sin(\pi x)\exp(-cx)dx. \tag{B.1}$$

The N_{hit} distribution used in this analysis stands for the number of storeys that detected light from an event, i.e it refers to the total amount of light emitted by this event. The number of photons emitted by a muon track is related to the energy loss in the medium.

Under this assumption, the use of Landau distribution in Fig. 5.9 fits exactly the distribution of N_{hit} for muons.

Appendix C

KM3NeT: The future neutrino telescope

KM3NeT [17] is a research infrastructure housing the next generation neutrino telescopes. Once completed, the telescopes will have detector volumes between megaton and several cubic kilometres of clear sea water. Located in the deepest seas of the Mediterranean, KM3NeT will open a new window on our Universe, but also contribute to the research of the properties of the elusive neutrino particles. With the ARCA telescope, KM3NeT scientists will search for neutrinos from distant astrophysical sources such as supernovae, gamma ray bursters or colliding stars. The ORCA telescope is the instrument for KM3NeT scientists studying neutrino properties exploiting neutrinos generated in the Earth's atmosphere. Arrays of thousands of optical sensors will detect the faint light in the deep sea from charged particles originating from collisions of the neutrinos and the Earth. The facility will also house instrumentation for Earth and Sea sciences for long-term and on-line monitoring of the deep sea environment and the sea bottom at depth of several kilometers.

C.1 The collaboration

The collaboration includes about 240 people from more than 45 institutes or universities from 15 different countries.

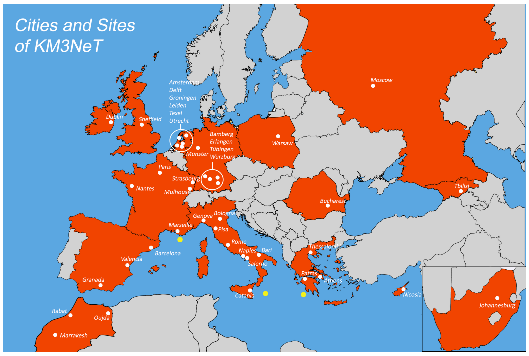

FIGURE C.1: The map of KM3NeT cities and sites.

Morocco takes part of this collaboration and it is presented by three universities; Mohammed I University in Oujda, Mohammed V University in Rabat and Cadi Ayyad University in Marrakech.

C.2 Detector design

Construction of KM3NeT began in 2015, with 240 scientists in 15 different countries embarking on the latest deep-sea adventure. On completion in the early 2020s it will have 345 detection lines distributed across two sites in the Mediterranean Sea: one near Toulon, close by ANTARES, and a second one off the coast of Capo Passero in Sicily, Italy, creating a telescope with a detection volume of more than $1km^3$. While neutrino detection in KM3NeT will still be reliant on the Cherenkov principle, the new project features significant technological improvements based on the decade-long experience of ANTARES and the other prototypes. In particular, 31 small photomultipliers, instead of a single, larger one, will be housed in each glass sphere offering several advantages in terms of photon detection efficiency, photon counting and directionality all of which are crucial ingredients for the reconstruction of the incoming neutrino energy and arrival direction. The deployment procedure has also been redesigned: the full detection line is coiled into a spherical frame and attached to a line anchor, which in turn is equipped with an acoustic receiver. Researchers can acoustically monitor the descent of the detection unit from a surface vessel, allowing lines to be positioned to within 1 m. And there's no need any more for courageous divers as the anchor is connected to the seabed network by a submarine vehicle remotely operated from the boat. Once the connection is verified onshore, an acoustic signal triggers the unfurling of the unit. The compact line frames also mean several lines can be deployed during a single cruise, saving time and money. Although both detection sites will be based on the same technology, the two will pursue different physics goals. In Toulon, the emphasis will be on studying atmospheric neutrino properties in the GeV energy range, with a dense detector named Oscillation Research with Cosmics in the Abyss (ORCA). In Sicily, a larger and sparser detector called Astrophysics Research with Cosmics in the Abyss (ARCA) will focus on the study of astrophysical sources with energies ranging from TeV to PeV. At each site, the first lines of the arrays have been installed and the first background events have been observed. Physicists working on the construction of KM3NeT are eager to share their data and provide new opportunities for earth and sea sciences through their cabled infrastructure. From oceanography to geophysics and from marine biology

FIGURE C.2: Photograph of the digital optical module.

to climatology, the full scientific potential of deep-sea neutrino observatories is still to be explored. As a partner of the European Multidisciplinary Seafloor and water column Observatory facility, KM3NeT will help scientists understand the complex interaction between the geosphere, the biosphere and the hydrosphere, while continuing to hunt for cosmic neutrinos (see box below).

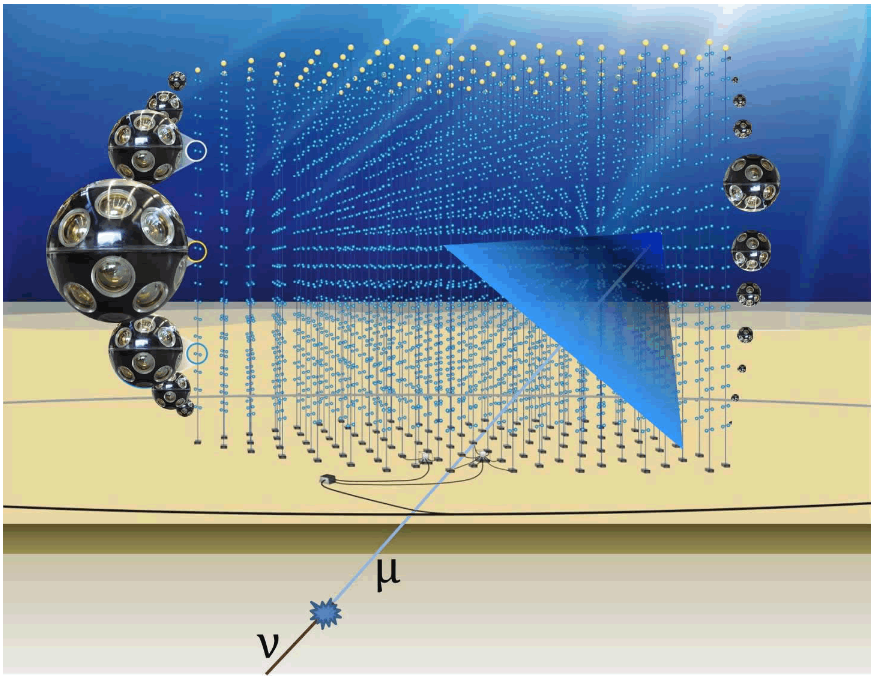

FIGURE C.3: Illustration of the whole km3net telescope.

C.2.1 Purposes of ORCA

ORCA is an underwater Cherenkov neutrino detector, planned to be part of the distributed KM3NeT infrastructure. It will be devoted to the study of the fundamental properties of neutrinos, exploiting the abundant flux of neutrinos produced in the interactions of cosmic rays with the atmosphere.

The atmospheric flux of neutrinos has traditionally been considered as background noise for the detection of an astrophysical neutrino signal. In recent years, however, it has been realized that in the few GeV band, this flux holds the key to solving a fundamental question of particle physics: that of the mass hierarchy of neutrinos, i.e if the eigenvalue ν_3 of the mass is heavier (normal hierarchy) or lighter (reversed hierarchy) than the states ν_2 and ν_1. The influence of the mass hierarchy on the neutrino oscillations in matter leaves its imprint on the flux of atmospheric neutrinos via the characteristic aspect of the appearance / disappearance of the various types of neutrinos according to the energy and the path crossed through the earth.

To perform this measurement, ORCA provides the instrumentation of a multi-megaton scale array of optical modules based on KM3NeT technology and optimized for the study of the interactions between atmospheric neutrinos in the sea. The optical modules will be arranged in a dense configuration, with an energy threshold of the order of GeV, three orders of magnitude lower than the standard energy scale tested by ARCA for neutrino astronomy. To be deployed at the French

KM3NeT site, ORCA's multi-PMT optical modules will take advantage of the excellent optical properties of deep seawater to achieve the angular and energy resolutions needed to illuminate the neutrino mass hierarchy.

Phase 1 of KM3NeT provides for the deployment and operation of a prototype ORCA array, consisting of 7 detection lines with a 20 m line spacing, in the next two years. If funds permit, the full ORCA detector, consisting of a KM3NeT building block (115 lines of detection), could be operational by the end of the decade, offering new possibilities for oscillation studies of neutrinos in the Mediterranean, complementary to reactor and beam experiments.

Bibliography

[1] A.H. Guth and E.J. Weinberg, *Could the Universe Have Recovered from a Slow First-Order Phase Transition?*, *Nuclear Physics* **B 212** (1983) 321.

[2] J.H. Christenson, J.W. Cronin, V.L. Fitch, R. Turlay (Princeton U.), *Evidence for the 2pi Decay of the K Meson*, *Physical Review Letters* **13** (1964) 138-140.

[3] N. D. Mermin, *The topological theory of defects in ordered media*, *Reviews of Modern Physics* **51** 591 – Published 1 July 1979.

[4] G. 't Hooft, *Magnetic monopoles in unified gauge theories*, *Nuclear Physics* **B 79** (1974) 276.

[5] A.M. Polyakov, *Particle Spectrum in the Quantum Field Theory*, *Soviet Physics JETP Letters* **20** (1974) 194.

[6] P. Niessen, *Search for Relativistic Magnetic Monopoles with the AMANDA Detector*. Ph.D. Thesis, Humboldt-Universität, Berlin, 2001.

[7] G. Aad et al., *Search for magnetic monopoles and stable particles with high electric charges in 8 TeV pp collisions with the ATLAS detector*, *Physical Reviews* **D 93** (2016) 052009.

[8] S. Adrian-Martinez et al., *Search for Relativistic Magnetic Monopoles with the ANTARES Neutrino Telescope*, *Astroparticle Physics* **35** (2012) 634.

[9] M.G. Aartsen et al., *Searches for Relativistic Magnetic Monopoles in IceCube*, *EPJ* **C76** (2016) 133.

[10] W. Hofmann et al., *Status of the High Energy Stereoscopic System (H.E.S.S.) Project*, the ICRC 2001 proceedings.

[11] Aab, A. et al., *Nuclear Instruments and Methods in Physics Research Section A* **798**, (2015) 172.

[12] Aartsen, M. G. et al. (2016), arXiv:1612.06028.

[13] M. Ageron et al., *ANTARES: the first undersea neutrino telescope*, *Nuclear Instruments and Methods* **A656** (2011) 11.

[14] Aasi J., et al., *Classical and Quantum Gravity* **32**, (2015) 074001.

[15] Acernese, F., et al., *Classical and Quantum Gravity* **32**, (2015) 024001.

[16] Abbott et al., *Physical Review Letters* **119**, (2017) 161101.

[17] S. Adrian-Martinez et al., *Letter of intent for KM3NeT 2.0.*, *Journal of Physics* **G43(8)** (2016) 084001.

[18] E. Fermi, *Zeitschrift für Physik* **88** (1934) 161–177.

[19] A. Yu. Smirnov, *The MSW effect and Solar Neutrinos*, arXiv:hep-ph/0305106, 2003.

[20] http://www-sk.icrr.u-tokyo.ac.jp/sk/pub/d.pdf

[21] G. Giacomelli, M. Giorgini, hep-ex/0110021.

[22] Soudan-2 coll., *19th International Conference on Neutrino Physics and Astrophysics - Neutrino 2000, Sudbury, Ontario, Canada*, *Nuclear Physics Poc. Suppl.* **91**, 16-21 June 2000, 134-140.

[23] P. A. Cherenkov, *Doklady Akademii Nauk SSSR* **Vol. 2** (1934), 451.

[24] L.A. Kuzmichev, *On the Velocity of Light Signals in Deep Underwater Neutrino Experiments*, *Nuclear Instruments and Methods* **A 482**, (2002) 304.

[25] D.J.L. Bailey, *Monte Carlo Tools and Analysis Methods for Understanding the ANTARES Experiment and Predicting Its Sensitivity to Dark Matter*, Ph.D. Thesis, Wolfson College, Oxford, 2002.

[26] J.A. Aguilar et al., *The data acquisition system for the ANTARES neutrino telescope*, *Nuclear Instruments and Methods* **A 570** (2007) 107.

[27] M. Amram et al., *The ANTARES optical module*, *Nuclear Instruments and Methods* **A484** (2002) 369-383.

[28] M. Ageron et al., ANTARES Collaboration, astro-ph/0703355 (2007).

[29] N.P. Clemente, Ph.D. Thesis, Université de la Méditérranée - AixMarseille II, France (2010).
http://www.theses.fr/2010AIX22084.

[30] D. Lachartre et F. Feinstein, *Application specific integrated circuits for ANTARES offshore frontend electronics*, *Nuclear Instruments and Methods* **A442** (2000) 99-104.

[31] F. Druillole et al., *The analoge ring sampler : An ASIC for the front-end electronics of the ANTARES neutrino telescope*, *IEEE Transactions on Nuclear Science* **49** (2002) 1122-1129.

[32] J.A.Aguilar, et al., *Astroparticle Physics* **34** (2011) 539, arXiv:1012.2204.

[33] J.A. Aguilar et al., *Zenith distribution and flux of atmospheric muons measured with the 5-line ANTARES detector*, *Astroparticle Physics* **34** (2010) 179.

[34] M. Ageron et al. (ANTARES Collaboration) *Astroparticle Physics* **31** (2009) 277.

[35] Aguilar J.A., et al. *Astroparticle Physics* **33** (2010) 86-90.

[36] E. V. Bugaev et al. *Physical Review* **D58** (1998) 05401.

[37] E. Andres et al., (AMANDA Collaboration) *Astroparticle Physics* **13** (2000) 1.

[38] P. Desiati for AMANDA Collaboration *Proc. of the 28th ICRC, Tsukuba*, (2003).

[39] I. A. Belolaptikov et al., (Baikal Collaboration) *Astroparticle Physics* **7** (1997) 263.

[40] J. Babson et al., (DUMAND Collaboration) *Physical Review* **D42** (1990) 41.

[41] G. Aggouras et al., (NESTOR Collaboration) *Astroparticle Physics* **23** (2005) 377.

[42] S. Aiello et al., (NEMO Collaboration) *Astroparticle Physics* **33** (2010) 263.

[43] A. G. Dickson and C. Goyet (eds.), *Handbook of Methods for the Analysis of the Various Parameters of the Carbon Dioxide System in Sea Water*, version 2, DOE (1994), ORNL/CDIAC-74, http ://andrew.ucsd.edu/co2qchandbook/0content.pdf

[44] G. Audi et al. *The NUBASE Evaluation of Nuclear and Decay Properties, Nuclear Physics* **A 729** (2003) 3.

[45] J. Brunner, *Simulation of 40K Signals internal note Site/1999-002*, (ANTARES Collaboration) (1999).

[46] Jun S. Song, *Undergraduate Journal of Science* **3**, (1996) 47-55.

[47] P.A.M. Dirac, *Quantized Singularities in the Electromagnetic Field, Proceedings of the Royal Society* **A 133** (1931) 60.

[48] D.A. Kirzhnits, *Weinberg Model and The ḦotÜniverse, JETP Letters* **15**, (1972) 529.

[49] T.W.B. Kibble, *Topology of Cosmic Domains and Strings, Journal of Physics* **A 9**, (1976) 1387.

[50] J.P. Preskill, *Cosmological Production of Superheavy Magnetic Monopoles, Physical Review Letters* **43**, (1979) 1365.

[51] A.M. Pollmann, *Search for mildly relativistic Magnetic Monopoles with IceCube*, Ph.D Thesis, BERGISCHE UNIVERSITÄT WUPPERTAL, November 2015.

[52] M.S. Turner, E.N. Parker and T.J. Bogdan, *Magnetic Monopoles and the Survival of Galactic Magnetic Fields, Physical Review* **D 26**, (1982) 1296.

[53] G. Giacomelli, *Magnetic Monopoles, La Rivista del Nuovo Cimento* **7**, (1984) 1.

[54] S. Weinberg, *The Quantum Theory of Fields, Volume II: Modern Applications*, Cambridge University Press, 1996.

[55] H. Georgi, H.R. Quinn and S. Weinberg, *Hierarchy of Interactions in Unified Gauge Theories, Physical Review Letters* **33**, (1974) 451.

[56] M. Daniel, G. Lazarides and Q. Shafi, *SU(5) Monopoles, Magnetic Symmetry and Confinement, Nuclear Physics* **B 170**, (1980) 156.

[57] T.W. Kephart and T.J. Weiler, *Magnetic Monopoles as the Highest Energy Cosmic Ray Primaries, Astroparticle Physics* **4**, (1996) 271.

[58] P.H. Frampton and B.H. Lee, *SU(15) Grand Unification, Physical Review Letters* **64**, (1990) 619.

[59] P.H. Frampton and T.W. Kephart, *Higgs Sector and Proton Decay in SU(15) Grand Unification, Physical Review* **D 42**, (1990) 3892.

[60] S.F. King and Q. Shafi, *Minimal Supersymmetric* $SU(4) \times SU(2)_L \times SU(2)_R$, *Physics Letters* **B 422**, (1998) 135.

[61] T.W. Kephart and Q. Shafi, *Family Unification, Exotic States and Magnetic Monopoles*, May 2001. hep-ph/0105237.

[62] K.R. Dienes, E. Dudas, T. Gherghetta, *Physics Letters* **B436**, (1998) 55.

[63] I. Antoniadis, N. Arkani-Hamed, S. Dimopoulos, G. Dvali, *Physics Letters* **B436**, (1998) 257.

[64] St.D. Wick et al. *Astroparticle Physics* **18**, (2003) 663.

[65] E. Huguet and P. Peter, *Bound States in Monopoles: Sources for UHECR*, *Astroparticle Physics* **12**, (2000) 277.

[66] S.D. Wick, T.W. Kephart, T.J. Weiler and P.L. Biermann, *Signatures for a Cosmic Flux of Magnetic Monopoles*, (April 2000) astro-ph/0001233.

[67] E.W. Kolb and M.S. Turner, *The Early Universe, in Frontiers in Physics*, *Perseus Publishing*, (1990).

[68] D. Ryu et al., *Cosmic magnetic fields in large scale filaments and sheets*, *Astronomy and Astrophysics* **335** (1998) 19.

[69] E.N. Parker, *The Origin of Magnetic Fields*, *Astrophysics Journal* **160** (1970) 383.

[70] C. Patrignani et al. (Particle Data Group), *listing on Searches for Magnetic Monopoles*, *Chinese Physics C* **40**, (2016) 100001.

[71] L. Patrizii and M. Spurio, *Status of Searches for Magnetic Monopoles*, *Annual Review of Nuclear and Particle Science* **65** (2015) 279.

[72] M. Ambrosio et al., *Final Results of Magnetic Monopole Searches with the MACRO Experiment*, (July 2002) hep-ex/0207020.

[73] S. Orito et al., *Search for Supermassive Relics with a* $2000 - m^2$ *Array of Plastic Track Detectors*, *Physical Review Letters* **66**, (1991) 1951.

[74] V.A. Balkanov et al., *The Lake Baikal Neutrino Experiment*, *Physics of Atomic Nuclei* **66**, (2003) 503.

[75] J. Bartelt et al., *Monopole-Flux and Proton-Decay Limits from the Soudan 1 Detector*, *Physical Review* **D 36**, (1987) 1990.

[76] R. Becker-Szendy et al., *New Magnetic Monopole Flux Limits from the IMB Proton Decay Detector*, *Physical Review* **D 49**, (1994) 2169.

[77] M.W. Ray et al. *Science: Vol. 348*, Issue 6234, pp. 544-547.

[78] B. Acharya et al., *Search for magnetic monopoles with the MoEDAL prototype trapping detector in 8 TeV proton-proton collisions at the LHC*, *JHEP* **08** (2016) 067.

[79] B. Acharya et al., *Search for magnetic monopoles with the MoEDAL forward trapping detector in 13 TeV proton-proton collisions at the LHC*, *Physical Review Letters* **118** (2017) 061801.

[80] Katz, U.F. et al., *High-Energy Neutrino Astrophysics*, *Progress in Particle and Nuclear Physics* **67** (2012) 651–704.

[81] S.P. Ahlen, *Monopole-track characteristics in plastic detectors*, *Physical Review* **D 14** (1976) 2935.

[82] E. Bauer, *The energy loss of free magnetic poles in passing through matter*, *Mathematical Proceedings of the Cambridge Philosophical Society* **47(04)** (1951) 777–789.

[83] H. J. D. Cole, *The theoretical behaviour of a magnetic monopole in a wilson cloud chamber*, *Mathematical Proceedings of the Cambridge Philosophical Society* **47(01)** (1951) 196–206.

[84] S.P. Ahlen, *Stopping-power formula for magnetic monopoles*, *Physical Review* **D 17**, 1 (1978) 229.

[85] Y. Kazama et al., *Scattering of a Dirac particle with charge Ze by a fixed magnetic monopole*, *Physical Review* **D 15** (1977) 2287.

[86] R.M. Sternheimer, R.F. Peierls, *Physical Review* **B3**, (1971) 3681.

[87] F. Bloch, *Annalen der Physik (Leipzig)* **16**, (1933) 285.

[88] J. Posselt, *Search for Relativistic Magnetic Monopoles with the IceCube 40-String Detector*, Ph.D. thesis, University of Wuppertal (2013).

[89] S.D. Wick et al., *Astroparticle Physics* **18**, (2003) 663.

[90] S.R. Kel'ner, *Soviet Journal of Nuclear Physics* **5**, (1967) 778.

[91] S.R. Kel'ner, Yu.D. Kotov, *Soviet Journal of Nuclear Physics* **7**, (1968) 237.

[92] S.I. Dutta, M.H. Reno, I. Sarcevic, D. Seckel, *Physical Review* **D63** (2001).

[93] J. Derkaoui et al., *Energy losses of magnetic monopoles and of dyons in the earth*, *Astroparticle Physics* **9** (1998) 173.

[94] V.A. Rubakov, *Superheavy Magnetic Monopoles and Decay of the Proton*, *JETP Letters* **33**, (1981) 644.

[95] V.A. Rubakov, *Adler-Bell-Jackiw Anomaly and Fermion-Number Breaking in the Presence of a Magnetic Monopole*, *Nuclear Physics* **B 203**, (1982) 311.

[96] C.G. Callan, *Disappearing Dyons*, *Physical Review* **D 25**, (1982) 2141.

[97] C.G. Callan, *Dyon-Fermion Dynamics*, *Physical Review* **D 26**, (1982) 2058.

[98] D.R. Tompkins, *Total energy loss and Cerenkov emission from monopoles*, *Physical Review* **138** (1965) 248.

[99] S.P. Ahlen, *Reviews of Modern Physics* **52**, (1980) 1.

[100] D.E. Groom, S.R. Klein, Particle Data Group, *Passage of Particles through Matter*, *European Physical Journal* **C 3**, (1998) 144.

[101] B. Rossi, *High-Energy Particles*, *Prentice-Hall, Inc.*, (1952).

[102] R.M. Sternheimer, *Density Effect for the Ionization Loss in Various Materials*, *Physical Review* **103**, (1956) 511.

[103] S.M. Seltzer and M.J. Berger, *Improved Procedure for Calculating the Collision Stopping Power of Elements and Compounds for Electrons and Positrons*, *International Journal of Applied Radiation and Isotopes* **35**, (1984) 665.

[104] G.R. Lynch and O.I. Dahl, *Approximations to Multiple Coulomb Scattering*, *Nuclear Instruments and Methods* **B 58**, (1991) 6.

[105] Particle Data Group, *Passage of Particles through Matter*, *European Physical Journal* **C 3**, (1998) 144.

[106] *Application Software Group, GEANT, CERN Program Library Long Writeup W5013* (1993), http://wwwasd.web.cern.ch/wwwasd/geant/.

[107] B. A. P. van Rens, *Detection of Magnetic Monopoles below the Cherenkov Limit*, Ph.D Thesis, NIKHEF, Amsterdam, The Netherlands.

[108] J. Brunner, *GEASIM*, March 2000.
http://antares.in2p3.fr/internal/software/geasim.html.

[109] G. Carminati et al., *Atmospheric MUons from PArametric formulas: a fast GEnerator for neutrino telescopes (MUPAGE)*, *Computer Physics Communications* **179(12)** (2008) 915.

[110] Y. Becherini et al., *A Parameterisation of single and multiple muons in the deep water or ice*, *Astroparticle Physics* **25** (2006) 1.

[111] J. Brunner, *ANTARES simulation tools, Proceedings of the VLVnT 2003, Amsterdam (http://www.vlvnt.nl/proceedings.pdf)*.

[112] A. Margiotta, *Common simulation tools for large volume neutrino detectors*, *NIM* **A725** (2013) 98.

[113] V. Agrawal et al., *Atmospheric neutrino flux above 1 GeV*, *Physical Review* **D 53** (1996) 1314.

[114] G.D. Barr et al., *Uncertainties in atmospheric neutrino fluxes*, *Physical Review* **D 74** (2006) 094009.

[115] G. Basttistoni et al. *Astroparticle Physics* **12** (2000) 315-333.

[116] M. Honda et al. *Physical Review* **D52** (1995) 4985-5005.

[117] C.G.S. Costa, *Astroparticle Physics* **16** (2001) 193-204.

[118] C. G. S. Costa, *The prompt lepton cookbook*, *Astroparticle Physics* **16**, (2001) 193, hep-ph/0010306.

[119] P. Antonioli et al., *A Three-dimensional Code for Muon Propagation through the Rock: MUSIC*, *Astroparticle Physics* **7**, (1997) 357.

[120] S. Navas and L. Thompson, *KM3 User Guide and Reference Manual*, (November 1999), *ANTARES internal note Soft/1999-011*.

[121] J.A. Aguilar et al., *A fast algorithm for muon track reconstruction and its application to the ANTARES neutrino telescope*, *Astroparticle Physics* **34** (2011) 652.

[122] C. Reed, *CalReal Update*, Antares collaboration Meeting, Paris, 17th June 2008.

[123] F. James and M. Roos, *Computer Physics Communications* **10** (1975) 343.

[124] M. Circella, *Nuclear Instruments and Methods* **A 602**, (2009) 1–6.

[125] H. van Haren et al., *Deep-Sea Research* **I 58**, (2011) 875–884.

[126] L. Fusco and A. Margiotta, *The Run-by-Run Monte Carlo simulation for the ANTARES experiment*, *EPJ Web of Conferences* **116** (2016) 02002.

[127] S. Adrian-Martinez et al., *Searches for Point-like and extended neutrino sources close to the Galactic Centre using the ANTARES neutrino Telescope*, *Astrophysical Journal Letters* **786:L5** (2014) arxiv:1402.6182.

[128] G.C. Hill and K. Rawlins, *Unbiased cut selection for optimal upper limits in neutrino detectors: the model rejection potential technique*, *Astroparticle Physics* **19** (2003) 393.

[129] G.J. Feldman and R.D. Cousins, *Unified approach to the classical statistical analysis of small signals*, *Physical Review* **D 57** (1998) 3873.

[130] S. Adrian-Martinez et al., *Measurement of the atmospheric ν_μ energy spectrum from 100 GeV to 200 TeV with the ANTARES telescope*, *European Physical Journal* **C 73** (2013) 2606.

[131] S. Adrian-Martinez et al., *First search for point sources of high-energy cosmic neutrinos with the ANTARES neutrino telescope*, *The Astrophysical Journal Letters* **743:L14** (2011) (6pp).

[132] P. Amram et al., *The ANTARES optical module*, *Nuclear Instruments and Methods* **A484** (2002) 369.

[133] J.A. Aguilar et al., *Transmission of light in deep sea water at the site of the ANTARES neutrino telescope*, *Astroparticle Physics* **23** (2005) 131.

[134] A. Albert et al., *Search for relativistic magnetic monopoles with five years of the ANTARES detector data*, *JHEP* **07** (2017) 054.

[135] V. Aynutdinov et al., *Search for relativistic magnetic monopoles with the Baikal neutrino telescope*, *Astroparticle Physics* **29** (2008) 366.

[136] E. Fermi, *Nuclear Physics*, University of Chicago Press (1950), ISBN 9780226243658.

[137] E. Rutherford, *The scattering of alpha and beta particles by matter and the structure of the atom*, *Philosophical Magazine* **21** (1911) 669–688.

[138] K. A. Olive et al. (Particle Data Group), *Chinese Physics* **C 38(9)** (2014) 090001.

[139] H. Bethe , *Annals of Physics* **5**, (1930) 325. H. Bethe, *Zeitschrift für Physik* **76**, (1932) 293.

[140] L. Landau, *Journal of Physics (USSR)* **8**, (1944) 201; in: L.D. Landau, Colleted Papers, ed. D. ter Haar (Pergamon, Press, Oxford, q965), p. 417.